

# On Stabilizing Aluminium Electrolysis Cells with Oscillating Currents

by

Ibrahim Mohammad

Submitted in Partial Fulfillment

of the

Requirements for the Degree

Doctor of Philosophy

Supervised by

Professor Douglas H. Kelley

Department of Mechanical Engineering  
Arts, Sciences and Engineering

Edmund A. Hajim School of Engineering and Applied Sciences

University of Rochester  
Rochester, New York

2023

I dedicate this document to God who has blessed me with the desire and opportunity to seek knowledge. May God accept this document from me as a source of knowledge for others to benefit from.

# Table of Contents

<b>Biographical Sketch</b>	<b>v</b>
<b>Acknowledgments</b>	<b>viii</b>
<b>Abstract</b>	<b>xiii</b>
<b>Contributors and Funding Sources</b>	<b>xv</b>
<b>List of Tables</b>	<b>xviii</b>
<b>List of Figures</b>	<b>xix</b>
<b>1 Introduction</b>	<b>1</b>
1.1 Aluminium Production . . . . .	1
1.2 Energy Consumption of Al Production . . . . .	3
1.3 Equations of Magnetohydrodynamics in Al Electrolysis Cells . . .	8
1.4 Metal Pad Instability . . . . .	13
1.5 Hypothesis and Thesis Overview . . . . .	18
<b>2 Stabilizing a Low-Dimensional Model of Magnetohydrodynamic Instabilities in Aluminium Electrolysis Cells</b>	<b>19</b>
2.1 Introduction . . . . .	19

2.2	Mechanical Model . . . . .	21
2.3	Deriving Equations of Motion . . . . .	24
2.4	Numerical Solution . . . . .	31
2.5	Summary and Future Work . . . . .	39
2.6	Acknowledgements . . . . .	40
<b>3</b>	<b>Stabilizing Aluminium Electrolysis Cells via Oscillating Currents in Simulation</b>	<b>42</b>
3.1	Introduction . . . . .	42
3.2	Characterizing Interface Oscillations . . . . .	46
3.3	Simulating MPI in a TRIMET 180 kA Al Electrolysis Cell . . . . .	50
3.4	Stabilization Using an Oscillating Current . . . . .	56
3.5	Summary and Future Work . . . . .	67
3.6	Acknowledgements . . . . .	69
<b>4</b>	<b>Stabilizing Electrolysis Cells with Oscillating Currents: Oscilla- tion Amplitude and Current Efficiency</b>	<b>71</b>
4.1	Introduction . . . . .	71
4.2	Oscillation Current Amplitude and Frequency . . . . .	74
4.3	On the Impact of Exciting Standing Waves on Current Efficiency	78
4.4	Cell Noise and Current Efficiency . . . . .	85
4.5	Summary and Future Work . . . . .	88
4.6	Acknowledgements . . . . .	90
<b>5</b>	<b>Conclusion</b>	<b>92</b>
	<b>Bibliography</b>	<b>95</b>

## Biographical Sketch

The author, Ibrahim Mohammad, was born as a Palestinian refugee in Beirut, Lebanon. He attended schools offered by the United Nations for refugees (UN-RWA schools) in Lebanon: Yaabad Elementary School, Ariha Middle School, and Galilee Secondary School. Early on, the author was motivated to learn so he can do well at school and make his parents proud. At 12 years old, he started working to help support his family financially, and experienced early on how hard it can be to earn a living. This made him realize that education is his way of doing better, and changed his motivation for learning from something external to something internal. Through the help of AMIDEAST Lebanon, EducationUSA, and The Hope Fund he was able to do the TOEFL and SAT exams, and apply to colleges and universities in the US.

In 2013, he received the Renaissance and Global Scholarship to attend the University of Rochester (UR), where he studied mechanical engineering and mathematics. While at UR the author benefited from an incredible education, exposure to people with diverse backgrounds and thoughts, an abundance of resources to grow and explore ideas, and meeting many kind people that supported him along the way. In 2014, he received the Xerox Engineering Research fellowship which allowed him to do research at Professor Douglas Kelley's lab in the Mechanical Engineering Department that summer. Research was different from classes, it taught him how to ask questions rather than to focus on finding answers, and was a great opportunity to learn. Also, Prof. Kelley was an incredible mentor that

helped the author develop critical thinking, grow his knowledge and skill set, and supported him inside and outside the lab.

The author kept working in Prof. Kelley’s lab, and in November 2016 he had the opportunity to present his research at the American Physical Society-Division of Fluid Dynamics (APS-DFD) conference where he realized that he wanted to continue his education so he can learn how to think. In 2017, he graduated from UR with a Bachelor of Science degree in Mechanical Engineering and a Bachelor of Arts degree in Mathematics, and pursued a Doctorate in Mechanical Engineering at UR right after. He joined Prof. Kelley’s lab, and in 2018 he received a Master of Science in Mechanical Engineering. As the author matured through the PhD journey, he felt both humbled and excited to learn more about nature and life, and realized that his motivation to keep learning is because it makes him a better person.

List of publications:

1. **I. Mohammad**, M. Dupuis, P.D. Funkenbusch, and D.H. Kelley, “Oscillating Currents Stabilize Aluminum Cells for Efficient, Low Carbon Production,” *JOM* **74**,1908-1915 (2022).
2. **I. Mohammad** and D.H. Kelley, “Stabilizing a Low-Dimensional Model of Magnetohydrodynamic Instabilities in Aluminum Electrolysis Cells,” *Light Metals 2022* edited by D. Eskin(Springer International Publishing, Cham, 2022), pp. 512–519.
3. **I. Mohammad**, M. Dupuis, P.D. Funkenbusch, and D.H. Kelley, “Stabilizing Electrolysis Cells with Oscillating Currents: Amplitude, Frequency, and Current Efficiency,” *Light Metals 2022* edited by D. Eskin(Springer International Publishing, Cham, 2022), pp. 551–559.
4. J.S. Cheng, **I. Mohammad**, B. Wang, D. Keogh, J. Forer, and D.H. Kelley, “Oscillations of the large-scale circulation in experimental liquid metal

- convection at aspect ratios 1.4–3,” *Journal of Fluid Mechanics* **949**, A42 (2022).
5. J.S. Cheng, **I. Mohammad**, B. Wang, J. Forer, and D.H. Kelley, “Laboratory model of electrovortex flow with thermal gradients for liquid metal batteries,” *Exp Fluids* **63**, 178 (2022).

## Acknowledgments

I have been blessed in knowing many good people who supported me at different points in my life. Without their help, I would not be in this position today. My attempt here falls short of actually describing their contribution.

To start, I would like to thank my father and mother for raising me when I was young, and doing their best for my siblings and I. My father sold juice on a cart on the street from 5 am till 8 pm everyday, well into his 70s, to provide for us. He could've easily given up and stopped working but he didn't so we could eat. Now that he passed away, may God have mercy on him. My mother dedicated her life to raising and taking care of us. She always pushed me to do well in school and fought for my education, and is the kindest person I know. I pray to God that she has good health and be happy for the rest of her life. I also want to thank my younger siblings, Youssef and Mariam, for taking care of my dad in his last years while I was here. Their sacrifice allowed me to continue pursuing my education. I also want to thank Grace, my wife and partner, for supporting me on this journey with her love, kindness, and patience.

Then, I would like to thank my PhD advisor Prof. Douglas Kelley, who had a tremendous positive impact on my life that is hard for me to sum up. I started working for Prof. Kelley as an undergraduate student summer of 2014, and I had such a positive experience there that I decided to pursue a PhD after. I wasn't the best student and always struggled with self-doubt, but Prof. Kelley gave me the opportunity to pursue a PhD in his lab and supported me at every step of

the way till now, allowing me to grow and mature as a person and scientist. He helped me develop my critical thinking, grow my knowledge and skill set, and supported me inside and outside the lab. His door was always open since 2014 for questions about research and advice about life. Other than being a great scientist and mentor, Prof. Kelley is a great human being. He is humble, generous, patient, and kind. He is the person I learned from the most, and one that I look up to in many aspects of my life. I will be always grateful to him.

In addition, I would like to thank my PhD defense committee members, Prof. Riccardo Betti for meeting with me on multiple occasions to help me understand the problem I was working on and explaining magnetohydrodynamic equations, for an excellent class on hydrodynamic instabilities that gave me most of the insight I have on instabilities such as "instabilities are pretty sneaky phenomena, they try to minimize the energy they need to develop", and for teaching me linear stability analysis; Prof. David Foster for his support with Ansys simulations when I was trying to use it initially before we switched simulation packages, and for giving me valuable career advice on multiple occasions; Dr. Marc Dupuis for valuable lessons on aluminium electrolysis, the aluminium industry, sharing with me many references and resources to learn from, and his generosity when it came to sharing his knowledge and his time; Prof. Earl Conee for serving as my defense committee chair, and for teaching me two great classes on ethics as an undergraduate that I really enjoyed and deepened my interest in the topic.

I would like to acknowledge and thank my lab mates (and friends), Dr. Bitong Wang who inspired me with his strong work ethic and always motivated me; Dr. Jonathan Cheng for being a great leader, sharing knowledge and know-how, and offering helpful insights; Dr. Thomas Nevins who helped me on many occasions as an undergraduate researcher, for sharing knowledge and ideas, and for great conversations I learned a lot from; Dr. Rakan Ashour for teaching me about batteries and thinking about the big picture; Dr. Jeff Tithof for always offering to

help, and for sharing knowledge and know-how; Dr. Adi Raghunadnan and Dr. Kimberly Boster for helpful insights during group meetings, and offering good advice; Jinge and Yiming, for great conversations and being good friends.

The mechanical engineering department feels like home to me, and I owe the professors and staff there a great deal for teaching me, supporting me, and for their kindness towards me. I would like to thank Prof. Muir who taught me many classes that helped me gain most of the insight I have for engineering design and material failure, for being an excellent teacher, and for teaching me MATLAB; Prof. Nam, who always inspired me with the passion he has for his research, for being an excellent teacher that pushed me during classes, for teaching me about vibrations and numerical methods, and giving me an example in fairness as a teacher; Prof. Lambropoulos for being an excellent teacher, teaching me thermodynamics, and offering me important pieces of advice that shaped my PhD experience; Prof. Funkenbusch for being an excellent teacher, teaching me fluids lab and experimental design, and being a great collaborator to work with; Prof. Gracewski for being an excellent teacher and for a great class on boundary value problems; Prof. Askari for teaching me heat and mass transfer and finite element method; Prof. Aluie for teaching me about fluid dynamics and for helpful advice; Prof. Goncharov for teaching me about solving partial differential equations; Prof. Perucchio for teaching an excellent class on the engineering of bridges that was the first mechanical engineering class I took; Prof. Ren for teaching me heat and power, for explaining some magnetohydrodynamics, and for letting me sit on a couple of lectures in his plasma physics class; Prof. Jessica Shang for teaching me about continuum mechanics; Prof. John Thomas for helping me understand some magnetohydrodynamics; Prof. Adam Sefkow for being a great teacher, for letting me sit in on his numerical methods class, and for his inspiring talks; Prof. Ranga Dias for inspiring me with his hard work and view of the big picture; Sarah Ansini for critical support to stay on track with the PhD degree, sending registration

reminders, helping schedule preliminary and qualifier exams, and administrative support in the final thesis submission; Jill Morris for her support and kindness; Chris Prat, Mike Pomerantz, and Scott Russell for teaching me all the labs I took, for support, and offering important advice when it came to building experiments; Jim Alkins and John Miller for teaching me mechanical fabrication, and offering design advice.

I would also like to thank the professors who taught me from the mathematics department, Prof. Geba for being an excellent teacher, for teaching me about math competitions and how to solve problems, and for an incredible class on partial differential equations; Prof. Herman for being an excellent teacher, for his kindness, and teaching me multivariable calculus and the history of math; Prof. Greenleaf for teaching me proof based calculus and for excellent class notes; Prof. Dummit for an excellent class on number theory and cryptography; Prof. Mkrtchyan for teaching me probability; Prof. Thakur for teaching me linear algebra; Prof. Tucker for teaching me group theory; Prof. Madhu for being a great teacher; Prof. Neuman for teaching me about ordinary differential equations theory. I would like to also thank from the data science department Prof. Mort from the for teaching me introductory data science, and Dr. Harry Stern for his support in installing Ansys on the BlueHive Cluster; the University of Rochester Linux cluster containing 480 nodes, 14392 CPU cores, and 72 TB RAM.

From when I was a student in Lebanon I would like to thank and acknowledge Samira Mansour for being a great elementary school principal and making us feel like normal students rather than refugees; Itidal for her support; Hiba Mohammad for giving me advanced math books to learn from; Jihad Idriss and Khaled Kassim for motivating me in middle school; Hanan Al-Shourafa and Ahmad Il-Saeed for being excellent teachers in high school. Also, I would like to thank AMIDEAST Lebanon office for helping me apply to US universities and making it possible, in particular I would like to recognize Sarah El-Dallal whose help was instrumental

for me. I would like to thank the Hope Fund for supporting my university applications, to Deyaa for introducing me to the US culture and helping me settle in, and to Ginny Lapham for hosting me when I first came to the US. Also, I would like to thank Jonathan Burdick for his continuous support throughout my time as an undergraduate student, and Ann Robinson from the office of undergraduate research for her support and kindness.

Finally, I would like to thank my aunts and uncles for supporting my family, in particular uncle Mostapha, aunt Hedia, and aunt Aisha. Also, I want to thank my best friend Omar Soufan, and my closest friends Edgar Alaniz, Tarif Homsy, Ibrahim Sonji, Hamza Al-Murdaa, Ossama, and Yuki for their help and support.

# Abstract

Humankind produced 67.1 million metric tons of primary aluminium (Al) metal [1] in 2021, nearly all via the Hall-Héroult electrolytic process in which electrical current liberates molten Al from alumina dissolved in an electrolyte inside an electrolysis cell [2]. That year, Al production required 843 TWh of electrical energy [3], 3.4% of the world total [4]. About 50% of the electrical energy does not produce any aluminium [5], and is instead lost in the form of heat in the poor electrically conducting electrolyte where the alumina is dissolved. Thinning the electrolyte layer could decrease loss [5] but has been limited by the Metal Pad Instability (MPI) [6], which causes Al cells to slosh out of control if the electrolyte is not sufficiently thick. The MPI is a magnetohydrodynamic process that depends on a coupled resonance between hydrodynamic gravity wave modes, driven by the cell's electrolytic current, and appears as a circulating traveling wave on the Al-electrolyte interface that grows exponentially [7].

Parametric instabilities can often be decoupled by introducing a new frequency that frustrates the resonance, so we hypothesized that adding an oscillation to the current would prevent the MPI. To start, I extend a mechanical analogue of the MPI [8] to include an oscillating current component, and show that the extended model is stabilized by the oscillating current. I also explore the stability of the extended mechanical model at different oscillation amplitudes and frequencies. Then, I show in high fidelity numerical simulations of a TRIMET 180 kA electrolysis cell that adding an oscillating current component prevented the MPI, and

allowed for stable operation at 11.6% lower electrolyte thickness than with steady current only. I analyze the Al-electrolyte interface evolution, through the fast Fourier transform and projecting the interface displacement onto the hydrodynamic gravity wave modes, to show that the oscillating current excites standing gravity wave modes that frustrate the MPI. Finally, I examine the impact of the oscillation current amplitude and frequency on stability, and investigate the potential effects exciting the standing waves might have on the Al cell's current efficiency. This novel method of stabilizing Al electrolysis cells could allow Al production at lower cost, with less energy, and a smaller carbon footprint [9].

## Contributors and Funding Sources

This work was supervised by a dissertation committee consisting of Professor Douglas H. Kelley (advisor) of the Department of Mechanical Engineering, Professor Riccardo Betti of the Department of Mechanical Engineering, Professor David G. Foster of the Department of Chemical Engineering, Dr. Marc Dupuis an expert on dynamical modelling of aluminium electrolysis cells from outside the University of Rochester, and Professor Earl Conee (chair) from the Department of Philosophy.

Financial support for this thesis was received from the National Science Foundation (NSF) through grant CBET-1552182, and from a University of Rochester, URVentures TAG award.

Chapter 2 is based on “Stabilizing a Low-Dimensional Model of Magnetohydrodynamic Instabilities in Aluminum Electrolysis Cells” which was printed in the book *Light Metals 2022* [10], and has been modified to fit in this thesis. The thesis author is the primary author and was responsible for deriving the model’s equations of motion, writing the MATLAB code to numerically solve the equations of motion, and writing the paper. The thesis author prepared all the figures, except Fig. 2.2 and Fig. 2.3 which were prepared by co-author Prof. Douglas Kelley. Co-author Prof. Douglas Kelley came up with the idea of extending the mechanical model of the MPI to test the stabilizing effect of adding an oscillating current, provided guidance on deriving the equations of motion, on developing the numerical solution algorithm, on figure formation, and edited the paper. Conversations with Prof. Riccardo Betti and Dr. Marc Dupuis offered valuable insights.

Chapter 3 is based on material primarily from “Oscillating Currents Stabilize Aluminum Cells for Efficient, Low Carbon Production” which was printed in the journal *JOM* [9], and some material “Stabilizing Electrolysis Cells with Oscillating Currents: Amplitude, Frequency, and Current Efficiency” which was printed in the book *Light Metals 2022* [7]. Both have been modified to fit in this thesis. The thesis author and co-author Douglas Kelley wrote the original paper [9], and the thesis author wrote [7]. The thesis author was the primary author and was responsible for performing the data analysis, including creating videos of the interface height and displacement, plotting the root-mean-square interface displacement with exponential fits, calculating the oscillation power spectra, and projecting the interface displacement onto the set of basis wave modes. The thesis author wrote all the custom MATLAB code to perform the analysis with the help and guidance from co-author Prof. Douglas Kelley, who also wrote the first version of the mode projection code. The thesis author produced all figures in this chapter, except Fig. 3.1 which was courtesy of co-author Dr. Marc Dupuis and Fig. 3.2 which was made by co-author Prof. Douglas Kelley. Co-author Marc Dupuis was responsible for running the TRIMET 180 kA Al cell simulations on MHD-Valdis software [11]. Co-author Prof. Paul Funkenbusch and the thesis author guided oscillation current’s amplitude and frequency choices for the simulation campaign. The thesis author explained how the different mode pairs couple through the different components of the vertical magnetic field, and how the three mode coupling happens in the MPI. The thesis author found that the oscillating current is exciting standing waves and co-author Prof. Douglas Kelley came up with the hypothesis on the stabilization mechanism. Co-author Prof. Douglas Kelley came up with the idea of stabilization Al cell with oscillating currents and conceived this study. The thesis author is grateful for support from, and conversations with, Prof. Riccardo Betti that offered valuable insights at various points in this study. The thesis author is also grateful to Prof. David Foster, Dr. Gerrit

M. Horstmann, and Dr. Jonathan S. Cheng for fruitful discussions, and to Dr. Curtis Broadbent for leading the commercialization efforts of this work [12].

Chapter 4 is based on material primarily from “Stabilizing Electrolysis Cells with Oscillating Currents: Amplitude, Frequency, and Current Efficiency” which was printed in the book *Light Metals 2022* [7], and some unpublished work aimed at expanding the discussion of the impact of using oscillating currents on current efficiency. The material from the paper [7] has been modified to fit in this thesis. The thesis author was the primary author and was responsible for writing the paper, performing all the data analysis, writing the custom MATLAB code to perform the analysis, and producing all the figures except where it was noted in the caption. Working out the impact of using the oscillating current on cell noise was done through a correspondence between the thesis author and co-author Marc Dupuis. Co-author Dr. Marc Dupuis was responsible for running the TRIMET 180 kA Al cell simulations on MHD-Valdis software, and provided guidance on the topic of Al electrolysis cell current efficiency. Co-author Prof. Paul Funkenbusch and the thesis author guided oscillation current’s amplitude and frequency choices for the simulation campaign. Co-author Prof. Douglas Kelley came up with the idea of stabilization Al cell with oscillating currents, and provided guidance and support throughout this work. The thesis author is grateful to Prof. Riccardo Betti, Prof. David Foster, Dr. Gerrit M. Horstmann, and Dr. Jonathan S. Cheng for fruitful discussions, and to Dr. Curtis Broadbent for leading the commercialization efforts of this work [12].

# List of Tables

1.1	Voltage sources in (V) for an Al electrolysis cell that operates at 93% $CE$ and has 4.373 V cell voltage. Data is from Reference [13]. The specific energy consumption of this cell is 14 kWh/(kg Al). . . . .	8
3.1	Electrical conductivities, $\sigma$ , of the fluid layers and carbon anodes used in the simulation in S/m. . . . .	45
3.2	Density of the molten Al and electrolyte layers used in the simulations.	45

# List of Figures

1.1	Metals produced/mined by humankind in 2021. Aluminium is the the most produced non-ferrous metal at 68 million metric tonnes. Figure is from Visual Capitalist Reference [14] . . . . .	2
1.2	Primary Aluminium metal production from 2011 to 2021. Data is from International Aluminium [1] . . . . .	3
1.3	Schematic of a cross-section of an Aluminium electrolysis cell. These electrolysis cells rely on the Hall-Héroult process to produce aluminium metal. Reprinted by permission from Springer Nature Customer Service Centre GmbH: Springer Nature, <i>SN Applied Sciences</i> , “A review of primary aluminium tapping models”, Kitungwa Kabezya et al (2019) [15] . . . . .	4
1.4	Picture of a potline of Al electrolysis cells. Reprinted by permission from Wolters Kluwer Health, Inc: from Halvor Kvande and Per Drabløs, “The Aluminum Smelting Process and Innovative Alternative Technologies”, <i>Journal of Occupational and Environmental Medicine</i> (2014) [16] . . . . .	5

1.5	A representation of the Sele mechanism. The Al-electrolyte interface is plotted when the interface is tilted, red means above flat surface and blue means below. Due to the low conductivity of the electrolyte, a vertical perturbation current (yellow) is created near the wave crest. Due to the high conductivity of the Aluminium, the perturbation current is horizontal there and interacts with the vertical magnetic field to produce a horizontal Lorentz force (green). The Lorentz force pushes the Al moving the wave crest along the side walls of the cell counter clockwise. . . . .	15
2.1	Schematic diagram of the compound pendulum model. The pendulum can swing about both the $x$ and $y$ axes, with the $x$ -axis as shown and the $y$ -axis pointing into the page. . . . .	24
2.2	Pendulum model at initial unperturbed state, and under small rotation about $x$ -axis . . . . .	25
2.3	Only the electromagnetic and gravitational forces have a net non-zero torque with respect to the pivot. . . . .	29
2.4	Numerical solutions for the decoupled case $a = 0$ . <b>a</b> , $\gamma_x$ oscillates in time at a single frequency. <b>b</b> , $\gamma_y$ oscillates in time at a single frequency that is lower than that of $\gamma_x$ . <b>c</b> The power spectrum of both $\gamma_x$ and $\gamma_y$ shows that each oscillates exactly at its pure angular gravitational frequency. . . . .	33

- 2.5 Numerical solutions at  $a$  slightly above and below  $a_{\text{crit}}$ . **a**,  $a = 1.100205$ , the Al plate is stable with  $\gamma_x$  oscillating in time and beating phenomenon is present. The regions appearing solid blue indicate oscillations too fast to be individually visible. **b**, an enlargement of the same data as (a) plotted for only 50 s. The oscillations inside the amplitude envelope can now be seen. **c**,  $\gamma_y$  is also stable, behaving the same as  $\gamma_x$ . **d**,  $a = 1.100207$ , the Al plate is unstable with the amplitude of  $\gamma_x$  increasing exponentially in time. The regions appearing solid blue indicate oscillations too fast to be individually visible. **e**, an enlargement of the same data as (d) plotted for only 50 s. **f**,  $\gamma_y$  is also unstable, behaving the same as  $\gamma_x$ . 36
- 2.6 Numerical solutions at  $a = 1.100207$  with an oscillating current of  $\beta = 0.1$  and  $\omega_b = 0.94$  rd/s. **a**,  $\gamma_x$  oscillating in time stably. The regions appearing solid blue indicate oscillations too fast to be individually visible. **b**, an enlargement of the same data as (a) plotted for only 100 s. The oscillations inside the amplitude envelope can now be seen. **c**, The power spectrum of  $\gamma_x$  shows two frequencies, one near the oscillating frequency. . . . . 37
- 2.7  $(\beta, \omega_b)$  phase space for  $a = 1.100207$ . The motion is stable for many pairs of the oscillating current's angular frequency and normalized amplitude. The stable pairs cluster at two distinct regions. . . . . 38
- 2.8  $(\beta, \omega_b)$  phase space for  $a = 1.133213$ . The motion remains stable for only a few pairs of the oscillating current's angular frequency and normalized amplitude. . . . . 38

3.1	Snapshot of the TRIMET 180 kA potline model from MHD-Valdis software showing busbar layout. Color represents the current, $I$ , in each conductor in Ampere (A). Figure is courtesy of Dr. Marc Dupuis. . . . .	44
3.2	Characteristics of Al electrolysis cells. <b>a</b> , Electrical current flows downward from anodes to cathode, through electrolyte and Al layers. <b>b</b> , The vertical component of the ambient magnetic field, at the Al-electrolyte interface, from our simulations, seen from above. The field varies spatially and is caused primarily by currents in the adjacent cells and nearby busbars. <b>c</b> , The Al-electrolyte interface bulges because of electromagnetic forces due to the magnetic field and the current. . . . .	50
3.3	Root-mean-square displacement of the Al-electrolyte interface at 4.3 cm ACD. An exponential fit is shown in blue for $t > 100$ s. The RMS displacement decays very slowly in time. . . . .	50
3.4	Current, voltage, and total power for the TRIMET Al cell at 4.3 cm ACD with steady current. <b>a</b> , Current supplied is constant at 180 kA. <b>b</b> , Cell voltage exhibits a low-frequency oscillation from the waves on the Al-electrolyte interface. The average voltage is 4.467 V. <b>c</b> , Total cell power. Average total power is 804.8 kW. . . . .	51
3.5	Current, voltage, and total power for the TRIMET Al cell at 4 cm ACD with steady current. <b>a</b> , Current supplied is constant at 180 kA. <b>b</b> , Cell voltage exhibits a low-frequency oscillation from the waves on the Al-electrolyte interface. The average voltage is 4.34 V, and the sudden voltage drop at the end is due to the short circuit happening when the Al layer touched the anode. <b>c</b> , Total cell power. The sudden drop in power at the end is due to the short circuit. The average total power is 781.6 kW. . . . .	52

- 3.6 The metal pad instability (MPI) in a simulated Al electrolysis cell. **a**, Displacement of the Al-electrolyte interface grows exponentially, as shown by the fitted curve. **b**, The spectral power of the displacement of one point on the interface is dominated by a narrow frequency band, close to the frequency of interface wave modes  $G_{2,0}$ ,  $G_{0,1}$ , and  $G_{1,1}$ , expected in the MPI. . . . . 52
- 3.7 Example of estimating the interface displacement through projecting onto the modes  $G_{m,n}$ . **a**, Al-electrolyte interface displacement at  $t = 125$  s. **b**, Estimate of the interface displacement at  $t = 125$  s through performing a linear least-square projection onto the interface modes  $G_{m,n}$ . The estimated interface displacement looks visually the same as the actual interface displacement. **c**, The % error of the interface displacement estimate relative to the actual interface displacement. The error is very low and  $< 4\%$  at all times. 54
- 3.8 The modes of the MPI in a simulated Al electrolysis cell. **a**,  $G_{2,0}$ ,  $G_{0,1}$ , and  $G_{1,1}$  have greater root-mean-square amplitude than any other modes. **b**,  $G_{2,0}$ ,  $G_{0,1}$ , and  $G_{1,1}$  oscillate with a common frequency and grow over time.  $G_{0,2}$  oscillates with the same frequency but does not grow in time. **c**,  $G_{2,0}$  and  $G_{0,1}$  are separated in phase by  $\sim 90^\circ$ , characteristic of a traveling wave as in the MPI. . . . . 54
- 3.9 Coupling of different mode pairs through the magnetic field components. **a-d** Coupling between  $G_{0,1}$  and  $G_{2,0}$  interface modes through the x-gradient component  $B_{xz}$  of the vertical magnetic field  $B_z$ . The modes are viewed from above, with the horizontal displacement current density  $j$  and resulting electromagnetic forces  $f$  sketched. **e-h** Coupling between  $G_{2,0}$  and  $G_{1,1}$  interface modes through the constant component  $B_{0z}$  of  $B_z$ . **i-l** Coupling between  $G_{0,1}$  and  $G_{1,1}$  interface modes through the y-gradient component  $B_{zy}$  of  $B_z$ . . . . . 55

- 3.10 Mode coupling creating the MPI. **a-d**, Interface displacements at four times spanning one MPI cycle (red dots in Fig. 3.8c) show a circulating traveling wave. **e-h**, Modal decomposition of the interface displacements at the same times as in (a-d). Two dominant modes are present at each time, and an interplay among  $G_{2,0}$ ,  $G_{0,1}$ , and  $G_{1,1}$  is evident in creating the MPI. **i-l**, Reconstruction of the interface displacements at the same times as in (a-d) using only the two most dominant modes present in each of (e-h), viewed from above.  $G_{0,1}$  and  $-G_{1,1}$  are present in (i) and excite  $G_{2,0}$  and  $G_{1,1}$  through the different components of  $B_z$  based on Fig. 3.9.  $G_{2,0}$  and  $G_{1,1}$  consequently excite  $-G_{0,1}$  and  $G_{1,1}$  and so on. . . . . 57
- 3.11 Current, voltage, and total power for the TRIMET Al cell at 4 cm ACD with an oscillating current of half-amplitude 19.8 kA and frequency 0.045 Hz **a**, Current supplied has an oscillating triangular component with an average of 180 kA. **b**, Cell voltage exhibits a low-frequency oscillation at the current driving frequency. The average voltage is 4.36 V. **c**, Total cell power. Average total power is 787.1 kW. . . . . 58
- 3.12 Characteristics of the interface displacement oscillations with an oscillating current of frequency 0.045 Hz and half-amplitude 19.8 kA. **a**, RMS interface displacement. The Al-electrolyte interface oscillates stably, not growing or decaying in time. **b**, The spectral power of the displacement of one point on the interface is dominated by one frequency band close to the expected in the MPI frequency, and another close to the drive frequency. . . . . 59

- 3.13 Oscillating current excites standing waves. **a**, The Al-electrolyte interface displacement at  $t = 125$  s. **b**, Reconstruction of the interface displacement through performing a projection onto the interface modes at  $t = 125$  s. The estimated interface displacement looks visually the same as the actual interface displacement. **c**, The % error of the interface displacement estimate relative to the actual interface displacement. The error is very low and  $\leq 3\%$  at all times. **d**,  $G_{2,0}$ ,  $G_{0,1}$ ,  $G_{1,1}$ ,  $G_{0,2}$ , and  $G_{4,0}$  have greater root-mean-square amplitude than any other modes. **e-f**, Their amplitudes  $\alpha_{m,n}$  oscillate, and  $G_{0,2}$  and  $G_{4,0}$  are almost aligned in phase, characteristic of a standing wave. . . . . 60
- 3.14 Standing waves frustrate the MPI. **a-d**, Interface displacements at four times spanning one drive cycle show a standing wave. **e-h**, Interface displacements at the same times as in (a-d), estimated using only  $G_{0,2}$  and  $G_{4,0}$  and viewed from above. The resulting electromagnetic forces  $\mathbf{f}$  (sketched) often favour clockwise circulation, opposing and frustrating the MPI. . . . . 60

- 3.15 An oscillating current component prevents the MPI at 3.8 cm ACD.  
**a**, The Al-electrolyte interface oscillates stably. **b**, The spectral power of the displacement of one point on the interface is dominated by one frequency band close to the expected in the MPI frequency, and another close to the drive frequency. **c**,  $G_{2,0}$ ,  $G_{0,1}$ ,  $G_{1,1}$ ,  $G_{0,2}$ , and  $G_{4,0}$  have greater root-mean-square amplitude than any other modes. **d-e**, Their amplitudes  $\alpha_{m,n}$  oscillate, and  $G_{0,2}$  and  $G_{4,0}$  are almost aligned in phase, characteristic of a standing wave. **f-i**, Interface displacements at four times spanning one drive cycle (red dots in (e)) show a standing wave. **j-m**, Interface displacements at the same times as in (f-i), estimated using only  $G_{0,2}$  and  $G_{4,0}$  and viewed from above. . . . . 62
- 3.16 Current, cell voltage, and power for the TRIMET Al cell at 3.8 cm ACD with an oscillating current of half-amplitude 19.8 kA and frequency 0.045 Hz **a**, Current supplied has an oscillating triangular component with an average of 180 kA. **b**, Cell voltage exhibits a low-frequency oscillation at the current driving frequency. The average voltage is 4.28 V. **c**, Cell total power. Average power is 773.4 kW. . . . . 63

- 3.17 An oscillating current component with frequency 0.069 Hz prevents the MPI. **a**, The Al-electrolyte interface oscillates stably. **b**, The spectral power of the displacement of one point on the interface is dominated by one frequency band close to the expected in the MPI frequency, and another close to the drive frequency. **c**,  $G_{2,0}$ ,  $G_{0,1}$ ,  $G_{1,1}$ ,  $G_{0,2}$ , and  $G_{6,0}$  have greater root-mean-square amplitude than any other modes. **d-e**, Their amplitudes  $\alpha_{m,n}$  oscillate, and  $G_{0,2}$  and  $G_{6,0}$  are almost aligned in phase, characteristic of a standing wave. **f-i**, Interface displacements at four times spanning one drive cycle (red dots in (e)) show a standing wave. **j-m**, Interface displacements at the same times as in (f-i), estimated using only  $G_{0,2}$  and  $G_{6,0}$  and viewed from above. . . . . 65
- 3.18 An oscillating current component halts the MPI in progress. **a**, The applied current was steady for the first 100 s, before an oscillatory current with half-amplitude 19.8 kA and frequency 0.045 Hz was added. **b**, Interface displacement grew when the current was steady but stopped growing soon after we added current oscillation, indicating stability. **c-f**, Interface displacements, when current was steady, at four times spanning one MPI cycle. A circulating travelling wave is present. **g-j**, Interface displacements, after we added the oscillating current, at four times spanning one drive cycle. A standing wave is present. . . . . 66

- 3.19 Wave modes when a non-initial current oscillation is applied. **a**, The spectral power of the displacement of one point on the interface shows many frequencies present, the dominant ones at the MPI frequency and current oscillation frequency. **b**, The estimated interface displacement using the wave mode projection had an error  $\leq 3\%$  at all times. **c**, RMS mode amplitude.  $G_{2,0}$ ,  $G_{0,1}$ , and  $G_{1,1}$  are strongest, followed by  $G_{0,2}$  and  $G_{4,0}$  **g-j**, Amplitudes of the  $G_{2,0}$ ,  $G_{0,1}$ , and  $G_{0,2}$  wave modes in time. . . . . 67
- 4.1 MPI present at 4 cm ACD, with an oscillating current of frequency 0.045 Hz and half-amplitude 2.9 kA. **a**, Root-mean-square displacement of the Al-electrolyte interface is growing exponentially in time. An exponential fit is shown in blue for  $t > 100$  s. **b**, The spectral power of the displacement of one point on the interface is dominated by a narrow frequency band, close to the frequency of interface wave modes  $G_{2,0}$ ,  $G_{0,1}$ , and  $G_{1,1}$ , expected in the MPI. . . . . 74

- 4.2 Modes at 4 cm ACD, with an oscillating current of frequency 0.045 Hz and half-amplitude 2.9 kA. **a**, Al-electrolyte interface displacement at  $t = 125$  s. **b**, Estimate of the interface displacement at  $t = 125$  s through performing a linear least-square projection onto the interface modes  $G_{m,n}$ . The estimated interface displacement looks visually the same as the actual interface displacement. **c**, The % error of the interface displacement estimate relative to the actual interface displacement. The error is very low and  $< 2.5\%$  at all times. **d**,  $G_{2,0}$ ,  $G_{0,1}$ , and  $G_{1,1}$  have greater root-mean-square amplitude than any other modes. **e**,  $G_{2,0}$ ,  $G_{0,1}$ , and  $G_{1,1}$  oscillate with a common frequency and grow over time.  $G_{0,2}$  oscillates with the same frequency but does not grow in time. **f**,  $G_{2,0}$  and  $G_{0,1}$  are separated in phase by  $\sim 90^\circ$ , characteristic of a traveling wave as in the MPI. . . . . 76
- 4.3 Al-electrolyte interface behaviour at 3.7 cm ACD, with an oscillating current of frequency 0.045 Hz and half-amplitude 36 kA. **a**, Al-electrolyte interface RMS displacement is very high, causing a short circuit. **b**, Power spectrum of interface displacement at a point shows a small peak near the oscillating current frequency **c**, The Al-electrolyte interface at  $t = 83.25$  s, right before the electrolysis cell shorted. A wave is present whose crest is high enough to touch the anode and cause a short-circuit. **d**, The % error of projecting the interface displacement onto the wave modes is  $< 3\%$  for the duration of the simulation. **e**,  $G_{0,2}$  mode is strongest. . . . . 77

- 4.4 Al-electrolyte interface behaviour at 4 cm ACD, with an oscillating current of frequency 0.5 Hz and half-amplitude 19.8 kA. **a**, The Al-electrolyte interface grows exponentially, and the MPI is present. **b**, The spectral power of the displacement of one point on the interface is dominated by one frequency band close to the expected MPI frequency. The driving frequency of 0.5 Hz is absent. . . . . 78
- 4.5 Interface area in stable, unstable, and stabilized electrolysis cells **a**, Al-electrolyte interface surface area as a function of time for a stable Al cell operating with a steady 180 kA current at 4.3 cm ACD. The surface area oscillates in time and decreases very slowly. **b**, Interface surface area for a cell operating with a 180 kA steady current at 4 cm ACD. The surface area is growing in time, which is consistent with the cell being unstable and the MPI present. **c**, Interface surface area for a cell operating at 4 cm ACD, but with the steady 180 kA current supplemented with an oscillating current of half-amplitude 19.8 kA and of frequency 0.045 Hz. The surface area oscillates in time and does not grow, consistent with the cell being stable. The interface surface area is larger than that of panel **a** due to the excited standing waves by the oscillating current. . . 79
- 4.6 Illustration of back reaction region with decreasing ACD. **a**, Distribution of interface height of the Al-electrolyte interface is in blue, and of the CO<sub>2</sub> gas bubbles forming on the anode is in pink. **b**, When the ACD is reduced and an overlap between the Al metal and CO<sub>2</sub> bubbles distribution occurs, the back reaction takes place reducing CE. Reprinted by permission from Springer Nature Customer Service Centre GmbH: Springer Nature, *Light Metals 2014*, “Current Efficiency in Aluminium Reduction Cells: Theories, Models, Concepts, and Speculations”, Asbjørn Solheim (2014) [17] . . 82

- 4.7 Distribution of Al-electrolyte interface height in stable, unstable, and stabilized electrolysis cells. **a**, Al-electrolyte interface height distribution for a stable Al cell operating with a steady 180 kA current at 4.3 cm ACD. **b**, Interface height distribution for a cell operating with a 180 kA steady current at 4 cm ACD. The cell is unstable with the MPI present and shorted. **c**, Interface height distribution for a cell operating at 4 cm ACD, but with the steady 180 kA current supplemented with an oscillating current of half-amplitude 19.8 kA and of frequency 0.045 Hz. . . . . 82
- 4.8 Distribution of Al-electrolyte interface height for a cell operating with steady current at 4.3 cm ACD, and cell operating at 4 cm ACD, but with the steady 180 kA current supplemented with an oscillating current of half-amplitude 19.8 kA and of frequency 0.045 Hz. 83
- 4.9 Distribution of maximum Al-electrolyte interface height at every instant in time for a cell operating the steady 180 kA current supplemented with an oscillating current of half-amplitude 19.8 kA and of frequency 0.045 Hz at 4 cm ACD, and another operating with the same current at 3.8 cm ACD. . . . . 84
- 4.10 Cell noise for TRIMET 180 kA Al electrolysis cells operating at different currents and ACD. **a**, Cell operating with steady current of 180 kA at 4.3 cm. **b** Unstable cell operating with steady current of 180 kA at 4 cm. **c** Cell operating at 4 cm ACD and with the steady current supplemented by an oscillating current of half-amplitude 19.8 kA and of frequency 0.045 Hz. **d** Cell operating at 3.8 cm ACD and with the steady current supplemented by an oscillating current of half-amplitude 19.8 kA and of frequency 0.045 Hz. . . . 87

# 1 Introduction

## 1.1 Aluminium Production

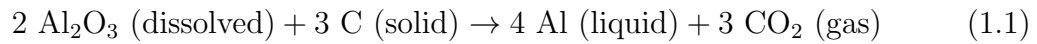
Aluminium (Al) is a very important industrial metal and the most widely used non-ferrous metal in the world [18], (see Fig. 1.1). In 2021, humankind produced 67.1 million metric tons of primary aluminium [1], about 187 times the mass of the Empire State building in New York City, and our demand for it has increased steadily over the past decade as shown in Fig. 1.2. Luckily, Al is the most abundant metal in the Earth's crust [18] though not in its pure elemental state, but as an oxide or silicate [2, 18]. The most important Al ore is bauxite [19], which contains 40 – 60% alumina ( $\text{Al}_2\text{O}_3$ ) by mass [2]. Early on, producing Al from ore was very expensive, making Al more expensive than gold, until 1886 when Charles Hall and Paul Héroult, simultaneously and independently, devised a process to electrolytically produce Al: decomposing alumina, dissolved in a cryolite ( $\text{Na}_3\text{AlF}_6$ ) electrolyte, via an electric current to liberate molten Al [2, 18]. For the Hall-Héroult process to be economically viable, high purity alumina must be produced efficiently, and this is done by using the Bayer process to refine alumina from bauxite [2, 18, 19] .

Nowadays, all large scale Al production is done through the Hall-Héroult pro-



**Figure 1.1:** Metals produced/mined by humankind in 2021. Aluminium is the the most produced non-ferrous metal at 68 million metric tonnes. Figure is from Visual Capitalist Reference [14]

cess in Al electrolysis cells [2]. A cell is made from a steel shell lined with refractory material [20], and canonically consists of two broad ( $\sim 8 \times 3.6$  m, or larger) and shallow fluid layers ( $\sim 5 - 20$  cm): molten Al beneath a floating layer of molten electrolyte, with both layers situated in between two carbon electrodes [9, 20] (see Fig. 1.3). Electrolysis cells operate at high temperatures, between  $935 - 960$  °C [21, 22], to keep the fluid layers molten. Several prebaked carbon anodes are dipped in the electrolyte, and raw alumina is fed to the electrolyte through a point feeder, where it dissolves [2]. A large, steady current ( $\sim 200 - 500$  kA [23]) is driven downward from the carbon anodes through the electrolyte to the cathode beneath the Al layer (Fig. 1.3), reducing the alumina to Al and producing carbon dioxide ( $\text{CO}_2$ ), an important greenhouse gas, at the anodes [9]. The overall chemical reaction can be written as [2]:



The decomposition voltage needed for the overall reaction, Eq. 1.1, is 1.2 V [2,

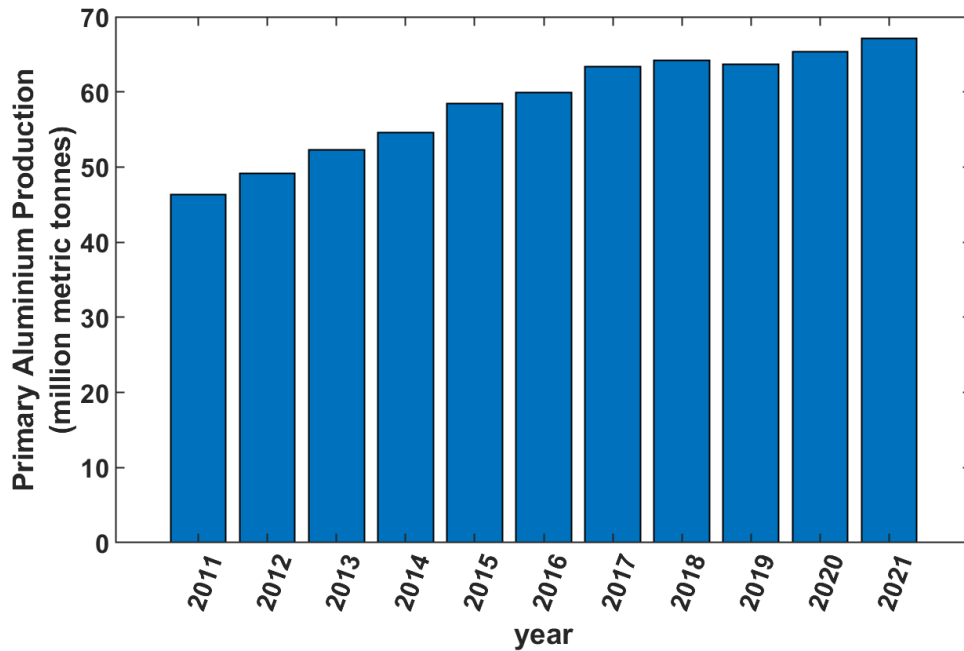


**Figure 1.2:** Primary Aluminium metal production from 2011 to 2021. Data is from International Aluminium [1]

13], and the carbon anodes consumed by the reaction need to be replaced every 20 days [20]. An Al smelter usually contains hundreds of electrolysis cells, where the cells are electrically connected in series, and positioned in long rows known as potlines (see Fig. 1.4) [2]. An array of conductor busbars carries the current between the cells and, due to the large currents, generates a strong magnetic field  $\sim 0.01$  T, about  $200\times$  Earth's magnetic field [2, 20]. Since both the electrolyte and Al layers are conducting and carrying current, electromagnetic forces are generated moving the fluid layer and deforming the Al-electrolyte interface [20].

## 1.2 Energy Consumption of Al Production

Producing Aluminium through electrolysis cells is energy intensive, and Al smelters are usually located next to large power plants. In fact, producing all the Al in

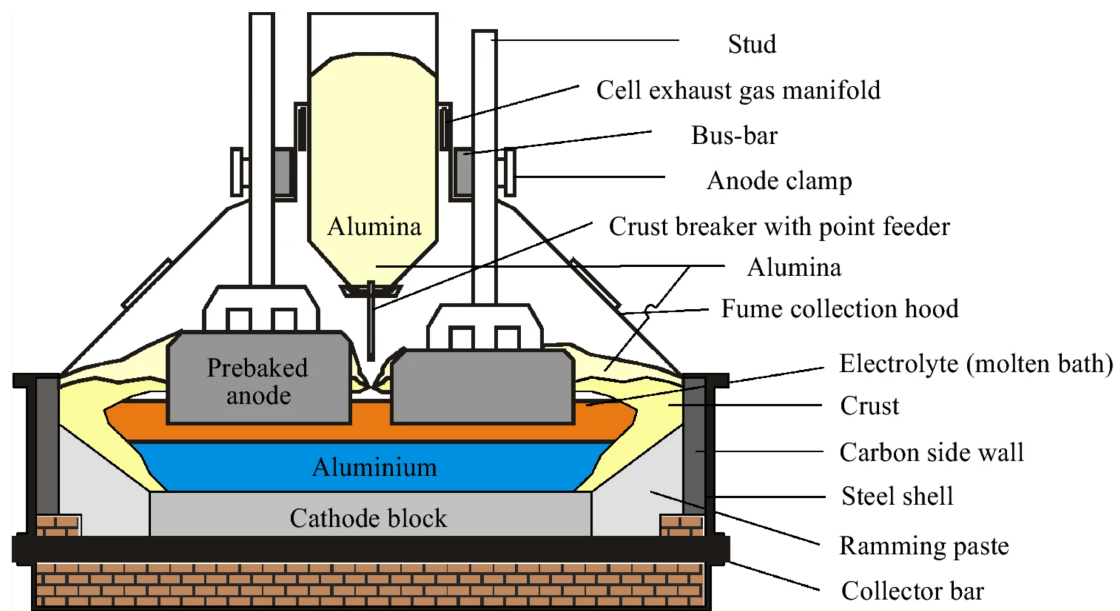


**Figure 1.3:** Schematic of a cross-section of an Aluminium electrolysis cell. These electrolysis cells rely on the Hall-Héroult process to produce aluminium metal. Reprinted by permission from Springer Nature Customer Service Centre GmbH: Springer Nature, *SN Applied Sciences*, “A review of primary aluminium tapping models”, Kitungwa Kabezya et al (2019) [15]



**Figure 1.4:** Picture of a potline of Al electrolysis cells. Reprinted by permission from Wolters Kluwer Health, Inc: from Halvor Kvande and Per Drabløs, “The Aluminum Smelting Process and Innovative Alternative Technologies”, *Journal of Occupational and Environmental Medicine* (2014) [16]

2021 required 843 TWh of electrical energy [3], about 3.4% of the total global electrical energy consumption that year [4] and a fifth of the U.S. [24]. To shed more light on the high energy consumption, it is helpful to look at the energy required to produce one kg of Al, commonly known as the cell's specific energy consumption (SEC) [13]:

$$\text{SEC} = \frac{298 \times V_{\text{cell}}}{\text{CE}} \quad (1.2)$$

where SEC is in (kWh/kg),  $V_{\text{cell}}$  is the Al cell's total voltage in V and CE is the cell's current efficiency as a percentage. Briefly, CE is the ratio of actual Al production rate to the theoretical Al production rate [2, 7] and in most modern cells is above 90% [2, 25]. On the other hand, a typical cell voltage  $V_{\text{cell}}$  is well above the decomposition voltage of 1.2 V and is between 4 and 5 V [2], commonly 4.1 – 4.2 V [13].  $V_{\text{cell}}$  can be broadly decomposed as [2, 26]:

$$V_{\text{cell}} = V_{\text{decomposition}} + V_{\text{anode}} + V_{\text{cathode}} + V_{\text{electrolyte}} + V_{\text{external}} + \eta_{\text{over}} \quad (1.3)$$

where  $V_{\text{anode}}$  is the voltage drop in the anode including the drop due to the gas bubbles,  $V_{\text{cathode}}$  is the voltage drop in the cathode,  $V_{\text{external}}$  is the voltage drop in the electrical busbar connections outside each cell,  $V_{\text{electrolyte}}$  is the voltage drop due to the electrical resistance of the electrolyte, and  $\eta_{\text{over}}$  is the additional voltage required by the kinetics at the electrodes and a results from concentration gradients and surface reactions at the electrodes [2, 26]. For example, the voltage constituents in Eq. 1.3 for an Al cell presented in [13] are given in Table 1.1. From this example, it becomes clear that poor electrical resistance of the electrolyte is the main source of energy loss, as it contributes about 48% of this cell's voltage, and consequently SEC, yet this energy produces no Al and is wasted in the form of heat in the electrolyte. For most cells, this Ohmic heat loss is at about 50%, and is proportional to the electrical resistance ( $R_e$ ) of the electrolyte, which is given by:

$$R_e = \frac{h_e}{\sigma_e A} \quad (1.4)$$

where  $h_e$  is the electrolyte height,  $\sigma_e$  is the electrolyte's electrical conductivity, and  $A$  is the cross-sectional area.  $\sigma_e$  is a material property dictated by the electrolyte's chemistry and is constant, and  $A$  is dictated by the electrolysis cell design and is fixed. Thus, the only way to reduce the electrical resistance of the electrolyte would be to reduce the electrolyte height, which is quantified by the anode-cathode distance (ACD) in industry; the average electrolyte depth from the surface of the anode [27]. Decreasing (or squeezing) the ACD would improve the cell's energy efficiency, and seems quite easy to do at first glance, however when the ACD is decreased below a certain critical threshold, the cell becomes unstable [6, 8, 28–32]. In a process known as the metal pad instability (MPI) [33], electromagnetic forces amplify small perturbations on the Al-electrolyte interface, causing a circulating traveling wave that can grow exponentially until the cell sashes out of control or the Al shorts to the anode [9].

Understanding the cell behaviour and the reasons behind the instability are of great importance. Since the cell operates at a high temperature [22] and the electrolyte is highly corrosive [2], conducting experiments is hard, and coupled mathematical models and numerical simulations are needed [20]. A complete model would account for the many physical phenomena present, coupling chemical, thermal, and magnetohydrodynamic (MHD) effects [20]. Yet, when the instability is present, industrial observations showed that low frequency oscillations, with periods ranging from a few seconds to a minute, are present in the cell voltage and correspond to waves observed on the Al-electrolyte interface [20, 28, 34]. On such short periods, the chemical reactions of electrolysis, temperature changes, and thermal convection are not fast enough to affect the behaviour of the cell [20]. Thus, modelling the magnetohydrodynamics of the Al electrolysis cell is key for understanding this instability.

$V_{\text{decomposition}}$	$V_{\text{anode}}$	$V_{\text{cathode}}$	$V_{\text{external}}$	$V_{\text{electrolyte}}$	$\eta_{\text{over}}$
1.2	0.494	0.3	0.16	1.64	0.579

**Table 1.1:** Voltage sources in (V) for an Al electrolysis cell that operates at 93%  $CE$  and has 4.373 V cell voltage. Data is from Reference [13]. The specific energy consumption of this cell is 14 kWh/(kg Al).

## 1.3 Equations of Magnetohydrodynamics in Al Electrolysis Cells

### 1.3.1 Equations of Electrodynamics

Let be  $\mathbf{E}$ ,  $\mathbf{B}$ ,  $\mathbf{J}$  denote the electric field, magnetic field, and the current density, respectively. Then, Maxwell's equations of electrodynamics [35] for both conducting fluid layers, the molten electrolyte and molten Al, are:

$$\nabla \cdot \mathbf{E} = \frac{\rho_e}{\epsilon_0} \quad (1.5)$$

$$\nabla \times \mathbf{B} = \mu \left( \mathbf{J} + \frac{\epsilon_0 \partial \mathbf{E}}{\partial t} \right) \quad (1.6)$$

$$\nabla \times \mathbf{E} = -\frac{\partial \mathbf{B}}{\partial t} \quad (1.7)$$

$$\nabla \cdot \mathbf{B} = 0 \quad (1.8)$$

where  $\mu$  is the magnetic permeability,  $\epsilon_0$  is the electric permittivity of free space, and  $\rho_e$  is the charge density. The material properties are assumed to be constant in space and time here for each fluid layer. Eq. 1.5 is Gauss' law, Eq. 1.6 is Amperé's law, Eq. 1.7 is Faraday's law of induction, and Eq. 1.8 reflects that the  $\mathbf{B}$  is solenoidal (no magnetic monopoles). The equations of electrodynamics are supplemented with the electromagnetic force equation

$$\mathbf{f} = q (\mathbf{E} + \mathbf{u} \times \mathbf{B}) \quad (1.9)$$

where  $\mathbf{f}$  is the force per unit charge and  $\mathbf{u}$  is the velocity field. Eq. 1.9 tells us that a charge experiences a force from the presence of the total electric field  $\mathbf{E}$ , which includes both the electrostatic field and the electric field induced by a time-varying magnetic field (Eq. 1.7), and a force from the charge's movement within the magnetic field  $\mathbf{B}$  [35]. To find the bulk force acting the conducting fluid, we can sum Eq. 1.9 over a unit volume of the conducting fluid to find:

$$\mathbf{F} = \rho_e \mathbf{E} + \mathbf{J} \times \mathbf{B} \quad (1.10)$$

where  $\mathbf{F}$  is the force per unit volume. In addition to Eqs. 1.5-1.8, one more constitutive relation is needed for  $\mathbf{J}$  which is Ohm's law [36],  $\mathbf{J} = \sigma \mathbf{E}$ , reflecting that the current density is proportional to the force experienced by the free charges in a stationary conductor [35]. Since the fluid layers are moving, we must consider  $\mathbf{E}$  in a frame of reference moving with the conducting fluid. Thus,

$$\mathbf{J} = \sigma(\mathbf{E} + \mathbf{u} \times \mathbf{B}). \quad (1.11)$$

### Common Simplifications in MHD

Taking the divergence,  $(\nabla \cdot)$ , of Eq. 1.6 and substituting Eq. 1.5 we get:

$$\nabla \cdot \mathbf{J} = -\frac{\partial \rho_e}{\partial t} \quad (1.12)$$

which describes the charge conservation in the conducting fluid. Taking the divergence of Ohm's law Eq. 1.11 and substituting Eq. 1.12 and Eq. 1.5 we find [35]:

$$\frac{\partial \rho_e}{\partial t} + \frac{\rho_e}{\tau_e} + \sigma \nabla \cdot (\mathbf{u} \times \mathbf{B}) = 0 \quad (1.13)$$

where  $\tau_e = \epsilon_0/\sigma$  is the charge relaxation time. For  $\sigma_{al} = 325 \times 10^4$  S/m in the Al [37],  $\sigma_e = 250$  S/m in the electrolyte [20], and  $\epsilon_0 = 8.85 \times 10^{-12}$  F/m,  $\tau_e$  is  $\sim 10^{-18}$  s in the Al layer, and  $\sim 10^{-14}$  s is the electrolyte. Since we are interested in phenomena on a time scale between a few seconds to a minute, much longer

than  $\tau_e$  in either fluid layer, then  $\frac{\partial \rho_e}{\partial t}$  can be neglected when compared to  $\frac{\rho_e}{\tau_e}$  [35]. Thus, Eq. 1.13 and Eq. 1.12 reduce to:

$$\rho_e = -\epsilon_0 \nabla \cdot (\mathbf{u} \times \mathbf{B}) \quad (1.14)$$

$$\nabla \cdot \mathbf{J} = 0 \quad (1.15)$$

Eq. 1.14 indicates that a finite charge density is sustained inside the fluid layers, but it is very small. Consequently, we can neglect the electric force  $\rho_e \mathbf{E}$  compared to the magnetic force  $\mathbf{J} \times \mathbf{B}$  simplifying Eq. 1.10 to:

$$\mathbf{F} = \mathbf{J} \times \mathbf{B} \quad (1.16)$$

Also, comparing the terms on the right hand side of Eq. 1.6 and using Eq. 1.11 [35]:

$$\epsilon_0 \frac{\partial \mathbf{E}}{\partial t} \approx \tau_e \frac{\partial \mathbf{J}}{\partial t} \ll \mathbf{J} \quad (1.17)$$

Thus, Eq. 1.6 reduces to:

$$\nabla \times \mathbf{B} = \mu \mathbf{J} \quad (1.18)$$

In summary, the electrodynamics equations in MHD reduce to:

$$\nabla \times \mathbf{B} = \mu \mathbf{J} \quad (1.19)$$

$$\nabla \cdot \mathbf{J} = 0 \quad (1.20)$$

$$\nabla \times \mathbf{E} = -\frac{\partial \mathbf{B}}{\partial t} \quad (1.21)$$

$$\nabla \cdot \mathbf{B} = 0 \quad (1.22)$$

$$\mathbf{J} = \sigma(\mathbf{E} + \mathbf{u} \times \mathbf{B}) \quad (1.23)$$

$$\mathbf{F} = \mathbf{J} \times \mathbf{B} \quad (1.24)$$

### 1.3.2 Magnetic Induction Equation

Isolating  $\mathbf{E}$  in Eq. 1.23, and substituting Eq. 1.19 for  $\mathbf{J}$ , we find that  $\mathbf{E}$  can be written as [36]

$$\mathbf{E} = \eta \nabla \times \mathbf{B} - \mathbf{u} \times \mathbf{B} \quad (1.25)$$

where  $\eta = 1/\mu\sigma$  is the magnetic diffusivity. Substituting Eq. 1.25 for  $\mathbf{E}$  in Eq. 1.21 we get:

$$\nabla \times (\eta \nabla \times \mathbf{B} - \mathbf{u} \times \mathbf{B}) = -\frac{\partial \mathbf{B}}{\partial t} \quad (1.26)$$

but,

$$\nabla \times \nabla \times \mathbf{B} = \nabla(\nabla \cdot \mathbf{B}) - \nabla^2 \mathbf{B} \quad (1.27)$$

Substituting Eq. 1.27 to Eq. 1.26 and applying Eq. 1.22 yields:

$$\frac{\partial \mathbf{B}}{\partial t} = \eta \nabla^2 \mathbf{B} + \nabla \times (\mathbf{u} \times \mathbf{B}) \quad (1.28)$$

Eq. 1.28 is known as the magnetic induction equation and shows that the evolution of the magnetic field is a result of both the diffusion  $\eta \nabla^2 \mathbf{B}$  and the advection  $\nabla \times (\mathbf{u} \times \mathbf{B})$  of the magnetic field. The normal and tangential components of the magnetic field should be continuous across the Al-electrolyte interface for a non-zero  $\eta$  (i.e. finite electrical conductivity) [36].

### 1.3.3 Fluid Equations

The Al and electrolyte layers are treated as incompressible, immiscible fluids. Thus, the conservation of mass [38]

$$\frac{\partial \rho}{\partial t} + \nabla \cdot (\rho \mathbf{u}) = 0 \quad (1.29)$$

reduces to the continuity equation:

$$\nabla \cdot \mathbf{u} = 0 \quad (1.30)$$

and conservation of momentum gives the Navier-Stokes equation with the Lorentz Force Eq. 1.24 added [38]

$$\rho \left[ \frac{\partial}{\partial t} \mathbf{u} + (\mathbf{u} \cdot \nabla) \mathbf{u} \right] = -\nabla(P) + \rho \nu \nabla^2 \mathbf{u} + \rho \mathbf{g} + (\mathbf{J} \times \mathbf{B}) \quad (1.31)$$

where  $\nu$  is the kinematic viscosity. Substituting Eq. 1.19 into Eq. 1.31 for  $\mathbf{J}$ , and using the identity  $\nabla \times \mathbf{B} \times \mathbf{B} = (\mathbf{B} \cdot \nabla)\mathbf{B} - \nabla \left( \frac{B^2}{2} \right)$ , we get:

$$\rho \left[ \frac{\partial}{\partial t} \mathbf{u} + (\mathbf{u} \cdot \nabla) \mathbf{u} \right] = -\nabla(P) + \rho \nu \nabla^2 \mathbf{u} + \rho \mathbf{g} + \frac{1}{\mu} (\mathbf{B} \cdot \nabla) \mathbf{B} - \nabla \left( \frac{B^2}{2\mu} \right) \quad (1.32)$$

where  $B^2 = \mathbf{B} \cdot \mathbf{B}$ ,  $\frac{1}{\mu} (\mathbf{B} \cdot \nabla) \mathbf{B}$  is known as the magnetic tension, and  $\nabla \left( \frac{B^2}{2\mu} \right)$  is the magnetic pressure. It is often convenient to define the total pressure

$$P_t = P + \frac{B^2}{2\mu}, \quad (1.33)$$

and write Eq. 1.32 as:

$$\rho \left[ \frac{\partial}{\partial t} \mathbf{u} + (\mathbf{u} \cdot \nabla) \mathbf{u} \right] = -\nabla(P_t) + \rho \nu \nabla^2 \mathbf{u} + \rho \mathbf{g} + \frac{1}{\mu} (\mathbf{B} \cdot \nabla) \mathbf{B} \quad (1.34)$$

Notice that Eq. 1.28 and Eq. 1.34 describe the evolution in time and space of the magnetic field  $\mathbf{B}$  and the fluid velocity field  $\mathbf{u}$  and their interaction.

### 1.3.4 Low Magnetic-Reynolds Number Approximation

An important non-dimensional number in MHD is the magnetic Reynolds number  $Rm$  defined as

$$Rm = \frac{UL}{\eta} \quad (1.35)$$

where  $U$  is a characteristic velocity scale and  $L$  is a characteristic length scale.  $Rm$  represents an estimate of the relative importance between the advection of the magnetic field by the velocity to the diffusion of the magnetic field [35, 36]. In the context of induction equation, Eq. 1.28,  $Rm$  estimates the ratio of the terms [36]

$$Rm \approx \frac{|\nabla \times (\mathbf{u} \times \mathbf{B})|}{|\eta \nabla^2 \mathbf{B}|} \quad (1.36)$$

For Al electrolysis cells, a typical flow velocity is about 0.2 m/s [20] and a length scale for the wave motion on the Al-electrolyte interface is the ACD ( $\sim 5$  cm). Also, the magnetic permeability of the molten Al and molten electrolyte can be

taken to be  $\approx \mu_0 = 1.26 \times 10^{-6}$  H/m, and for  $\sigma_{al} = 325 \times 10^4$  S/m in the Al [37],  $\sigma_e = 250$  S/m in the electrolyte [20], The magnetic diffusivity  $\eta$  is  $\sim 0.25$  m<sup>2</sup>/s and  $\sim 3200$  m<sup>2</sup>/s in the Al and electrolyte respectively. Thus, the  $Rm \sim 0.04$  in the Al and  $Rm \sim 3 \times 10^{-7}$  in the electrolyte and in both fluid layers  $Rm \ll 1$ . As such, it is common to assume that the magnetic field is purely diffusive when studying the MHD stability of electrolysis cells

$$\frac{\partial \mathbf{B}}{\partial t} = \eta \nabla^2 \mathbf{B} \quad (1.37)$$

Effectively, this reduces the coupling between  $\mathbf{u}$  and  $\mathbf{B}$ , where  $\mathbf{B}$  is still affecting the fluid velocity field through the Lorentz force, but  $\mathbf{u}$  is not affecting the magnetic field. Furthermore, experimental observations indicate that the period of the wave motion on the Al-electrolyte interface is much greater than the diffusion time of the magnetic field [8, 30], and thus the magnetic field is assumed to be static  $\frac{\partial \mathbf{B}}{\partial t} = 0$ . This, too, is a very popular simplification in the literature and used in many studies of the MHD stability of the Al electrolysis cells [8, 29, 32, 39, 40].

## 1.4 Metal Pad Instability

As motivated by §1.2, being able to reduce the ACD while maintaining the Al electrolysis cell's stability would pave the way towards a more energy efficient production and more profits for Al smelters. Thus, understanding the MHD stability of electrolysis cells through numerical modelling has been an active area of research since 1967 [20, 41] where the governing equations similar to the ones presented in §1.3 are solved analytically or numerically. Some studies established simple qualitative models of the instability mechanism such as the one in [8, 42]. Other studies performed linear stability analysis of a simplified system analytically and then quantified the stability either analytically [39, 43] or numerically [8, 29]. The simplifications used in such studies are sometimes geometrical in nature

such as considering infinitely long and wide cells [44–47], infinitely long or wide cells [48, 49], circular cells [8, 43], rectangular cells [8, 29, 39, 40], or using the shallow water approximation [8, 20, 29, 40, 50]. Other simplifications used pertain to the electromagnetic aspect of the cells such as neglecting induced currents [8, 29], making assumptions about the electrical conductivity ratios [32, 47, 50], and imposed magnetic field [29, 30, 47], or pertain to the fluid dynamic aspect: such as neglecting viscosity and surface tension [8] or replacing their dissipative effect with a damping term [47, 51], or pertain to the equilibrium state the perturbation is done at [8, 29, 39]. Other studies move away from linear stability, and use nonlinear models and numerical simulations to study the stability of the Al electrolysis cell [20, 31, 50, 52].

### 1.4.1 Sele Mechanism

In almost all studies, understanding the mechanism behind the instability and predicting its threshold was the goal. Any proposed theory needed to agree with industrial observations that reducing the ACD, strong vertical magnetic fields, and strong horizontal currents in the Al favor instability [20]. The first widely accepted explanation was developed by Sele in 1977 [28], where the presence of a wave on the Al-electrolyte interface creates a perturbation current that is purely vertical at the wave crests (due to the low electrical conductivity of the electrolyte), and purely horizontal in the Al (due to the high electrical conductivity of the Al). This horizontal perturbation current in the Al interacts with the constant vertical magnetic field to produce a horizontal electromagnetic force in the Al that pushes the wave around [20, 28]. To quantify the stability threshold, one can consider a tilting of the interface as shown in Fig. 1.5. Let  $\tilde{\eta}$  be the interface deformation,  $h_e$  be the ACD, and  $h_{al}$  be the Al layer height. Then, if  $I$  is the current in the

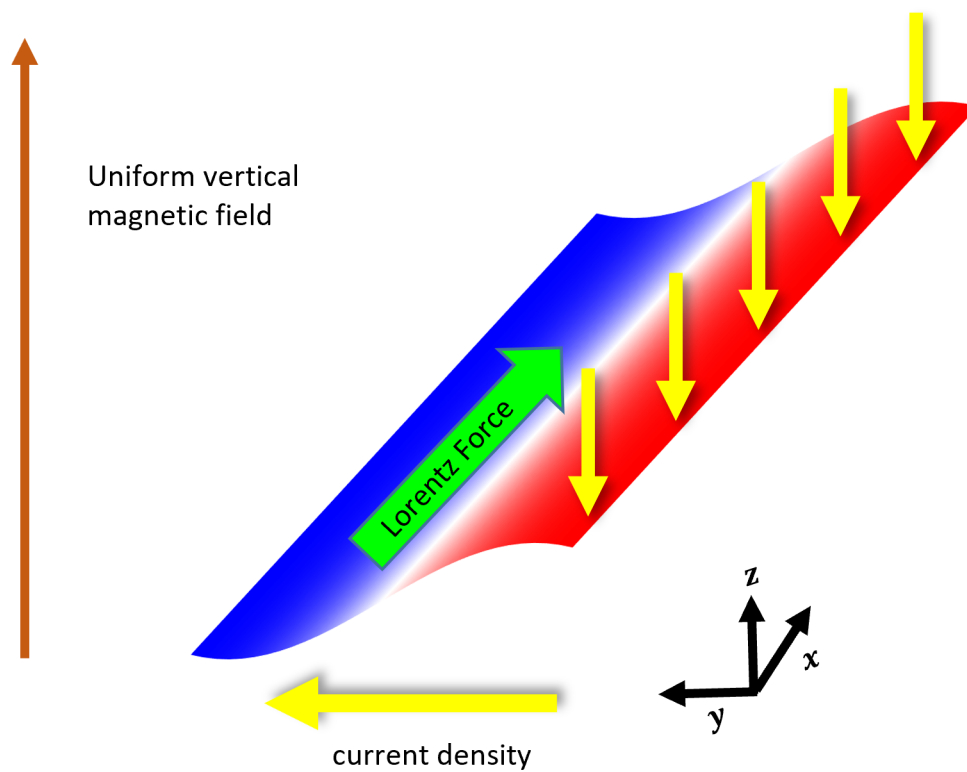


**Figure 1.5:** A representation of the Sele mechanism. The Al-electrolyte interface is plotted when the interface is tilted, red means above flat surface and blue means below. Due to the low conductivity of the electrolyte, a vertical perturbation current (yellow) is created near the wave crest. Due to the high conductivity of the Aluminium, the perturbation current is horizontal there and interacts with the vertical magnetic field to produce a horizontal Lorentz force (green). The Lorentz force pushes the Al moving the wave crest along the side walls of the cell counter clockwise.

cell, the perturbation current in the electrolyte is approximately

$$\frac{I\tilde{\eta}}{h_e} \quad (1.38)$$

this perturbed current then runs horizontally throughout the depth of the Al layer, then, the perturbed current in the Al is approximately [20]

$$\frac{I\tilde{\eta}}{h_e h_{al}} \quad (1.39)$$

Thus, the horizontal electromagnetic force (per unit area) is [20]

$$\frac{IB\tilde{\eta}}{h_e h_{al}} \quad (1.40)$$

where  $B$  is the magnitude of the uniform magnetic field. On the other hand, the interface deformation is subjected to a force (per unit area) due to gravity that is approximately [20]

$$(\rho_{al} - \rho_e)g\tilde{\eta} \quad (1.41)$$

where  $g$  is the gravitational acceleration,  $\rho_{al}$  and  $\rho_e$  are the densities of the Al and electrolyte, respectively. Taking the ratio between these two forces, Eqs.1.40,1.41 results in the Sele criterion [20, 28]

$$\beta_{Sele} = \frac{IB}{h_e h_{al}(\rho_{al} - \rho_e)g} \quad (1.42)$$

The cell is predicted to be stable when  $\beta_{Sele}$  is less than some empirical threshold. The Sele criterion Eq. 1.42 captures many practical observations: decreasing ACD, larger currents, and stronger vertical magnetic fields would increase  $\beta_{Sele}$  and consequently favor instability [20].

## 1.4.2 A Coupling of Interface Wave Modes

Subsequent work [6, 8, 29, 39] generalized Sele's stability criterion, where it was shown that the MPI is caused by a coupled resonance between interface wave

modes on the Al-electrolyte interface. The height of the Al-electrolyte interface varies spatially and can be written in terms of the wave modes as

$$\sum_{m,n} \alpha_{m,n} G_{m,n} = \sum_{m,n} \alpha_{m,n} \cos\left(\frac{m\pi}{L_x}\left(x + \frac{L_x}{2}\right)\right) \cos\left(\frac{n\pi}{L_y}\left(y + \frac{L_y}{2}\right)\right) \quad (1.43)$$

where  $G_{m,n}$  is an interface mode,  $\alpha_{m,n}$  is its amplitude,  $m, n$  are non-negative integers,  $x$  increases along the long axis of the rectangular cell,  $y$  increases along its short axis, and  $(x, y) = (0, 0)$  at the center of the cell. Each  $G_{m,n}$  has the form of a standing wave whose temporal frequency nearly matches the corresponding hydrodynamic gravity wave mode, whose frequency  $f_{m,n}$  [20] is independent of current and (in the limit of shallow cells) is given by

$$f_{m,n}^2 = \frac{(\rho_{Al} - \rho_c)g}{(2\pi)^2\left(\frac{\rho_{Al}}{h_{Al}} + \frac{\rho_e}{h_e}\right)} \left[ \left(\frac{m\pi}{L_x}\right)^2 + \left(\frac{n\pi}{L_y}\right)^2 \right] \quad (1.44)$$

Any perturbation on the Al-electrolyte interface can be written in terms of wave modes  $G_{m,n}$ , and when the Lorentz forces are absent, these modes are decoupled and the perturbations die out [8]. But when the Al cell is operating with a current and magnetic field present, the perturbed current density created by one mode gives rise to a Lorentz Force that can excite many other modes [8]. When two modes have nearly identical frequencies and cause surface motion at right angles (e.g., one with  $m = 0$ , another with  $n = 0$ ), their resonant coupling can give rise to the MPI [6, 33]. As Eq. 1.44 shows, if  $L_x/L_y = 1$ , frequencies of  $m = 0$  and  $n = 0$  modes match exactly; accordingly, the MPI is predicted to occur even with arbitrarily thick electrolyte layers in square or circular cells [9]. Many methods for MPI suppression have been attempted in the past, including inserting baffles in the Al layer [5, 53] or tilting the anode in synchrony with interface motion [5], with limited success. In practice, the MPI is mitigated by keeping the ACD thick and building cells with greater length  $L_x$  than width  $L_y$ . Certain aspect ratios  $L_x/L_y$ , especially those near 2.1, hinder the MPI [40] because it is parametric in nature [9].

## 1.5 Hypothesis and Thesis Overview

Parametric instabilities can often be decoupled by introducing a new frequency that frustrates the resonance, so we hypothesized that adding an oscillation to the current would prevent the MPI [9]. The goal of this thesis is to show that this is true. I start by first testing the hypothesis on a simple mechanical model of the MPI in chapter 2. I extended the simple model of the MPI presented in [8] to include an oscillating current component, and show that this extended model can be stabilized by the added oscillating current. Then, in chapter 3, I show that adding an oscillating current component, with a specific amplitude and frequency, can suppress the MPI in high fidelity numerical simulation of a TRIMET smelter of 180 kA electrolysis cells [54], done on MHD-Valdis software [55], and show that using this technique we were able to reduce the ACD by  $\sim 11\%$  and increase the cell's energy efficiency by 4 % while maintaining stable operation in simulation. Also, I discuss the stabilizing mechanism of the oscillating current which relates to exciting standing waves on the Al-electrolyte interface that oppose the MPI. Finally, in chapter 4, I present an initial assessment of the impact of using the oscillating current on the electrolysis cell's current efficiency. Further, I discuss the impact the choice of the amplitude and the frequency of the oscillating current has on the electrolysis cell stability.

## **2 Stabilizing a Low-Dimensional Model of Magnetohydrodynamic Instabilities in Aluminium Electrolysis Cells**

This chapter is based on Reference [10] and the author's qualifying exam submission. It has been reformatted and edited to fit within the thesis. The thesis author was the primary author on this work.

### **2.1 Introduction**

Davidson and Lindsay [8] proposed a mechanical analogue of the metal pad instability (MPI) in the form of a compound pendulum (see Figure 2.1) that consists of a flat and thin rectangular Al plate (representing the Al layer) that is attached by a rigid strut to a flat surface (representing the anode) with a poor-electrically conducting electrolyte between them. A steady uniform current density (representing the reduction current) flows vertically downwards through the electrolyte

to the Al plate where it is withdrawn from the plate's bottom. The Al plate can swing about both horizontal axes,  $x$  and  $y$ , and an ambient vertical magnetic field  $\mathbf{B}_z$  is imposed. When the electromagnetic forces are absent, the Al plate would oscillate at its natural angular gravitational frequency in each direction,  $\omega_x$  in  $x$  and  $\omega_y$  in  $y$ , and the plate's motion is decoupled [8]. However, due to the poor electrical conductivity of the electrolyte, a slight tilting of the Al plate about one axis, say the  $x$  axis, creates a perturbed current density that is purely vertical in the electrolyte; entering the electrolyte where it is thinnest and leaving where it is thickest. Since the Al plate is a good electrical conductor, the perturbed current density shorts through the plate and is horizontal there. This horizontal perturbed current density interacts with  $\mathbf{B}_z$  to create a horizontal electromagnetic force that pushes the Al plate in the  $y$  direction. This, in turn, is a situation where another horizontal electromagnetic force is created that pushes the Al plate back in the  $x$  direction. Thus, the electromagnetic forces couple the Al plate's motion in the  $x$  and  $y$  directions and, if strong enough, can make the Al plate oscillations grow in time [8].

This is quite similar to the MPI in Al electrolysis cells where the electromagnetic forces couple two or more interfacial gravity wave modes of similar frequencies [6, 8, 28–30, 33, 39] as explained in §1. Indeed, the stability of the Al plate's motion as different parameters are varied offers an accurate *qualitative* understanding of what would happen in an Al electrolysis cell if the same parameters were varied: larger currents, stronger vertical magnetic fields, smaller ACD, and electrolysis cells with horizontal aspect ratio closer to 1 are more unstable [8, 29, 39]. Since the pendulum model captures much of the essential physics of the MPI in Al electrolysis cells, it was a great starting point to test our hypothesis of whether an oscillating current can stop the MPI. Specifically, I wanted to study whether a slightly different model, one with an added oscillating current density with a specific frequency and amplitude, can stabilize an unstable Al plate motion.

This chapter proceeds as follows: In §2.2 I present a slightly extended mechanical model, one with an oscillating current density component, with a specific normalized amplitude and angular frequency, added to the steady current density. I also present the simplifying assumptions used with justification based on real Al electrolysis cell conditions. In §2.3, I derive the Al plate equations of motion in detail outlining where the simplifying assumptions are used and all approximations utilized. In §2.4, I present numerical solutions for the Al plate's motion for different cases. First, I consider the case of no electromagnetic coupling where the motion in  $x$  and  $y$  directions is decoupled and well known, serving as a good sanity check. Next, I consider the case of only steady current which was originally studied in [8] and the stability criterion identified. I show that the numerical solution accurately depicts the results of [8], and derive the stability criterion analytically. Finally, I solve for the Al plate's motion when the oscillating current density component is present and show that a previously unstable Al plate motion can be stabilized via the oscillating component. Further, I present the stability of the Al plate at different oscillating current density normalized amplitude and angular frequency combinations, and examine how the stability of those pairs changes when the model is driven further into the unstable regime. In §2.5, I summarize the results and discuss some limitations of the model, implications of the results, and potential future directions.

## 2.2 Mechanical Model

Consider the compound pendulum placed in a Cartesian coordinate system as shown in Figure 2.1. It consists of a solid Al plate of density  $\rho_{al}$  and dimensions  $L_x$ ,  $L_y$ , and  $H$  in the  $x$ ,  $y$  and  $z$  directions respectively, attached to a fixed electrode surface by a strut of height  $h_0$  and negligible mass. The strut pivots, allowing the Al plate to swing about both the  $x$  and  $y$  axes. The gap,  $h(x, y)$ , between

the Al plate and the electrode surface is filled with a poor-electrically conducting electrolyte, and a vertical magnetic field  $\mathbf{B}_z$  is imposed as shown. To this point the model is exactly the same as the one described in [8]. A current density,  $\mathbf{J}_0$ , passes vertically downwards through the electrolyte to the Al plate where it is collected, and consists of a steady component and a sinusoidal oscillating component:

$$\mathbf{J}_0 = J_0(1 + \beta \sin(\omega_b t))(-\hat{\mathbf{e}}_z) \quad (2.1)$$

where  $J_0$  is the steady current density amplitude,  $\beta$  is the ratio of the oscillating current amplitude to that of the steady current, and  $\omega_b$  is the angular frequency of the oscillating current.  $\sigma_{al}$ ,  $\sigma_e$  are the electrical conductivities of the Al plate and electrolyte, respectively.

### 2.2.1 Simplifying Assumptions

Following the same consideration as in [8] and in accordance to real Al electrolysis cell conditions, I use the following simplifying assumptions:

1. The Al plate and electrolyte are broad and shallow such that  $(H, h_0) \ll (L_x, L_y)$ . This accurately depicts the geometry of an Al electrolysis cell where the shallow water approximation [56] is often used to simplify the hydrodynamic problem [29–31, 40, 57].
2. The perturbation in the electrolyte thickness,  $\Delta h$ , is very small such that  $\Delta h \ll h_0$ . Solving for the plate's motion in time under this a perturbation would show whether the plate's motion is stable or not. As for Al electrolysis cells, this translates to studying the stability of small amplitude wave perturbations which are readily present due to gravity disturbances on the Al-electrolyte interface [8, 29, 39]
3. The Al plate's periods of oscillations are much greater than the magnetic field diffusion time. This assumption agrees with experimental observations

from Al electrolysis cells where the characteristic time for the wave motion on the Al-electrolyte interface is much greater than the magnetic field diffusion time in electrolysis cells [30]. This implies that the current relaxes to a new equilibrium as the Al-electrolyte interface moves [8].

4. The fixed wall has a fixed potential  $\Phi_0$  i.e. it is an equipotential surface. This is similar to what is commonly assumed about the carbon anodes in an Al electrolysis cell since the anodes have a much higher electrical conductivity, about 100 times [6] more, than that of the electrolyte. A detailed formal derivation of this approximation can be found in [47].
5. The perturbed current density,  $\mathbf{j}$ , is purely vertical in the electrolyte. This can be justified by the electrolyte having a much lower electrical conductivity than Al plate, about 10000 times [6], and the shallow nature of the electrolyte. This also is commonly assumed for Al electrolysis cell and a formal derivation can be found in [20, 39].
6. The Al plate is treated as an equipotential surface with potential  $\Phi = 0$  and the perturbed current  $\mathbf{j}$  is purely horizontal in it. This is due to the Al layer having a much higher electrical conductivity than the electrolyte and cathode in an Al cell and the shallow nature of the layers which make the perturbed current “short” through the Al layer.
7. The perturbed current in the Al plate is much higher than the perturbed current in the electrolyte. Thus, we neglect the perturbed electromagnetic forces in the electrolyte. This is the case in Al electrolysis cell due to the shallow water approximation of Assumption 1 [8].
8. The damping effects such as viscosity are ignored. Damping effects have a stabilizing effect and ignoring them would be a worst case scenario when studying the instability.

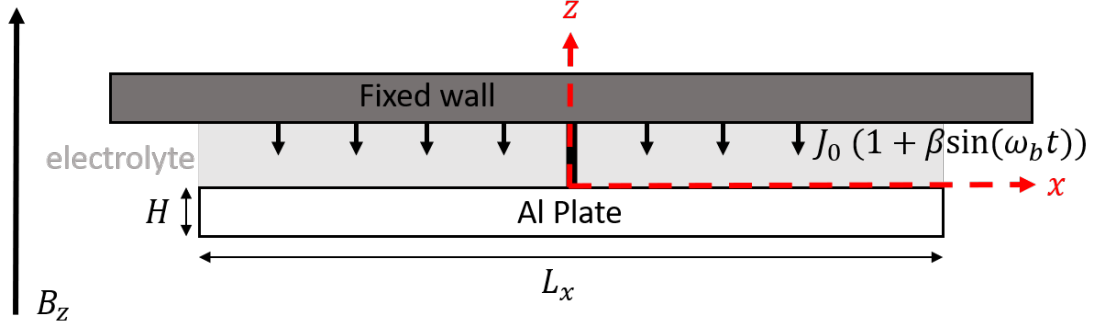


**Figure 2.1:** Schematic diagram of the compound pendulum model. The pendulum can swing about both the  $x$  and  $y$  axes, with the  $x$ -axis as shown and the  $y$ -axis pointing into the page.

9. The magnetic field induced by  $\mathbf{j}$  is very small compared to the imposed magnetic field  $\mathbf{B}_z$  and is neglected [8, 29].
10. We assume that the imposed magnetic field is vertical and constant:  $\mathbf{B}_z = B_0 \hat{\mathbf{e}}_z$ . This is a simplification and in actual Al cells the magnetic field is more complex [6].
11. The inertia of the electrolyte is ignored [8].

## 2.3 Deriving Equations of Motion

In what follows, I use superscript “e” for quantities related to the electrolyte and “al” for quantities related to the Al plate, and subscripts to indicate the direction. For example,  $\mathbf{j}_z^e$  refers to the perturbed current density in the electrolyte along the  $z$ -direction. Also,  $\hat{\mathbf{e}}_x, \hat{\mathbf{e}}_y, \hat{\mathbf{e}}_z$  are unit vectors along the  $x, y$  and  $z$  directions, respectively. At equilibrium, the Al plate is stationary, the thickness of the electrolyte  $h(x, y) = h_0$  is constant, and the current density  $\mathbf{J}_0 = J_0(1 + \beta \sin(\omega_b t))(-\hat{\mathbf{e}}_z)$ .

Small rotational perturbations of  $\theta_x$  and  $\theta_y$  are then applied to the plate about the  $x$  and  $y$  axes respectively. Let  $\Delta h_x$  be the perpendicular distance from the

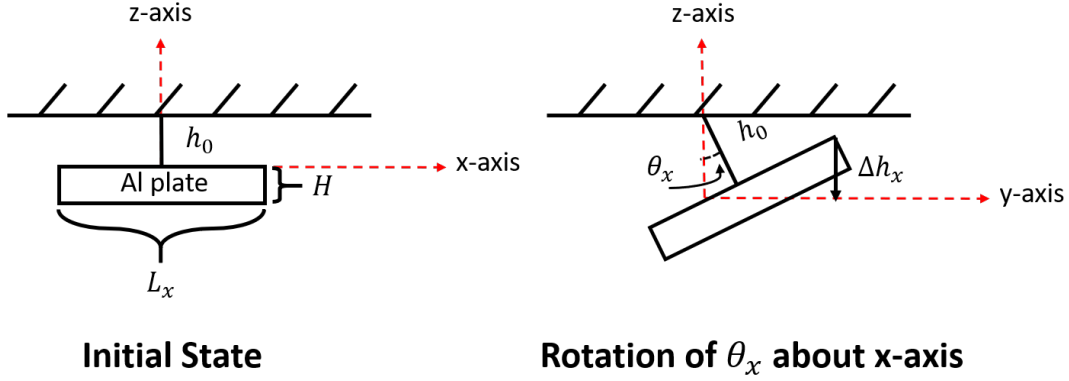


**Figure 2.2:** Pendulum model at initial unperturbed state, and under small rotation about  $x$ -axis

top of the plate to the  $y$ -axis (see Figure 2.2). Then, the angle between the Al plate and the  $y$ -axis is  $\theta_x$  and thus

$$\tan \theta_x = \frac{\Delta h_x}{y}, \quad (2.2)$$

but, for small  $\theta_x$ ,  $\tan \theta_x \approx \theta_x$  so  $\Delta h_x \approx y\theta_x$ . Similarly, if  $\Delta h_y$  is the perpendicular distance from the top of the plate to the  $x$ -axis, then  $\Delta h_y \approx x\theta_y$ . Notice that a rotation of  $\theta_x$  decreases the electrolyte thickness by  $\Delta h_x$  while a rotation of  $\theta_y$  increases the electrolyte thickness by  $\Delta h_y$ . Hence, the perturbed electrolyte thickness is given by

$$h(x, y) = h_0 + \Delta h_y - \Delta h_x \approx h_0 + x\theta_y - y\theta_x. \quad (2.3)$$

### 2.3.1 Perturbed current density in the electrolyte

Assumption 3 and Faraday's law of induction [20, 35] imply that the electric field is irrotational and thus can be represented as the gradient of a scalar potential  $\Phi$ . Using assumptions 2, 4, and 6, the potential in the electrolyte varies linearly across its depth from  $\Phi_0$  at the top wall, to 0 at the Al plate. Thus, using Eq. 2.3, the potential in the electrolyte is

$$\Phi(x, y, z) = \frac{\Phi_0 z}{h(x, y)} = \frac{\Phi_0 z}{h_0 + x\theta_y - y\theta_x}. \quad (2.4)$$

Let  $\mathbf{J}^e = \mathbf{J}_0 + \mathbf{j}^e$  denote the total current density in the electrolyte, where  $\mathbf{j}^e$  is the perturbed current density in the electrolyte. Since  $\mathbf{J}_0$  is purely vertical and so is  $\mathbf{j}^e$  by assumption 5, then  $\mathbf{J}^e$  must be purely vertical. Therefore, using Ohm's law [20, 35] and Eq. 2.4 I find the the total current density in the electrolyte to be:

$$\mathbf{J}^e = -\sigma \frac{\partial \Phi}{\partial z} (-\hat{\mathbf{e}}_z) = -\sigma \frac{\Phi_0}{h_0 + x\theta_y - y\theta_x} (-\hat{\mathbf{e}}_z). \quad (2.5)$$

When  $\theta_x = 0 = \theta_y$ , the Al plate is at equilibrium by definition and  $\mathbf{J}^e = \mathbf{J}_0 = \frac{-\sigma \Phi_0}{h_0} (-\hat{\mathbf{e}}_z)$  from Eq. 2.5. Thus, Eq. 2.5 can be written as:

$$\mathbf{J}^e = \frac{J_0(1 + \beta \sin(\omega_b t))h_0}{h_0 + x\theta_y - y\theta_x} (-\hat{\mathbf{e}}_z). \quad (2.6)$$

Now I can find the perturbed current density in the electrolyte:

$$\begin{aligned} \mathbf{j}^e &= \mathbf{J}^e - \mathbf{J}_0 \\ &= \left( \frac{-J_0(1 + \beta \sin(\omega_b t))h_0}{h_0 + x\theta_y - y\theta_x} + J_0(1 + \beta \sin(\omega_b t)) \right) (\hat{\mathbf{e}}_z) \\ &= J_0(1 + \beta \sin(\omega_b t)) \left( \frac{x\theta_y - y\theta_x}{h_0 + x\theta_y - y\theta_x} \right) (\hat{\mathbf{e}}_z). \end{aligned} \quad (2.7)$$

Let  $\epsilon = x\theta_y - y\theta_x$ . Then, the Taylor expansion of  $\frac{\epsilon}{h_0 + \epsilon}$  around  $\epsilon = 0$  gives

$$\frac{\epsilon}{h_0 + \epsilon} \approx 0 + \frac{h_0 + \epsilon - \epsilon}{(h_0 + \epsilon)^2} \Big|_{\epsilon=0} (\epsilon - 0) + O(\epsilon^2) \approx \frac{\epsilon}{h_0}. \quad (2.8)$$

Using Eq. 2.8 the perturbed current density in the electrolyte can be approximated as

$$\mathbf{j}^e \approx \frac{J_0(1 + \beta \sin(\omega_b t))(x\theta_y - y\theta_x)}{h_0} (\hat{\mathbf{e}}_z) = j^e (\hat{\mathbf{e}}_z). \quad (2.9)$$

### 2.3.2 Net flow of perturbed current in the Al plate

I want to calculate the net flow of perturbed current within the Al plate, and start by stating the boundary conditions for  $\mathbf{j}^{al}$ , the perturbed current density in the Al plate:

1.  $\mathbf{j}_z^{al} \Big|_{z=0} = \mathbf{j}_z^e,$
2.  $\mathbf{j}_x^{al} \cdot \hat{\mathbf{n}} \Big|_{\text{side boundary}} = 0 = \mathbf{j}_y^{al} \cdot \hat{\mathbf{n}} \Big|_{\text{side boundary}}$
3.  $\mathbf{j}_z^{al} \Big|_{z=-H} = \mathbf{0}.$

where  $\hat{\mathbf{n}}$  is an outwards unit normal vector to the Al plate's sides. Boundary condition 1 asserts that the perturbed current density is continuous across the electrolyte-Al plate interface. Boundary condition 2 implies that the side of the Al plate act as electrical insulators. This mimics the situation in an Al electrolysis cell, where the cell sides are made from refractory material that has a much lower electrical conductivity than the molten Al. A detailed derivation of this boundary condition can be found in [47]. Boundary condition 3 implies that the perturbed current density does not penetrate the Al plate and a consequence of assumption 6.

There are no free charges in the Al plate, so

$$\nabla \cdot \mathbf{j}^{al} = \frac{\partial j_x^{al}}{\partial x} + \frac{\partial j_y^{al}}{\partial y} + \frac{\partial j_z^{al}}{\partial z} = 0. \quad (2.10)$$

I integrate both sides in  $z$  and apply boundary conditions 1 and 3 to find

$$\begin{aligned} \int_{-H}^0 \frac{\partial j_x^{al}}{\partial x} dz + \int_{-H}^0 \frac{\partial j_y^{al}}{\partial y} dz + \int_{-H}^0 \frac{\partial j_z^{al}}{\partial z} dz &= 0 \\ \implies \int_{-H}^0 \frac{\partial j_x^{al}}{\partial x} dz + \int_{-H}^0 \frac{\partial j_y^{al}}{\partial y} dz + j_z^{al} \Big|_H^0 &= 0 \\ \implies \int_{-H}^0 \frac{\partial j_x^{al}}{\partial x} dz + \int_{-H}^0 \frac{\partial j_y^{al}}{\partial y} dz &= -j^e. \end{aligned} \quad (2.11)$$

Then, integrating Eq. 2.11 in  $y$ , and applying boundary condition 2 yields

$$\begin{aligned} \int_{-L_y/2}^{L_y/2} \int_{-H}^0 \frac{\partial j_x^{al}}{\partial x} dz dy + \int_{-L_y/2}^{L_y/2} \int_{-H}^0 \frac{\partial j_y^{al}}{\partial y} dz dy &= \int_{-L_y/2}^{L_y/2} -j^e dy \\ \implies \int_{-L_y/2}^{L_y/2} \int_{-H}^0 \frac{\partial j_x^{al}}{\partial x} dz dy + \cancel{\int_{-H}^0 j_y^{al} \Big|_{-L_y/2}^{L_y/2} dz} &= \int_{-L_y/2}^{L_y/2} -j^e dy \\ \implies \int_{-L_y/2}^{L_y/2} \int_{-H}^0 \frac{\partial j_x^{al}}{\partial x} dz dy &= - \int_{-L_y/2}^{L_y/2} j^e dy. \end{aligned} \quad (2.12)$$

Integrate Eq. 2.12 in  $x$  from some  $x'$  to  $\frac{L_x}{2}$  and applying 2 gives

$$\begin{aligned}
-\int_x^{L_x/2} \int_{-L_y/2}^{L_y/2} j^e dy dx &= \int_{x'}^{L_x/2} \int_{-L_y/2}^{L_y/2} \int_{-H}^0 \frac{\partial j_x^{al}}{\partial x} dz dy dx' \\
&= \int_{-L_y/2}^{L_y/2} \int_{-H}^0 \int_{x'}^{L_x/2} \frac{\partial j_x^{al}}{\partial x} dx' dz dy \\
&= \int_{-L_y/2}^{L_y/2} \int_{-H}^0 -j_x^{al}(x') dz dy \\
&= -I_x^{al}(x'), \tag{2.13}
\end{aligned}$$

where  $I_x^{al}$  represents the net flow of perturbed current in the  $x$  direction within the Al plate. Therefore, using Eq. 2.13 and substituting Eq. 2.9

$$I_x^{al}(x) = \int_x^{L_x/2} \int_{-L_y/2}^{L_y/2} j^e dy dx = \frac{J_0(1 + \beta \sin(\omega_b t))(\theta_y L_y)}{2h_0} \left[ \left( \frac{L_x}{2} \right)^2 - x^2 \right]. \tag{2.14}$$

Using the same procedure, the net flow of perturbed current along  $y$  inside of the Al plate can be found as:

$$I_y^{al}(y) = \int_y^{L_y/2} \int_{-L_x/2}^{L_x/2} j^e dx dy = -\frac{J_0(1 + \beta \sin(\omega_b t))(\theta_x L_x)}{2h_0} \left[ \left( \frac{L_y}{2} \right)^2 - y^2 \right]. \tag{2.15}$$

### 2.3.3 Applying Newton's second law of rotation

Having found the net perturbed current in the Al plate, I can now find the torques due to the perturbed electromagnetic force. The horizontal perturbed currents within the aluminium plate interact with the imposed vertical magnetic field,  $\mathbf{B}_z = B_0(\hat{\mathbf{e}}_z)$ , giving rise to a horizontal perturbed electromagnetic force per unit volume:

$$\mathbf{f} = \mathbf{j}^{al} \times \mathbf{B}_z. \tag{2.16}$$

Writing Eq. 2.16 component wise:

$$\mathbf{f}_x = j_y^{al} B_0 (\hat{\mathbf{e}}_x), \tag{2.17}$$

$$\mathbf{f}_y = -j_x^{al} B_0 (\hat{\mathbf{e}}_y). \tag{2.18}$$

$$\mathbf{f}_z = 0 \tag{2.19}$$

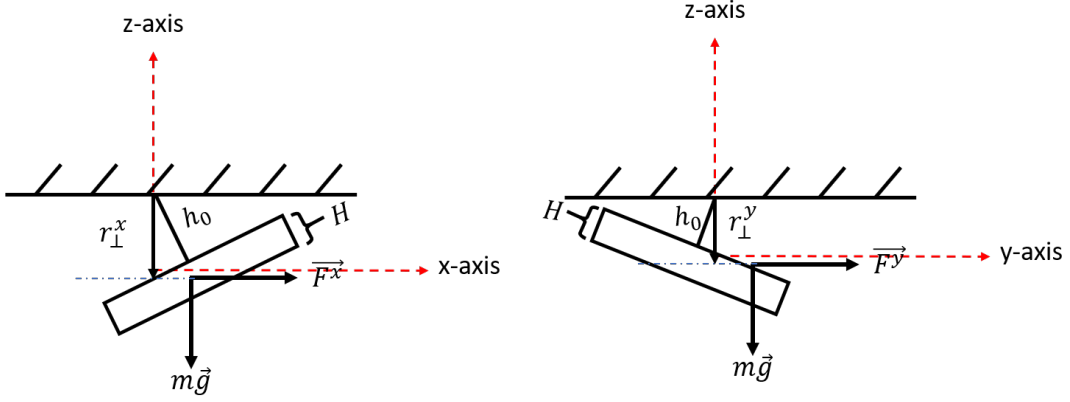


**Figure 2.3:** Only the electromagnetic and gravitational forces have a net non-zero torque with respect to the pivot.

Integrating Eq. 2.17 in  $x$  and  $z$ , I find the distribution of the electromagnetic force in the  $x$  direction,  $\mathbf{F}_x(y)$ , in  $N/m$ :

$$\begin{aligned} \int_{-L_x/2}^{L_x/2} \int_{-H}^0 \mathbf{f}_x \, dz \, dx &= \int_{-L_x/2}^{L_x/2} \int_{-H}^0 j_y^{al} B_0 (\hat{\mathbf{e}}_x) \, dz \, dx \\ \implies \mathbf{F}_x(y) &= I_y^{al}(y) B_0(\hat{\mathbf{e}}_x) \end{aligned} \quad (2.20)$$

Similarly, integrating Eq. 2.18 in  $y$  and  $z$ , I find the distribution of the electromagnetic force in the  $y$  direction  $\mathbf{F}_y(x)$ :

$$\begin{aligned} \int_{-L_y/2}^{L_y/2} \int_{-H}^0 \mathbf{f}_y \, dz \, dy &= \int_{-L_y/2}^{L_y/2} \int_{-H}^0 -j_x^{al} B_0 (\hat{\mathbf{e}}_y) \, dz \, dy \\ \implies \mathbf{F}_y(x) &= -I_x^{al}(x) B_0(\hat{\mathbf{e}}_y) \end{aligned} \quad (2.21)$$

Substituting Eq. 2.14 into Eq. 2.20 and Eq. 2.15 into Eq. 2.21, I get:

$$\begin{aligned} \mathbf{F}_x(y) &= I_y^{al}(y) B_0(\hat{\mathbf{e}}_x) = -\frac{J_0 B_0 (1 + \beta \sin(\omega_b t)) (\theta_x L_x)}{2h_0} \left[ \left( \frac{L_y}{2} \right)^2 - y^2 \right] (\hat{\mathbf{e}}_x), \quad (2.22) \\ \mathbf{F}_y(x) &= -I_x^{al}(x) B_0(\hat{\mathbf{e}}_y) = -\frac{J_0 B_0 (1 + \beta \sin(\omega_b t)) (\theta_y L_y)}{2h_0} \left[ \left( \frac{L_x}{2} \right)^2 - x^2 \right] (\hat{\mathbf{e}}_y). \end{aligned} \quad (2.23)$$

Referring to Figure 2.3, the distributions of the torques arising from the electro-

magnetic forces about the pivot, along the  $x$  and  $y$  directions respectively, are

$$\tau_x(x) = r_\perp^x F_y(x) (-\hat{\mathbf{e}}_z \times \hat{\mathbf{e}}_y) = (h_0 + \frac{H}{2}) F_y(x) (\hat{\mathbf{e}}_x), \quad (2.24)$$

$$\tau_y(y) = r_\perp^y F_x(y) (-\hat{\mathbf{e}}_z \times \hat{\mathbf{e}}_x) = -(h_0 + \frac{H}{2}) F_x(y) (\hat{\mathbf{e}}_y). \quad (2.25)$$

The net torques are obtained by integrating Eq. 2.24 along the  $x$  direction and Eq. 2.25 along the  $y$  direction:

$$\tau_x^{\text{net}} = \int_{-L_x/2}^{L_x/2} \tau_x(x) dx = -(h_0 + \frac{H}{2}) \frac{J_0 B_0 (1 + \beta \sin(\omega_b t)) (\theta_y L_y) (L_x)^3}{h_0 12} (\hat{\mathbf{e}}_x), \quad (2.26)$$

$$\tau_y^{\text{net}} = \int_{-L_y/2}^{L_y/2} \tau_y(y) dy = (h_0 + \frac{H}{2}) \frac{J_0 B_0 (1 + \beta \sin(\omega_b t)) (\theta_x L_x) (L_y)^3}{h_0 12} (\hat{\mathbf{e}}_y). \quad (2.27)$$

With the net torques due to the perturbed electromagnetic force found, I can derive the Al plate's equations of motion by considering the conservation of angular momentum about the horizontal axes parallel to  $x$  and  $y$  axes when the Al plate is at  $\theta_x = 0 = \theta_y$ , and passing through the pivot. As shown in Figure 2.3, the only torques acting on the plate are the ones due to the electromagnetic and gravity forces, so using Newton's second law for rotation in each direction is

$$I_{xx} \alpha_x = \sum \tau = \tau_x^{\text{net}} + \tau_x^{\text{gravity}}, \quad (2.28)$$

$$I_{yy} \alpha_y = \sum \tau = \tau_y^{\text{net}} + \tau_y^{\text{gravity}}, \quad (2.29)$$

Where  $\alpha_x = \ddot{\theta}_x \hat{\mathbf{e}}_x$  and  $\alpha_y = \ddot{\theta}_y \hat{\mathbf{e}}_y$  are the angular accelerations with  $\ddot{(\ )}$  indicating the second derivative in time,  $I_{xx}$  and  $I_{yy}$  are the moments of inertia of the rectangular Al plate simplified via assumption 1:

$$I_{xx} = \rho_a L_x L_y H \left[ \frac{L_y^2}{12} + \cancel{\frac{H^2}{12}} + (h_0 + \cancel{\frac{H}{2}})^2 \right], \quad (2.30)$$

$$I_{yy} = \rho_a L_x L_y H \left[ \frac{L_x^2}{12} + \cancel{\frac{H^2}{12}} + (h_0 + \cancel{\frac{H}{2}})^2 \right], \quad (2.31)$$

and  $\boldsymbol{\tau}_x^{\text{gravity}}, \boldsymbol{\tau}_y^{\text{gravity}}$  are the torques due to gravity

$$\boldsymbol{\tau}_x^{\text{gravity}} = \mathbf{r}_\perp \times m\mathbf{g} = \rho_{al}L_xL_yHg(h_0 + \frac{H}{2})\theta_x (-\hat{\mathbf{e}}_x) \quad (2.32)$$

$$\boldsymbol{\tau}_y^{\text{gravity}} = \mathbf{r}_\perp \times m\mathbf{g} = \rho_{al}L_xL_yHg(h_0 + \frac{H}{2})\theta_y (-\hat{\mathbf{e}}_y) \quad (2.33)$$

Substituting Eqs. 2.26, 2.27, 2.30, 2.31, 2.32, and 2.33 into 2.28 and 2.29 and rearranging yields

$$\ddot{\gamma}_x + \omega_x^2 \gamma_x = -a(1 + \beta \sin(\omega_b t))\gamma_y, \quad (2.34)$$

$$\ddot{\gamma}_y + \omega_y^2 \gamma_y = a(1 + \beta \sin(\omega_b t))\gamma_x, \quad (2.35)$$

where  $\gamma_x = \frac{\theta_x}{L_x^2}$  and  $\gamma_y = \frac{\theta_y}{L_y^2}$  are normalized angles,  $\omega_x^2 = \frac{g(h_0 + \frac{H}{2})}{L_y^2/12}$  and  $\omega_y^2 = \frac{g(h_0 + \frac{H}{2})}{L_x^2/12}$  are the natural angular frequencies of the pure gravitational oscillations squared, in the  $x$  and  $y$  directions respectively, and  $a = \frac{(h_0 + H/2)J_0B_0}{\rho_{al}Hh_0}$ . The parameter  $a$  is what couples the motion in the  $x$  and  $y$  directions, as shown by the right hand side of Eqs. 2.34, 2.35, and is directly proportional to the electromagnetic force  $J_0B_0$ .

## 2.4 Numerical Solution

Before solving the equations of motion Eqs. 2.34 and 2.35, I had to choose the system parameters. I chose values that reasonably mimic the lateral dimensions and fluid layer thickness of Al electrolysis cells [50]. I set the Al plate dimensions to  $H = 0.2$  m,  $h_0 = 0.045$  m,  $L_x = 11$  m, and  $L_y = 2.7$  m and used  $g = 9.81$  m/s<sup>2</sup>. Based on these dimensions, I calculated the natural angular gravitational frequencies of the Al plate to be  $\omega_x = 1.5302$  rad/s and  $\omega_y = 0.3756$  rad/s.

Then, I wrote the system of Equations Eqs. 2.34 and 2.35 in matrix form as:

$$\dot{\mathbf{X}} = \mathbf{A}(t)\mathbf{X} \quad (2.36)$$

where  $\mathbf{A}(t)$  is the coefficient matrix of the form

$$\begin{bmatrix} 0 & 0 & 1 & 0 \\ 0 & 0 & 0 & 1 \\ -\omega_x^2 & -a(1 + \beta \sin(\omega_b t)) & 0 & 0 \\ a(1 + \beta \sin(\omega_b t)) & -\omega_y^2 & 0 & 0 \end{bmatrix} \quad (2.37)$$

and  $\mathbf{X}$  is the state variable

$$\begin{bmatrix} \gamma_x \\ \gamma_y \\ \dot{\gamma}_x \\ \dot{\gamma}_y \end{bmatrix} \quad (2.38)$$

I solved Eq. 2.36 numerically using a 4th order Runge-Kutta based solver in MATLAB “ode45.m”. I initialized the solver using the conditions of small rotations  $\theta_x, \theta_y$  and zero angular velocities  $\dot{\theta}_x = 0 = \dot{\theta}_y$ .

### 2.4.1 No coupling case, $a = 0$

As a sanity check, I first solved for the simple case of  $a = 0$  which decouples the Al plate’s motion in the  $x$  and  $y$  directions. This can be thought of as having no current at all,  $J_0 = 0$ , or no magnetic field,  $B_0 = 0$ , which implies that there is no electromagnetic forces present. The equations of motion reduce to:

$$\ddot{\gamma}_x + \omega_x^2 \gamma_x = 0, \quad (2.39)$$

$$\ddot{\gamma}_y + \omega_y^2 \gamma_y = 0, \quad (2.40)$$

and admit solutions:

$$\gamma_x \approx \cos(\omega_x t) \quad (2.41)$$

$$\gamma_y \approx \cos(\omega_y t) \quad (2.42)$$

In this case, gravitational forces are only present and the Al plate would oscillate with angular frequency  $\omega_x$  in the  $x$  direction and  $\omega_y$  in the  $y$  direction. Since there

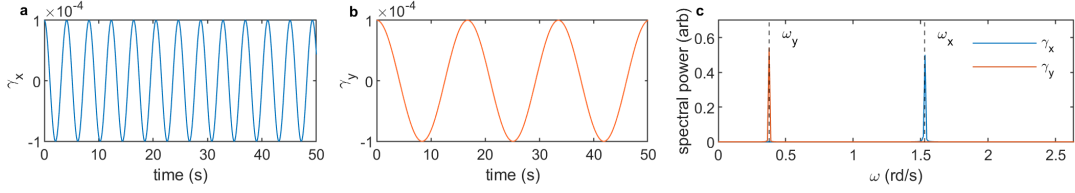


**Figure 2.4:** Numerical solutions for the decoupled case  $a = 0$ . **a**,  $\gamma_x$  oscillates in time at a single frequency. **b**,  $\gamma_y$  oscillates in time at a single frequency that is lower than that of  $\gamma_x$ . **c** The power spectrum of both  $\gamma_x$  and  $\gamma_y$  shows that each oscillates exactly at its pure angular gravitational frequency.

is no damping mechanism (assumption 8), I expect the amplitude of oscillations to stay constant in time. The numerical solution shows the expected results (Fig. 2.4).  $\gamma_x$  and  $\gamma_y$  are pure oscillations (Fig. 2.4a-b) with constant amplitude, and the power spectrum of each shows that the oscillations' angular frequencies coincide with  $\omega_x$  and  $\omega_y$  (Fig. 2.4c).

### 2.4.2 Steady current case, $\beta = 0$

Next, I solved for the steady current case by setting  $\beta = 0$  which eliminates the oscillatory component of the current. This case was originally studied in [8]. The equations of motion in this case reduce to:

$$\ddot{\gamma}_x + \omega_x^2 \gamma_x = -a, \quad (2.43)$$

$$\ddot{\gamma}_y + \omega_y^2 \gamma_y = a, \quad (2.44)$$

Let  $\gamma^+ = \gamma_x + \gamma_y$  and  $\gamma^- = \gamma_x - \gamma_y$ . Taking the sum and difference of Eqs. 2.43 and 2.44, and re-writing in terms of  $\gamma^+$  and  $\gamma^-$  yields:

$$\ddot{\gamma}^+ + \omega_x^2 \frac{\gamma^+ + \gamma^-}{2} + \omega_y^2 \frac{\gamma^+ - \gamma^-}{2} = a\gamma^- \quad (2.45)$$

$$\ddot{\gamma}^- + \omega_x^2 \frac{\gamma^+ + \gamma^-}{2} - \omega_y^2 \frac{\gamma^+ - \gamma^-}{2} = -a\gamma^+ \quad (2.46)$$

Rearranging Eqs. 2.45 and 2.46:

$$\ddot{\gamma}^+ + \bar{\omega}^2 \gamma^+ = (a - \omega_c) \gamma^- \quad (2.47)$$

$$\ddot{\gamma}^- + \bar{\omega}^2 \gamma^- = (-a - \omega_c) \gamma^+ \quad (2.48)$$

where  $\bar{\omega}^2 = \frac{\omega_x^2 + \omega_y^2}{2}$  and  $\omega_c = \frac{\omega_x^2 - \omega_y^2}{2}$ . To check the stability of the motion described by Eqs. 2.47 and 2.48, I looked for a solution of the form  $\gamma^+ \sim e^{i\omega t}$  and  $\gamma^- \sim e^{i\omega t}$ . Substituting yields:

$$(-\omega^2 + \bar{\omega}^2) \gamma^+ = (a - \omega_c) \gamma^- \quad (2.49)$$

$$(-\omega^2 + \bar{\omega}^2) \gamma^- = (-a - \omega_c) \gamma^+ \quad (2.50)$$

which in matrix form is:

$$\begin{bmatrix} -\omega^2 + \bar{\omega}^2 & \omega_c - a \\ \omega_c + a & -\omega^2 + \bar{\omega}^2 \end{bmatrix} \begin{bmatrix} \gamma^+ \\ \gamma^- \end{bmatrix} = \begin{bmatrix} 0 \\ 0 \end{bmatrix} \quad (2.51)$$

For a non-trivial solution, the coefficient matrix of Eq. 2.51 must be singular i.e. have a zero determinant. Thus,

$$\begin{aligned} (-\omega^2 + \bar{\omega}^2)^2 - \omega_c^2 + a^2 &= 0 \\ \implies -\omega^2 + \bar{\omega}^2 &= \pm \sqrt{\omega_c^2 - a^2} \\ \implies \omega^2 &= \bar{\omega}^2 \mp \sqrt{\omega_c^2 - a^2} \end{aligned} \quad (2.52)$$

If  $\omega^2$  has a complex component, then the motion is unstable. From Eq. 2.52, this is the case when

$$\begin{aligned} \omega_c^2 - a^2 &< 0 \\ \implies a &> |\omega_c| \end{aligned} \quad (2.53)$$

Thus, transition to instability occurs when the coupling parameter  $a$  exceeds a critical value of:

$$a_{\text{crit}} = \left| \frac{\omega_x^2 - \omega_y^2}{2} \right| \quad (2.54)$$

This agrees with the critical coupling parameter presented in [8] where the case of steady current was originally studied. Furthermore, Eq. 2.54 shows that the initial separation of the natural gravitational angular frequencies,  $\omega_x$  and  $\omega_y$ , is of great importance to the stability of the system [8]. As such, having the length  $L_x$  be greater than the width  $L_y$  is desired. This accurately captures the situation in Al electrolysis cells, where they are designed to have a much greater length than width to hinder the MPI [9, 40]. Going back to Eq. 2.52, it becomes clear that the electromagnetic forces bring the motion's angular frequencies of oscillations closer to one another, until they converge to  $\bar{\omega}$  [8].

For the values of  $\omega_x$  and  $\omega_y$  here, the critical coupling parameter  $a_{\text{crit}} = 1.100206$ . First, I solved for the Al plate's motion for a case with coupling slightly below the critical value by setting  $a = 1.100205$ . The numerical solutions are presented in Fig. 2.5a-c.  $\gamma_x$  oscillates stably and the amplitude is enveloped by a slowly varying oscillation (Fig. 2.5a); the beating phenomenon is present. Plotting only the first 50 seconds (Fig. 2.5b) shows the oscillations happening at a higher frequency inside the amplitude envelope.  $\gamma_y$  behaves the same as  $\gamma_x$  (Fig. 2.5c). Then, I solved for a case with coupling slightly above the critical value by setting  $a = 1.100207$ . The numerical solutions are presented in Fig. 2.5d-f.  $\gamma_x$  is unstable with the amplitude growing exponentially in time (Fig. 2.5d).  $\gamma_x$  reaches  $\sim 25000$ , which would exceed  $\theta_x = \pi/2$  and definitely violate the small-angle approximation. So, the normalized angles shouldn't be taken literally but the exponential growth in amplitude is really an indicator of instability. Plotting only the first 50 seconds (Fig. 2.5e) shows the oscillations of  $\gamma_x$ .  $\gamma_y$  is also unstable (Fig. 2.5f). The numerical solutions for both cases matched what was expected from the stability condition of Eq. 2.54.

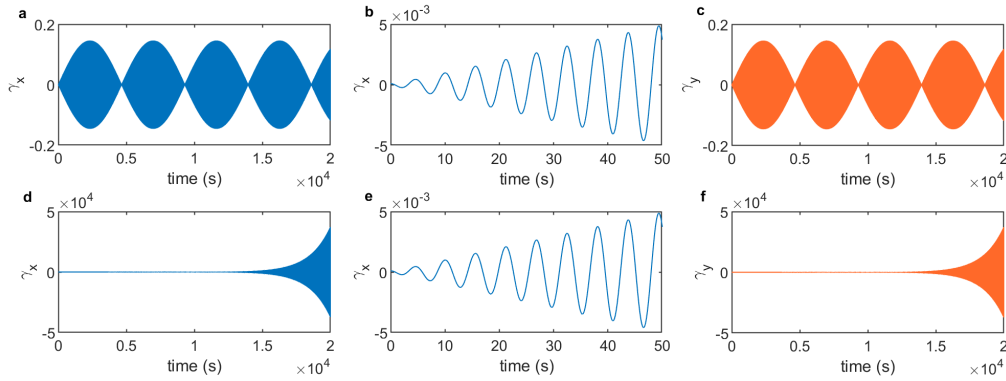


**Figure 2.5:** Numerical solutions at  $a$  slightly above and below  $a_{\text{crit}}$ . **a**,  $a = 1.100205$ , the Al plate is stable with  $\gamma_x$  oscillating in time and beating phenomenon is present. The regions appearing solid blue indicate oscillations too fast to be individually visible. **b**, an enlargement of the same data as (a) plotted for only 50 s. The oscillations inside the amplitude envelope can now be seen. **c**,  $\gamma_y$  is also stable, behaving the same as  $\gamma_x$ . **d**,  $a = 1.100207$ , the Al plate is unstable with the amplitude of  $\gamma_x$  increasing exponentially in time. The regions appearing solid blue indicate oscillations too fast to be individually visible. **e**, an enlargement of the same data as (d) plotted for only 50 s. **f**,  $\gamma_y$  is also unstable, behaving the same as  $\gamma_x$ .

### 2.4.3 Oscillating current added

I solved again for  $a = 1.100207$  but with an oscillating current present ( $\beta \neq 0$ ). I checked the stability of  $\gamma_x$  and  $\gamma_y$  for a range of oscillating currents, each with a different amplitude and frequency. I found that using an oscillating current with  $\omega_b = 0.94$  rd/s and  $\beta = 0.1$  (10% of the steady current amplitude) stabilized the motion, where  $\gamma_x$  (Fig. 2.6a-b) and  $\gamma_y$  no longer grew in time. The power spectrum of  $\gamma_x$  shows two dominant angular frequencies present: one near the oscillating current angular frequency of 0.94 rd/s, and the other near the root-mean-square of the natural gravitational frequencies,  $\bar{\omega}$ , of  $\sim 1.1$  rd/s (Fig. 2.6c). Having a peak near  $\omega_b$  present in the power spectrum indicates that the oscillating current successfully altered the dynamics of the Al plate by injecting a new angular frequency to the Al plate's motion.

I summarized the stability at  $a = 1.100207$  for different pairs of oscillating

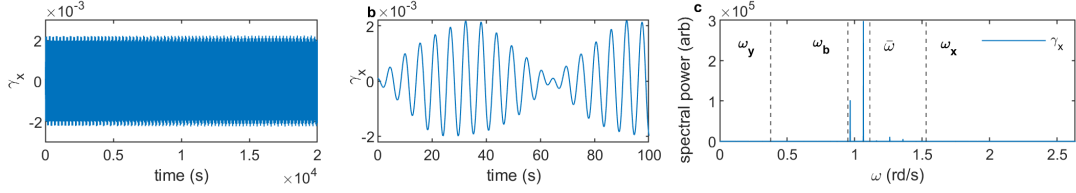


**Figure 2.6:** Numerical solutions at  $a = 1.100207$  with an oscillating current of  $\beta = 0.1$  and  $\omega_b = 0.94$  rd/s. **a**,  $\gamma_x$  oscillating in time stably. The regions appearing solid blue indicate oscillations too fast to be individually visible. **b**, an enlargement of the same data as (a) plotted for only 100 s. The oscillations inside the amplitude envelope can now be seen. **c**, The power spectrum of  $\gamma_x$  shows two frequencies, one near the oscillating frequency.

amplitude and frequency,  $(\beta, \omega_b)$ , in Fig. 2.7, where I varied  $\beta$  from 0.01 to 0.9 in steps of 0.01 and  $\omega_b$  from 0 rd/s to 12 rd/s in steps of 0.1 rd/s. At  $\omega_b = 0$  rd/s, the current is only steady and the Al plate motion is expected to be unstable for all  $\beta$ . This is the case indicated by the column of blue dots at  $\omega_b = 0$  rd/s in Fig. 2.7. For  $\omega_b \neq 0$ , two distinct regions of stability emerge. One near lower angular frequencies that almost looks like a triangle whose base is centered at  $\sim 1$  rd/s (region 1). Having a lower amplitude seems to be better for stability in that region. The other region is much bigger and at higher frequencies and seems to be bounded by two curves, one of which is almost a vertical line at  $\omega_b \sim 2.5$  rd/s (region 2). At higher frequencies, a higher amplitude seems to better. Overall, the  $(\beta, \omega_b)$  phase space portrait looks like Arnold tongues [58]. I increased the coupling parameter by 3% to  $a = 1.133213$ , pushing the Al plate motion further into the unstable regime. The  $(\beta, \omega_b)$  phase space portrait is presented in Fig. 2.8. Far fewer stable combinations exist compared to Fig. 2.7, where only the upper sides of region 1 retained stability and region 2 collapsed into a single line vertical line at  $\omega_b \sim 2.5$  rd/s starting at  $\beta = 0.25$ . All of the previously stable combinations with  $\beta < 0.1$  are now unstable, alluding to more unstable motion will require a higher oscillation current amplitude to be stabilized.

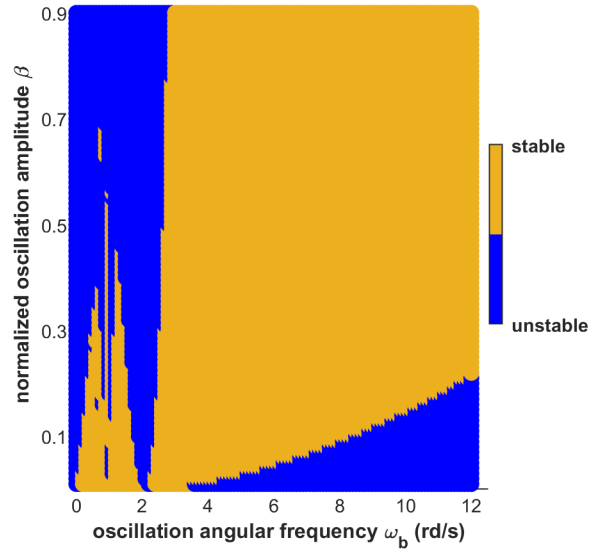


**Figure 2.7:**  $(\beta, \omega_b)$  phase space for  $a = 1.100207$ . The motion is stable for many pairs of the oscillating current's angular frequency and normalized amplitude. The stable pairs cluster at two distinct regions.

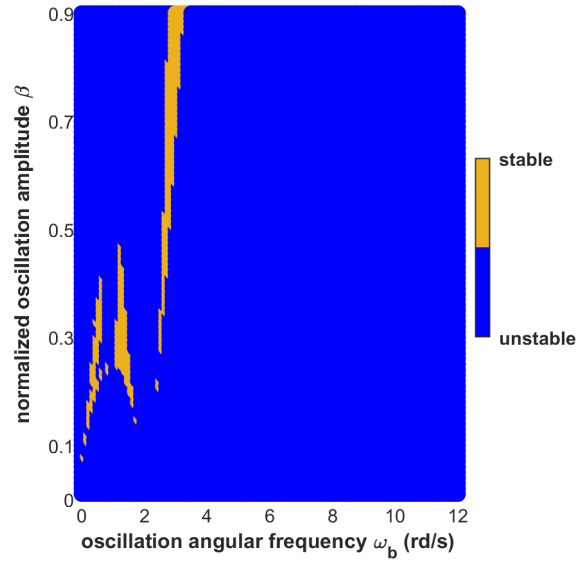


**Figure 2.8:**  $(\beta, \omega_b)$  phase space for  $a = 1.133213$ . The motion remains stable for only a few pairs of the oscillating current's angular frequency and normalized amplitude.

## 2.5 Summary and Future Work

In this chapter, I extended the mechanical model of the MPI presented in [8] to include an additional oscillating current component with a specific angular frequency and amplitude, to test whether the oscillating current component can stabilize it. I derived equations of motion for the model, Eqs. 2.34,2.35, a coupled system of second order ordinary differential equations. I solved the equations of motion numerically for three distinct cases: no coupling, steady current, and added oscillating current. The numerical solutions agreed with what is expected for the no coupling case and the steady current case originally studied in [8]. Also, I showed that adding the oscillating current stabilized a previously unstable motion with the steady current only. Various angular frequency,  $\omega_b$ , and normalized amplitude,  $\beta$ , combinations for the oscillating current worked for stabilizing the motion and the stability depends in a complicated way on  $\omega_b$ , where distinct regions of stability of emerge. The regions of stability are significantly smaller for a model that is more unstable i.e. has a higher coupling parameter  $a$ .

The choice of model dimensions,  $H$ ,  $h_0$ ,  $L_x$ , and  $L_y$  was to mimic similar dimensions in an Al electrolysis cells. Changing any of the dimensions would change the natural gravitational frequencies and consequently the critical coupling parameter  $a_{\text{crit}}$ . When I solved for the Al plate's motion, I would set the value of the coupling parameter  $a$  rather than calculating it for values of  $J_0$  and  $B_0$  that would be similar to those in Al electrolysis cells. Doing so would have given  $a$  values so low that the Al plate is always stable. Thus, the results of from this mechanical model should be only considered in a qualitative rather than a quantitative manner when translating them to Al electrolysis cell applications. For example, having a larger aspect ratio of  $L_x/L_y$  would increase the difference between the natural gravitational angular frequencies and consequently indicate a more stable scenario. This translates well to Al cells where a large aspect ratio

is desired for stability [29].

Also, the mechanical model reduces the real two fluid layer system in Al electrolysis cells from one with an infinite number of degrees of freedom to one with only two. In Al cells there are many gravitational frequencies and many couplings between them can occur to trigger the MPI [6, 29, 30, 33]. The mechanical model also fails to account for damping effects in Al cells, such as viscosity and the friction between the fluid layer and the electrode, which would most certainly impact stability. Adding a friction coefficient to the model would make it better mimic an Al cell.

The system of Eqs. 2.34, 2.35 is canonically a periodic linear differential equation system, Eq. 2.36 where the matrix  $A(t)$  is periodic with period  $T = \frac{2\pi}{\omega_b}$ , and belong to a family of equations known as Mathieu equations [59]. Analytical techniques such as Floquet theory [59, 60] can be used to study the stability of the system and perhaps outline the distinct stable regions present in the  $(\beta, \omega_b)$  phase space for a given coupling parameter  $a$ .

## 2.6 Acknowledgements

This chapter is based on “Stabilizing a Low-Dimensional Model of Magnetohydrodynamic Instabilities in Aluminum Electrolysis Cells” which was printed in the book *Light Metals 2022* [10], and has been modified to fit in this thesis. The thesis author is the primary author and was responsible for deriving the model’s equations of motion, writing the MATLAB code to numerically solve the equations of motion, and writing the paper. The thesis author prepared all the figures, except Fig. 2.2 and Fig. 2.3 which were prepared by co-author Douglas Kelley. Co-author Douglas Kelley came up with the idea of extending the mechanical model of the MPI to test the stabilizing effect of adding an oscillating current, provided guidance on deriving the equations of motion, on developing the numer-

ical solution algorithm, on figure formation, and edited the paper. Conversations with Riccardo Betti and Marc Dupuis offered valuable insights. This work was supported by the National Science Foundation (CBET-1552182).

# 3 Stabilizing Aluminium Electrolysis Cells via Oscillating Currents in Simulation

This chapter is based primarily on Reference [9] and some content from Reference [7]. They have been reformatted and edited to fit within the thesis. The thesis author is the primary author of this work.

## 3.1 Introduction

In chapter 2, I showed that a mechanical model of the MPI [8] can be extended to include an oscillating current density component, and that this oscillating component can stabilize the model [10]. Since the oscillating current worked in stabilizing the model, we were optimistic that it would work in Al electrolysis cells, and the next thing we set out to do was to test if it would stop the MPI in a high fidelity numerical simulation of an Al electrolysis cell.

To study the stability of a typical Al electrolysis cell under the influence of an oscillating current, we used the simulation package MHD-Valdis, a tool widely

used in the industry to design stable aluminum electrolysis cells. MHD-Valdis uses a generalized MHD shallow layer, non-linear wave model based on [29, 52, 55, 61–66]. It dynamically couples the transient turbulent motion of each fluid layer and the interface shape to the transient magnetic field and electric currents in the cell [55]. The model includes essential commercial cell features such as the electrolyte channels [64], electric current distribution in the busbars, and the magnetic field generated by the ferromagnetic cell elements [55], and has been validated against a benchmark model [67] in [63] and against measurements from the TRIMET 180 kA commercial potline [68] and other commercial cells [69, 70]. A model of the same TRIMET 180 kA commercial potline, in commercial use by TRIMET Aluminum, SE, in Germany, is used in our stabilization study (see Fig. 3.1). These cells normally operate at 4.5 cm anode-to-cathode distance (ACD) and have been simulated in previous studies that validated the model with real-world measurements [54, 68, 71].

### 3.1.1 Boundary Conditions

The electric network of MHD-Valdis represents several pots in the potline and includes the bus bar network elements. So the current density at the bottom of the anodes and on the surface of the cathode blocks is part of the electrical network solution, and changes in time with the interface shape [11]. At the Al cell’s side walls a zero normal current is applied, which implies that the side walls are assumed to be electric insulators. Also, continuity of the electric potential and the normal current component are asserted across the Al-electrolyte interface. The hydrodynamic boundary conditions used are continuity of pressure across the Al-electrolyte interface and zero normal velocity at the side walls.

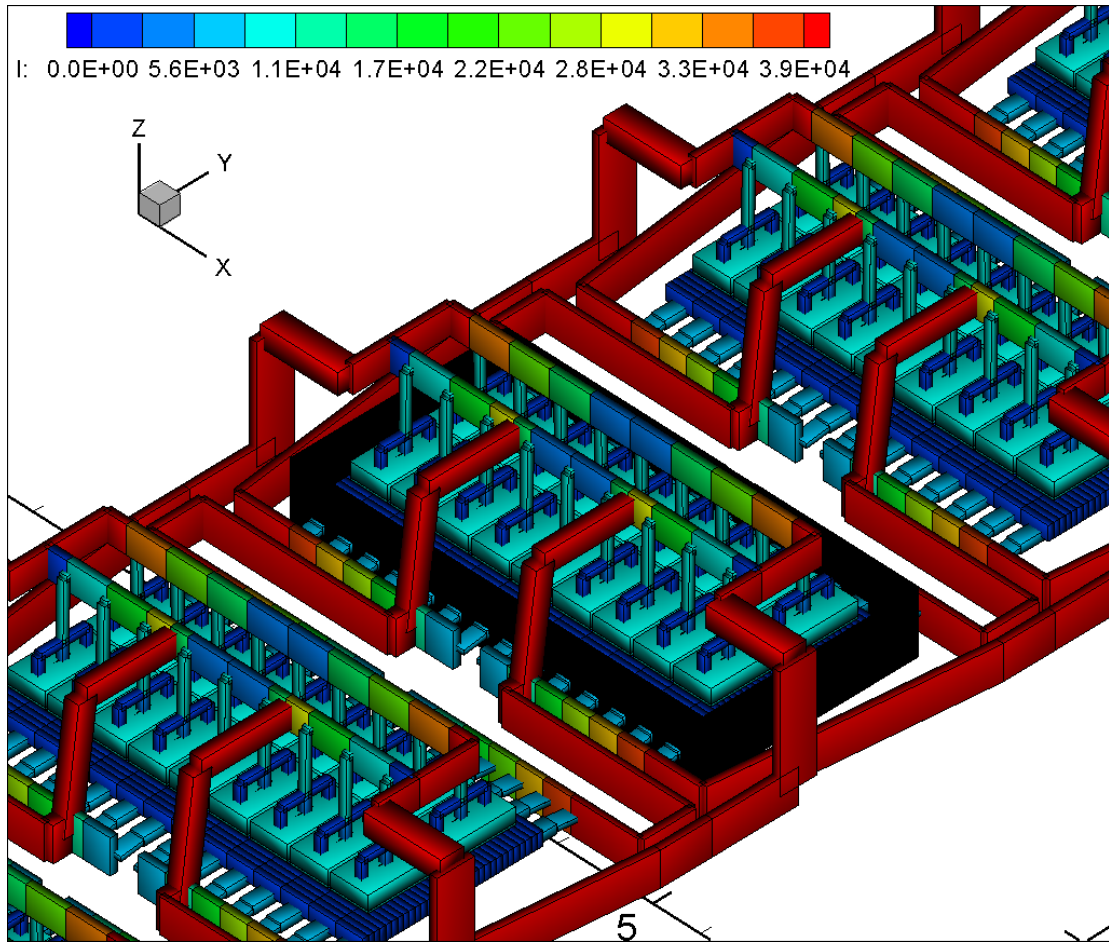


**Figure 3.1:** Snapshot of the TRIMET 180 kA potline model from MHD-Valdis software showing busbar layout. Color represents the current,  $I$ , in each conductor in Ampere (A). Figure is courtesy of Dr. Marc Dupuis.

molten Al	molten electrolyte	carbon anode	carbon cathode
$4 \times 10^6$	233	20450	74074

**Table 3.1:** Electrical conductivities,  $\sigma$ , of the fluid layers and carbon anodes used in the simulation in S/m.

layer	$\rho$ (kg/m <sup>3</sup> )
molten Al	2300
molten electrolyte	2075

**Table 3.2:** Density of the molten Al and electrolyte layers used in the simulations.

### 3.1.2 Simulation Setup

The TRIMET 180 kA Al electrolysis cell modelled in our simulations has lateral dimensions,  $L_x \times L_y = 7.92 \times 3.57$  m, and we use a numerical grid having  $N_x \times N_y = 87 \times 31$  elements, so the grid size is  $9.21 \times 11.90$  cm. The electrical conductivities used for the Al layer and electrolyte layer are presented in Table 3.1, and their densities in Table 3.2. The Al layer has a fixed height of 17 cm. The electrical conductivities of the carbon anodes and cathodes are also presented in Table 3.1.

The interface shape is initialized with the  $G_{1,0}$  interface mode as a perturbation with an amplitude of  $\alpha_{1,0} = 5$  mm, similar to previous work [68], and a steady and/or oscillating current with a specified frequency and amplitude. We use a 0.25 s time step and simulation is halted if the interface touches the anode, which would be a case of short circuit of the Al cell, or after 1000 s have elapsed. When applying oscillating currents, we used a triangular shape (Fig. 3.11a) because it may be more economical to produce in real Al cells and because it eliminated the need for shorter time steps in simulations.

This chapter proceeds as follows: In §3.2 I discuss how we quantified the Al-electrolyte interface stability and the methods we used to analyze and delineate

the interface dynamics. In §3.3, I present simulation results showing the MPI present in the TRIMET 180 kA cell at 4 cm ACD with steady current, and use the methods described in §3.2 to show that the MPI is caused by the resonance of three specific  $G_{m,n}$  interface wave modes. Also, I explain how these three modes couple through the different components of the vertical magnetic field. In §3.4, I show that adding an oscillating current, with a particular frequency and amplitude, to the steady current can prevent the MPI by exciting standing waves. I present simulation results of the TRIMET Al cell having stable operation at 4 cm ACD and 3.8 cm ACD with the oscillating current present, and describe the interface behaviour and wave mode dynamics. Further, I show that an oscillating current can be used to halt the MPI. In §3.5, I summarize the results and discuss some limitations of the model, implications of the results, and potential future directions.

## 3.2 Characterizing Interface Oscillations

Since the MPI [33] manifests as a circulating travelling wave on the Al-electrolyte interface, characterizing the interface's motion is important in understanding the stability of the cell and the underlying dynamics. This characterization has to be done through quantifiable metrics so that different cases can be compared efficiently and adequately. Some of the questions we wanted to answer were: Is the interface motion stable? How stable/unstable is it? What can we say about the its temporal dynamics? and What interface wave modes  $G_{m,n}$  are present?

### 3.2.1 Quantifying Interface Stability

MHD-Valdis outputs the Al-electrolyte interface height  $z_{i,j}$  of element  $(i, j)$  at every time step, where  $1 \leq i \leq N_x$  and  $1 \leq j \leq N_y$ . Visualizing this 3 dimensional

data by creating a video of the interface's motion in time offered a good way of observing the overall motion. However, it didn't offer a quantifiable metric to assess its stability in an efficient manner. So, we thought about reducing the interface height  $z_{i,j}$  to single number, at every instant in time, that would capture how high the interface oscillations are. This can be done in many ways, but we opted to using the root-mean-square displacement of the interface from its mean shape in time:

$$z_{RMS} = \left( \frac{1}{N_x N_y} \sum_{i=1}^{N_x} \sum_{j=1}^{N_y} (\Delta z_{i,j})^2 \right)^{\frac{1}{2}} \quad (3.1)$$

where  $\Delta z_{i,j}$  is the interface displacement from its mean height in time,  $\overline{z_{i,j}}$ :

$$\Delta z_{i,j} = z_{i,j} - \overline{z_{i,j}} \quad (3.2)$$

When an instability is present,  $z_{RMS}$  will increase exponentially over time and its rate of increase would quantify how strong the instability is. I fit an exponential function to  $z_{RMS}$  of the form:

$$z_{RMS} \propto c_1 e^{c_2} \quad (3.3)$$

where  $c_1$  is a pre-factor, and  $c_2$  is the growth or decay rate. Comparing the values of  $c_2$  for different cases would show the relative stability between them.

### 3.2.2 Untangling Interface Mode Dynamics

Since the MPI is a parametric instability that depends on a coupled resonance between interface wave modes [39], we wanted to know which modes  $G_{m,n}$  of Eq. 1.43 are strongest. Since these wave modes form an orthonormal basis of the interface surface, we performed a linear least-squares projection of the interface displacement  $\Delta z_{i,j}$  onto the  $G_{m,n}$  modes using a procedure similar to the one described in [72]. The linear least-square projection is performed by determining

the wave mode amplitudes,  $\alpha_{m,n}$ , that minimize the squared error between the interface displacement and the estimated interface displacement:

$$\begin{aligned} z_{error}^2 &= \left( \Delta z - \sum_{m,n} \alpha_{m,n} G_{m,n} \right)^2 = (\Delta z - z_{est})^2 \\ &= (\Delta z)^2 - 2(\Delta z)z_{est} - z_{est}^2 \end{aligned} \quad (3.4)$$

The squared error Eq. 3.4 admits a minimum that satisfies:

$$\frac{\partial z_{error}^2}{\partial \alpha_{m,n}} = 0 \quad (3.5)$$

for all coefficients  $\alpha_{m,n}$ . Substituting Eq. 1.43 and Eq. 3.4 into Eq. 3.5 yields:

$$\begin{aligned} -2(\Delta z)G_{m,n} + 2 \sum_{m',n'} \alpha_{m',n'} G_{m',n'} G_{m,n} &= 0 \\ \implies \Delta z G_{m,n} &= \sum_{m',n'} \alpha_{m',n'} G_{m',n'} G_{m,n} \end{aligned} \quad (3.6)$$

We truncate Eq. 3.6 by considering the lowest-order modes up to a certain number,  $0 \leq m \leq M$  and  $0 \leq n \leq N$ . Let the mode matrix  $\mathbf{g}$  be defined as:

$$\begin{bmatrix} G_{0,0} \\ \vdots \\ G_{M,0} \\ \vdots \\ G_{M,N} \end{bmatrix} \quad (3.7)$$

where each mode  $G_{m,n}$  is  $N_x$  by  $N_y$  is size, making  $\mathbf{g}$  of size  $(M+1)(N+1)$  by  $N_x N_y$ . Also, let the coefficient vector  $\boldsymbol{\alpha}$  be defined similarly as:

$$\begin{bmatrix} \alpha_{0,0} \\ \vdots \\ \alpha_{M,0} \\ \vdots \\ \alpha_{M,N} \end{bmatrix} \quad (3.8)$$

Then, Eq. 3.6 truncated to the lowest-order modes can be written in matrix form as:

$$\mathbf{g}\Delta\mathbf{z} = \mathbf{M}\boldsymbol{\alpha} \quad (3.9)$$

where  $\Delta\mathbf{z}$  is the interface displacement vector that is  $N_x N_y$  by 1 and  $\mathbf{M} = \mathbf{g}\mathbf{g}^\top$  is the projection matrix. Thus, the coefficients of the best fit can be found as:

$$\boldsymbol{\alpha} = \mathbf{M}^{-1}\mathbf{g}\Delta\mathbf{z} \quad (3.10)$$

Since  $\mathbf{g}$  and  $\Delta\mathbf{z}$  are known, the main task is to invert  $\mathbf{M}$ . We do so by first finding the singular-value decomposition (SVD) [73] of  $\mathbf{M}$ ,

$$\mathbf{M} = \mathbf{U}\boldsymbol{\Sigma}\mathbf{V}^\top \quad (3.11)$$

where  $\mathbf{U}$  and  $\mathbf{V}$  are unitary matrices with orthonormal columns and  $\boldsymbol{\Sigma}$  is a matrix with real, nonnegative entries on the diagonal and zeros off the diagonal [73]. Using the SVD decomposition Eq. 3.11, we can find the left pseudo-inverse of  $\mathbf{M}$  [73–75] and find the coefficients using Eq. 3.10 as:

$$\boldsymbol{\alpha} = (\mathbf{V}\boldsymbol{\Sigma}^{-1}\mathbf{U}^\top)\mathbf{g}\Delta\mathbf{z} \quad (3.12)$$

We implemented the procedure described above using a custom MATLAB function to find the coefficients  $\alpha_{m,n}$  of the best linear least-squares estimate of the interface displacement,  $\Delta z$ , at every instant in time. I used the condition number, which is the ratio of the largest and smallest singular values of a matrix [73], to quantify how sensitive is inverting matrix  $\mathbf{M}$  to errors in the input.

Additionally, we calculated power spectra using the fast Fourier Transform (FFT) [73] to find the frequencies associated with the interface displacement  $\Delta z$ . We did not use  $z_{RMS}$ , but rather used a single point in one corner of the cell, without squaring its displacement, since the square of a function generally contains different frequencies than the original function.

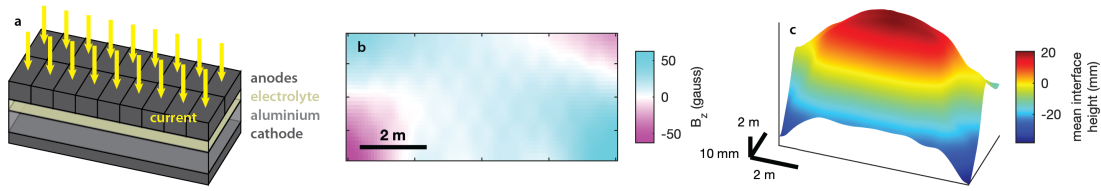


**Figure 3.2:** Characteristics of Al electrolysis cells. **a**, Electrical current flows downward from anodes to cathode, through electrolyte and Al layers. **b**, The vertical component of the ambient magnetic field, at the Al-electrolyte interface, from our simulations, seen from above. The field varies spatially and is caused primarily by currents in the adjacent cells and nearby busbars. **c**, The Al-electrolyte interface bulges because of electromagnetic forces due to the magnetic field and the current.

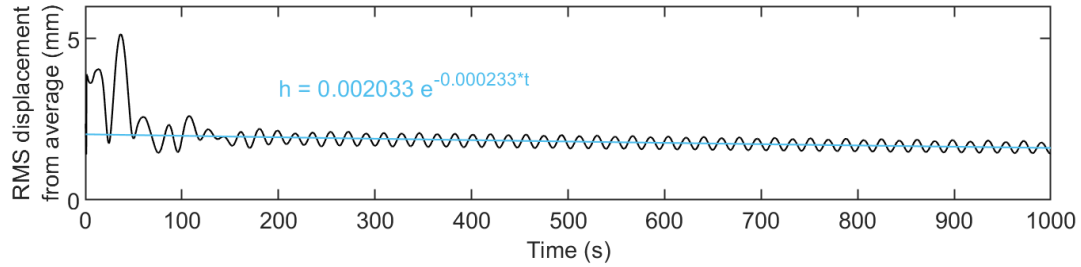


**Figure 3.3:** Root-mean-square displacement of the Al-electrolyte interface at 4.3 cm ACD. An exponential fit is shown in blue for  $t > 100$  s. The RMS displacement decays very slowly in time.

### 3.3 Simulating MPI in a TRIMET 180 kA Al Electrolysis Cell

The first thing we set out to do in the simulations was to determine the critical ACD of the TRIMET cell; the minimum electrolyte thickness at which the cell is still stable. Critical stability is quantified by the interface displacement not growing or decaying in time. We found the critical ACD to be about 4.3 cm when rounded up to the nearest mm. The ambient vertical magnetic field field is shown in Fig. 3.2b, and The Al-electrolyte interface developed a central bulge (Fig. 3.2c) as expected [76].  $z_{RMS}$  at 4.3 cm ACD is shown in Fig. 3.3 and it is decaying in

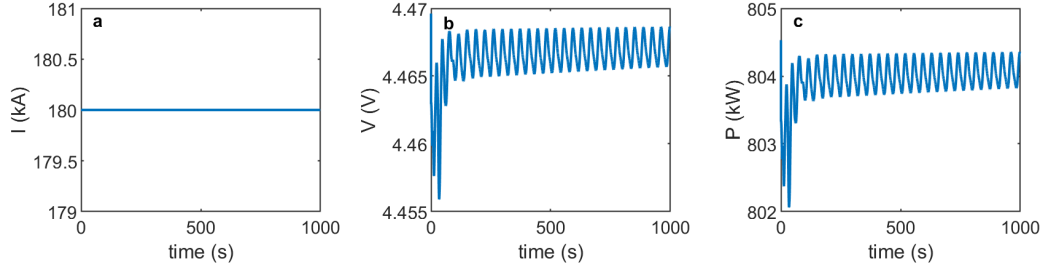


**Figure 3.4:** Current, voltage, and total power for the TRIMET Al cell at 4.3 cm ACD with steady current. **a**, Current supplied is constant at 180 kA. **b**, Cell voltage exhibits a low-frequency oscillation from the waves on the Al-electrolyte interface. The average voltage is 4.467 V. **c**, Total cell power. Average total power is 804.8 kW.

time but very slowly. This is because the critical ACD is slightly below 4.3 cm. Our result agrees with the previous work [68], where the TRIMET 180 kA cell was shown to be stable at 4.5 cm ACD. The supplied current, instantaneous cell voltage, and instantaneous total cell power are plotted in Fig. 3.4, with the average cell voltage at 4.47 V and average total cell power at 804.8 kW. The instantaneous total power of the Al cell is calculated by multiplying the instantaneous cell voltage with the supplied current.

### 3.3.1 MPI in Simulation

We lowered the ACD by 3 mm from its critical value to 4 cm, kept the current steady at 180 kA (Fig. 3.5a) and ran the simulation again. As we expected, lowering the ACD triggered the MPI and the interface height grew until it touched the anode and a short circuit happened at  $t \approx 800$  s. The cell voltage and total power showed a sudden drop at that time as shown in Fig. 3.5b-c. I plotted the RMS displacement of the interface,  $z_{RMS}$ , in Fig. 3.6a where low frequency oscillations and exponential growth are evident. The growth rate was about  $2.2 \times 10^{-3} \text{ s}^{-1}$  as shown by the exponential fit in blue in Fig. 3.6a.

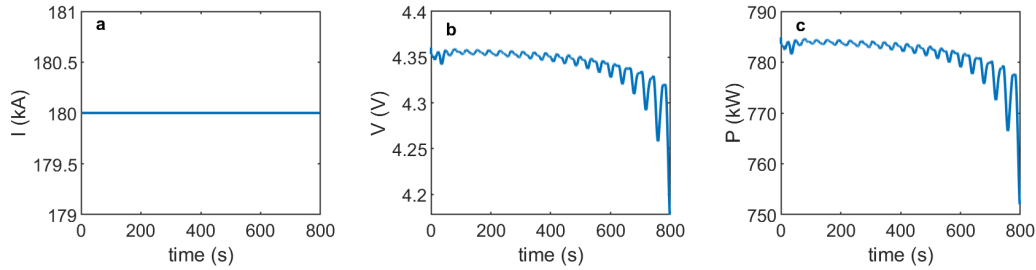


**Figure 3.5:** Current, voltage, and total power for the TRIMET Al cell at 4 cm ACD with steady current. **a**, Current supplied is constant at 180 kA. **b**, Cell voltage exhibits a low-frequency oscillation from the waves on the Al-electrolyte interface. The average voltage is 4.34 V, and the sudden voltage drop at the end is due to the short circuit happening when the Al layer touched the anode. **c**, Total cell power. The sudden drop in power at the end is due to the short circuit. The average total power is 781.6 kW.

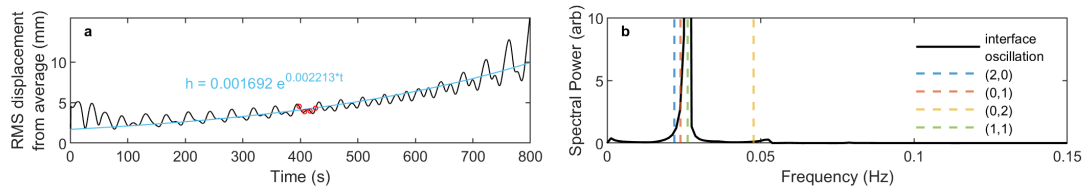


**Figure 3.6:** The metal pad instability (MPI) in a simulated Al electrolysis cell. **a**, Displacement of the Al-electrolyte interface grows exponentially, as shown by the fitted curve. **b**, The spectral power of the displacement of one point on the interface is dominated by a narrow frequency band, close to the frequency of interface wave modes  $G_{2,0}$ ,  $G_{0,1}$ , and  $G_{1,1}$ , expected in the MPI.

To analyze the interface oscillations, I calculated the power spectrum of the interface displacement at a point, see §3.2, which showed that its power is highly concentrated near 0.0263 Hz (Fig. 3.6b). This frequency lies close to the frequencies  $f_{2,0}$ ,  $f_{0,1}$ , and  $f_{1,1}$  from Eq. 1.44 of the wave modes  $G_{2,0}$ ,  $G_{0,1}$  and  $G_{1,1}$ . Thus, I had a suspicion that the MPI is a result of the resonant coupling of these modes. To verify the role of these three modes, I performed a linear least-squares projection of the simulated interface displacement shape onto a basis set of wave modes  $G_{m,n}$ , see §3.2. An example is shown in Fig. 3.7 where the interface displacement at  $t = 125$  s is plotted in Fig. 3.7a and the estimated displacement through the wave mode projection is plotted in Fig. 3.7b. Visually, the actual interface displacement and estimated interface displacement look the same. I calculated the % error of the displacement estimation, defined as:

$$\frac{\sum_{i=1}^{N_x} \sum_{j=1}^{N_y} |z_{error}|}{\sum_{i=1}^{N_x} \sum_{j=1}^{N_y} |\Delta z|} \times 100 \quad (3.13)$$

at every instant in time and plotted the result in Fig. 3.7c. The % error is low and  $< 4$  % through the duration of the simulation. For this projection procedure, we retained the 128 lowest-order modes  $0 \leq m \leq 16$  and  $0 \leq n \leq 8$ . Spectral power in modes with  $m > 6$  or  $n > 6$  was always negligible. The projection was also robust with the condition number low ( $\sim 4$ ). The wave mode amplitudes  $\alpha_{m,n}$  vary over time; one way to quantify their typical overall magnitude is with the root-mean-square amplitude  $\langle \alpha_{m,n}^2 \rangle^{\frac{1}{2}}$ , where brackets signify averaging over time. I calculated the RMS amplitude each mode, through the duration of the simulation, and plotted the results in Fig. 3.8a. Clearly the  $G_{2,0}$ ,  $G_{0,1}$ , and  $G_{1,1}$  are far stronger than all other modes as expected from the power spectrum Fig. 3.6b. Plotting their amplitudes ( $\alpha_{2,0}$ ,  $\alpha_{0,1}$ , and  $\alpha_{1,1}$ ) as a function of time shows that they are growing exponentially and oscillate a single frequency near 0.0263 Hz (Figs. 3.8b-c). Note that the amplitude of other modes is not growing in time, such as  $\alpha_{0,2}$  of  $G_{0,2}$ , which is also plotted in Figs. 3.8b-c. The coupling of these

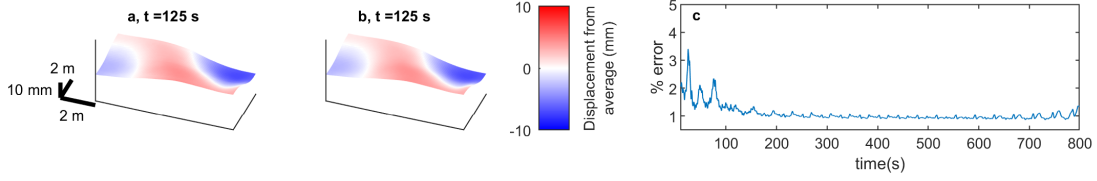


**Figure 3.7:** Example of estimating the interface displacement through projecting onto the modes  $G_{m,n}$ . **a**, Al-electrolyte interface displacement at  $t=125$  s. **b**, Estimate of the interface displacement at  $t=125$  s through performing a linear least-square projection onto the interface modes  $G_{m,n}$ . The estimated interface displacement looks visually the same as the actual interface displacement. **c**, The % error of the interface displacement estimate relative to the actual interface displacement. The error is very low and  $< 4\%$  at all times.

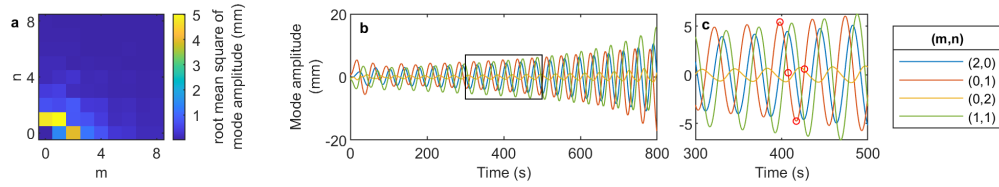


**Figure 3.8:** The modes of the MPI in a simulated Al electrolysis cell. **a**,  $G_{2,0}$ ,  $G_{0,1}$ , and  $G_{1,1}$  have greater root-mean-square amplitude than any other modes. **b**,  $G_{2,0}$ ,  $G_{0,1}$ , and  $G_{1,1}$  oscillate with a common frequency and grow over time.  $G_{0,2}$  oscillates with the same frequency but does not grow in time. **c**,  $G_{2,0}$  and  $G_{0,1}$  are separated in phase by  $\sim 90^\circ$ , characteristic of a traveling wave as in the MPI.

three modes was suggested to cause the MPI by Urata in [6].

### 3.3.2 MPI Mode Couplings

To explain the different mode couplings, we express the vertical magnetic field  $B_z$  (Fig. 3.2b) as a Taylor series

$$B_z = B_{0z} + B_{xz}x + B_{yz}y, \quad (3.14)$$

where  $B_{0z}$  is the uniform component,  $B_{xz}$  quantifies linear variation in the  $x$  direction,  $B_{yz}$  quantifies linear variation in the  $y$  direction, and higher-order terms have been neglected. In commercial potlines  $B_{0z}$  is generated primarily by the

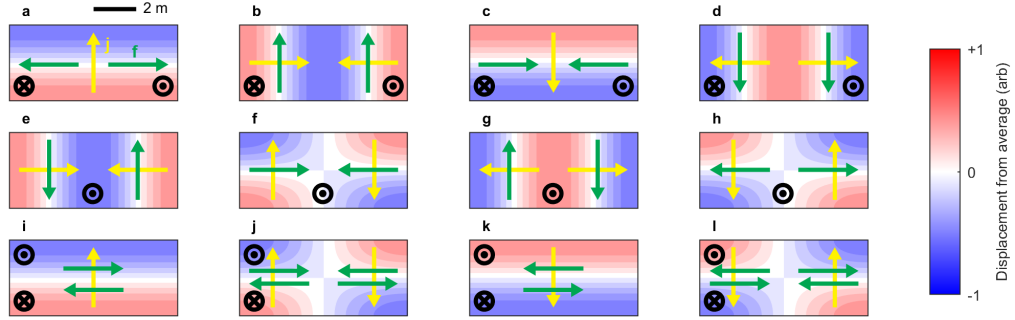


**Figure 3.9:** Coupling of different mode pairs through the magnetic field components. **a-d** Coupling between  $G_{0,1}$  and  $G_{2,0}$  interface modes through the x-gradient component  $B_{xz}$  of the vertical magnetic field  $B_z$ . The modes are viewed from above, with the horizontal displacement current density  $j$  and resulting electromagnetic forces  $f$  sketched. **e-h** Coupling between  $G_{2,0}$  and  $G_{1,1}$  interface modes through the constant component  $B_{0z}$  of  $B_z$ . **i-l** Coupling between  $G_{0,1}$  and  $G_{1,1}$  interface modes through the y-gradient component  $B_{zy}$  of  $B_z$ .

current in the adjacent line,  $B_{xz}$  is generated primarily by the current in the side risers and busbar under the cell, and  $B_{xy}$  is generated primarily by current in the anode risers or cathode busbar [6]. When a wave is present on the Al-electrolyte interface, current flows preferentially where the electrolyte is thinner (at interface crests), due to the low electrical conductivity of the electrolyte (Table 3.1). Then it “shorts” through the Al layer, due to its high electrical conductivity compared to the carbon cathode (Table 3.1), and spreads horizontally after entering the Al layer [8, 50]. That spreading creates a horizontal compensation current,  $j$ , in the Al pointing from a crest to a trough, which interacts with the different components of  $B_z$  to create horizontal electromagnetic forces,  $f$ , that couple different modes [6, 8, 29]. For example, the  $G_{0,1}$  mode causes a horizontal current  $j$  that interacts with  $B_{xz}$  to produce a force  $f$  that excites the  $G_{2,0}$  mode (Fig. 3.9a). It, in turn, excites the  $G_{0,1}$  mode, resulting in a feedback loop (Fig. 3.9b-d). Similarly,  $B_{0z}$  couples the  $G_{2,0}$  and  $G_{1,1}$  modes (Fig. 3.9e-h), and  $B_{zy}$  couples the  $G_{0,1}$  and  $G_{1,1}$  modes (Fig. 3.9i-l).

Visualizing the interface displacement shape at four times spaced evenly through a 0.0263-Hz oscillation cycle (marked with red dots in Fig. 3.6a and Fig. 3.8c) reveals canonical MPI dynamics: a traveling wave that circulates counter-clockwise when viewed from above (Figs. 3.10a-d), consistent with the fact that  $G_{2,0}$  and  $G_{0,1}$  vary with  $\sim 90^\circ$  phase difference. To understand the underlying MPI mechanism, a simplified representation is helpful, so we first found which wave modes are present at each instant (Figs. 3.10e-h) by calculating the mode's amplitude as a percentage of the total energy of all modes. Here, we quantified the total energy of all modes by the sum of all modes' amplitudes in absolute value. The sign of the mode amplitude was preserved to indicate the mode orientation. Then, we reconstructed the interface displacement shape after eliminating all but the two strongest modes at each instant (Figs. 3.10i-l). With the aid of the coupling mechanisms presented in Fig. 3.9, we can see the interplay among  $G_{0,1}$ ,  $G_{2,0}$ , and  $G_{1,1}$ ; the most dominant modes present (Fig. 3.8a). At  $t = 398$  s,  $G_{0,1}$  and  $-G_{1,1}$  are present and excite  $G_{2,0}$  and  $G_{1,1}$ , which have appeared by  $t = 407.5$  s. Those modes, in turn, excite  $-G_{0,1}$  and  $G_{1,1}$ , which have appeared by  $t = 417$  s. Those modes, in turn, excite  $-G_{2,0}$  and  $-G_{1,1}$ , which have appeared by  $t = 426.5$  s. Finally, they excite the original modes,  $G_{0,1}$  and  $-G_{1,1}$ . The coupling and timing of the three modes are right for forming a closed cycle that amplifies the circulating wave.

### 3.4 Stabilization Using an Oscillating Current

Knowing that the MPI is present at 4 cm ACD with steady current, it was time to test our hypothesis of whether adding an oscillation to the current would prevent the MPI and stabilize the Al cell. To test, we ran a new simulation, identical to the one that produced the MPI, except that the steady 180 kA current was supplemented with an oscillating component of half-amplitude 19.8 kA and frequency

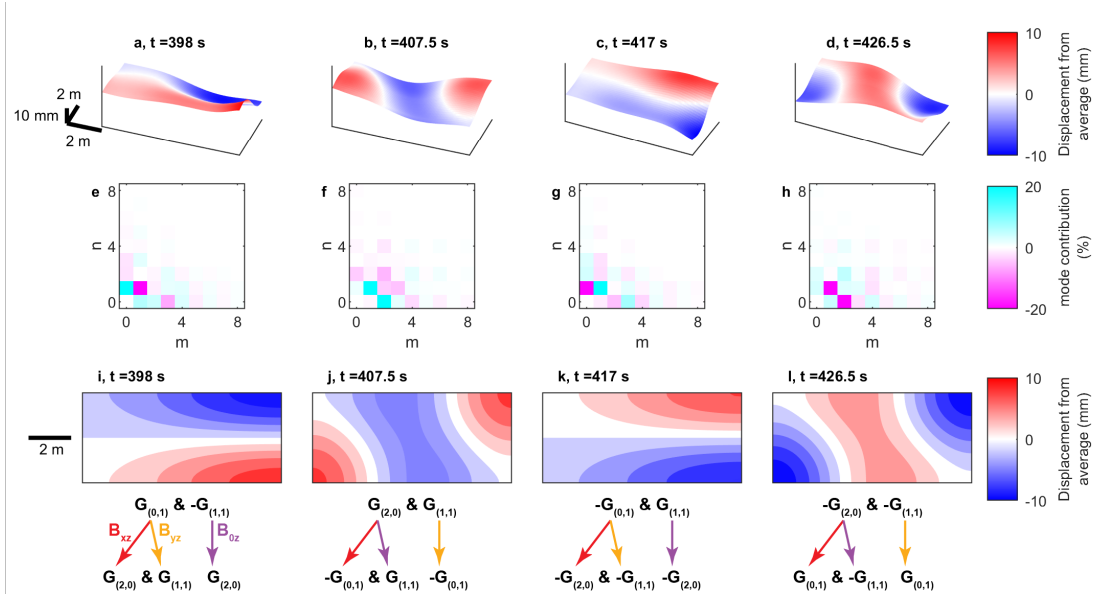


**Figure 3.10:** Mode coupling creating the MPI. **a-d**, Interface displacements at four times spanning one MPI cycle (red dots in Fig. 3.8c) show a circulating traveling wave. **e-h**, Modal decomposition of the interface displacements at the same times as in (a-d). Two dominant modes are present at each time, and an interplay among  $G_{2,0}$ ,  $G_{0,1}$ , and  $G_{1,1}$  is evident in creating the MPI. **i-l**, Reconstruction of the interface displacements at the same times as in (a-d) using only the two most dominant modes present in each of (e-h), viewed from above.  $G_{0,1}$  and  $-G_{1,1}$  are present in (i) and excite  $G_{2,0}$  and  $G_{1,1}$  through the different components of  $B_z$  based on Fig. 3.9.  $G_{2,0}$  and  $G_{1,1}$  consequently excite  $-G_{0,1}$  and  $G_{1,1}$  and so on.

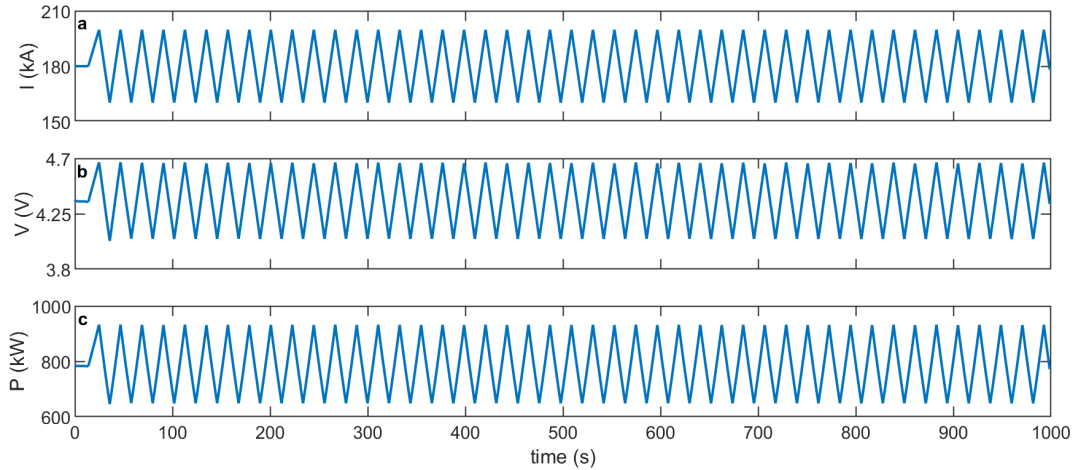


**Figure 3.11:** Current, voltage, and total power for the TRIMET Al cell at 4 cm ACD with an oscillating current of half-amplitude 19.8 kA and frequency 0.045 Hz **a**, Current supplied has an oscillating triangular component with an average of 180 kA. **b**, Cell voltage exhibits a low-frequency oscillation at the current driving frequency. The average voltage is 4.36 V. **c**, Total cell power. Average total power is 787.1 kW.

0.045 Hz as shown in Fig. 3.11a. I plotted the RMS displacement in Fig. 3.12a, and as shown it oscillates but did not grow exponentially – the MPI was absent. The spectral power of the displacement at a point showed strong peaks at two frequencies, one near  $f_{2,0}$ ,  $f_{0,1}$ , and  $f_{1,1}$ , as seen in the presence of the MPI, and another near the 0.045 Hz, the drive frequency of the current (Fig. 3.12b).

To investigate the modal dynamics, I projected the interface displacement shape into  $G_{m,n}$  wave modes. An example is shown in Figs. 3.13a-b where the interface displacement and estimated interface displacement are plotted at  $t = 125$  s, respectively. The condition number was low again ( $\sim 4$ ), and the % error was  $\leq 3\%$  at all times (Fig. 3.13c). I plotted the RMS amplitude of each mode in Fig. 3.13d and found that in addition to  $G_{2,0}$ ,  $G_{0,1}$ , and  $G_{1,1}$  modes associated with the MPI, the  $G_{0,2}$  and  $G_{4,0}$  were also present and strongest. Their corresponding frequencies,  $f_{0,2}$  and  $f_{4,0}$ , nearly match the drive frequency (Fig. 3.12b), and the temporal variations of their amplitudes,  $\alpha_{0,2}$  and  $\alpha_{4,0}$ , are nearly sinusoidal

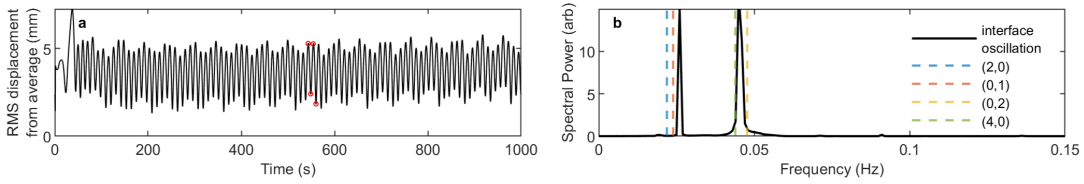


**Figure 3.12:** Characteristics of the interface displacement oscillations with an oscillating current of frequency 0.045 Hz and half-amplitude 19.8 kA. **a**, RMS interface displacement. The Al-electrolyte interface oscillates stably, not growing or decaying in time. **b**, The spectral power of the displacement of one point on the interface is dominated by one frequency band close to the expected in the MPI frequency, and another close to the drive frequency.

(Figs. 3.13e-f) oscillating at the drive frequency, unlike those of  $G_{2,0}$  and  $G_{0,1}$ , which are more complicated. Visualizing the interface shape at four times spaced evenly through a 0.045-Hz oscillation cycle (marked with red dots in Fig. 3.12a and Fig. 3.13f) reveals not a traveling wave, as would occur with the MPI, but a standing wave (Figs. 3.14a-d), consistent with the fact that  $G_{0,2}$  and  $G_{4,0}$  vary synchronously and with almost no phase difference (Fig. 3.13f). Taken together, these facts suggest that a standing gravity wave, driven by the current oscillation, frustrates the circulating wave that comprises the MPI.

For a simplified explanation of the mechanism, we reconstructed the interface shape after eliminating all modes except  $G_{0,2}$  and  $G_{4,0}$ , which account for most of the power and can approximate the actual shape well (Figs. 3.14e-h). Remembering that current in the Al spreads horizontally from interface crests, we see that the resulting electromagnetic forces tend to drive two vortex-like circulations, one in each half of the cell, whose vorticities alternate over time but are always opposed: one clockwise and one counter-clockwise. Though counter-clockwise flow might tend to facilitate the counter-clockwise MPI circulation (even if not near the cell center), clockwise flow strongly opposes the MPI and is apparently sufficient, in this case, to prevent it altogether. These observations suggest a novel strategy for stabilizing Al cells [12]: oscillate the current at a frequency chosen to excite

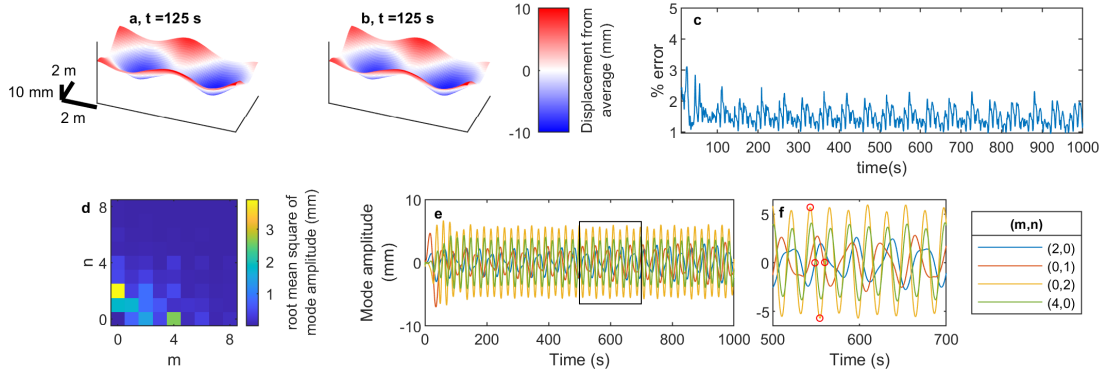


**Figure 3.13:** Oscillating current excites standing waves. **a**, The Al-electrolyte interface displacement at  $t = 125$  s. **b**, Reconstruction of the interface displacement through performing a projection onto the interface modes at  $t = 125$  s. The estimated interface displacement looks visually the same as the actual interface displacement. **c**, The % error of the interface displacement estimate relative to the actual interface displacement. The error is very low and  $\leq 3\%$  at all times. **d**,  $G_{2,0}$ ,  $G_{0,1}$ ,  $G_{1,1}$ ,  $G_{0,2}$ , and  $G_{4,0}$  have greater root-mean-square amplitude than any other modes. **e-f**, Their amplitudes  $\alpha_{m,n}$  oscillate, and  $G_{0,2}$  and  $G_{4,0}$  are almost aligned in phase, characteristic of a standing wave.

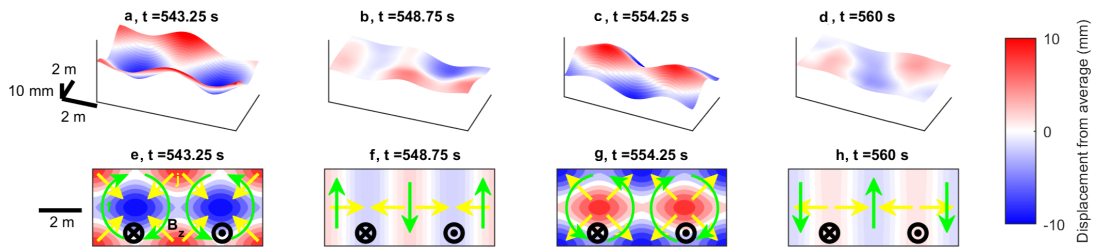


**Figure 3.14:** Standing waves frustrate the MPI. **a-d**, Interface displacements at four times spanning one drive cycle show a standing wave. **e-h**, Interface displacements at the same times as in (a-d), estimated using only  $G_{0,2}$  and  $G_{4,0}$  and viewed from above. The resulting electromagnetic forces **f** (sketched) often favour clockwise circulation, opposing and frustrating the MPI.

standing wave modes, which frustrate the MPI traveling wave.

### 3.4.1 Preventing the MPI at 3.8 cm ACD

By applying the oscillating current of half-amplitude 19.8 kA and frequency 0.045 Hz we were able to prevent the MPI and maintain cell stability at 4 cm ACD; a 7% reduction from the ACD required for critical stability with a steady current only. This resulted in average cell voltage decreasing by  $\approx 2.5\%$  (Fig. 3.11b vs Fig. 3.4b) and average total cell power by 2.2% (Fig. 3.11c vs Fig. 3.4c). We wanted to see if we can reduce the ACD even further while maintaining cell stability, so we ran another simulation at 3.8 cm ACD with an oscillating current of half-amplitude 19.8 kA and frequency 0.045 Hz. The results are summarized in Fig. 3.15, and the interface behaviour and dynamics are very similar to that at 4 cm ACD. The RMS interface displacement oscillates but does not grow exponentially indicating stability (Fig. 3.15a), however, it has a higher amplitude than before in Fig. 3.12a. This makes sense since lowering the ACD makes the cell more unstable [28]. Similar to before in Fig. 3.12b, the spectral power of the displacement at a point showed strong peaks at two frequencies, one near  $f_{2,0}$ ,  $f_{0,1}$ , and  $f_{1,1}$ , and another near the 0.045 Hz drive frequency (Fig. 3.15b). Decomposing the interface displacement shape into  $G_{m,n}$  modes, we found that the  $G_{2,0}$ ,  $G_{0,1}$ , and  $G_{1,1}$ ,  $G_{0,2}$  and  $G_{4,0}$  are strongest (Fig. 3.15c). A notable difference is that the MPI modes ( $G_{0,1}$ ,  $G_{2,0}$ , and  $G_{1,1}$ ) are stronger than before (Fig. 3.15c vs Fig. 3.13d). The temporal variations of the mode amplitudes  $\alpha_{m,n}$  are nearly sinusoidal (Figs. 3.15d-e) and the interface displacement dynamics (Figs. 3.15f-m) are similar to those discussed before (Figs. 3.14a-h). Thus, we demonstrated that the MPI can be prevented at 3.8 cm ACD, an 11.6% reduction from the critical value with steady current, reducing the total average power by  $\sim 4\%$  (Fig. 3.16c).

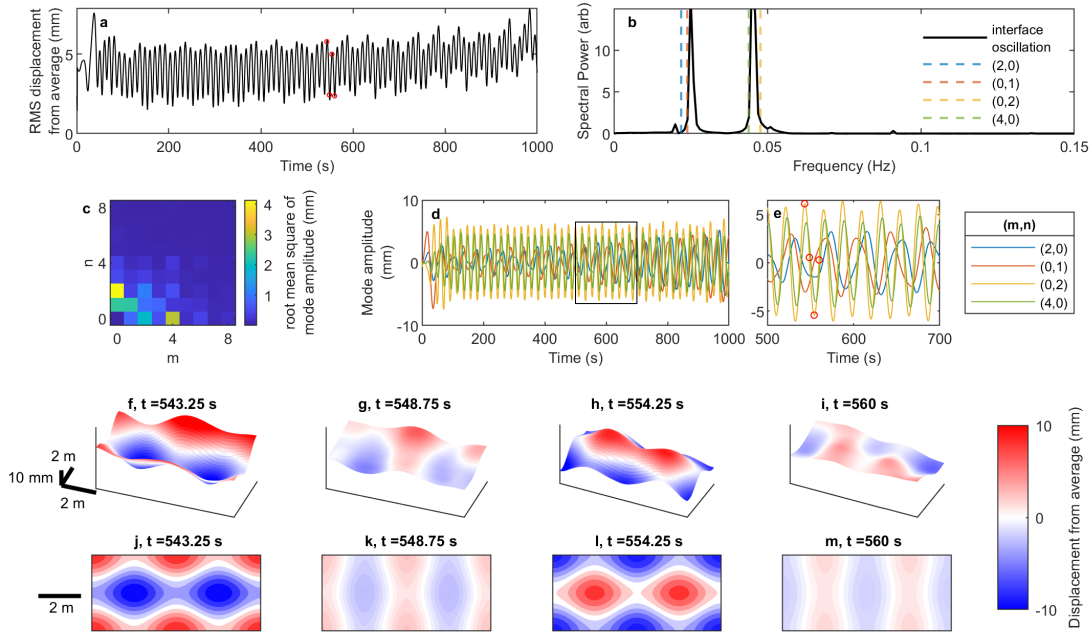


**Figure 3.15:** An oscillating current component prevents the MPI at 3.8 cm ACD. **a**, The Al-electrolyte interface oscillates stably. **b**, The spectral power of the displacement of one point on the interface is dominated by one frequency band close to the expected in the MPI frequency, and another close to the drive frequency. **c**,  $G_{2,0}$ ,  $G_{0,1}$ ,  $G_{1,1}$ ,  $G_{0,2}$ , and  $G_{4,0}$  have greater root-mean-square amplitude than any other modes. **d-e**, Their amplitudes  $\alpha_{m,n}$  oscillate, and  $G_{0,2}$  and  $G_{4,0}$  are almost aligned in phase, characteristic of a standing wave. **f-i**, Interface displacements at four times spanning one drive cycle (red dots in (e)) show a standing wave. **j-m**, Interface displacements at the same times as in (f-i), estimated using only  $G_{0,2}$  and  $G_{4,0}$  and viewed from above.

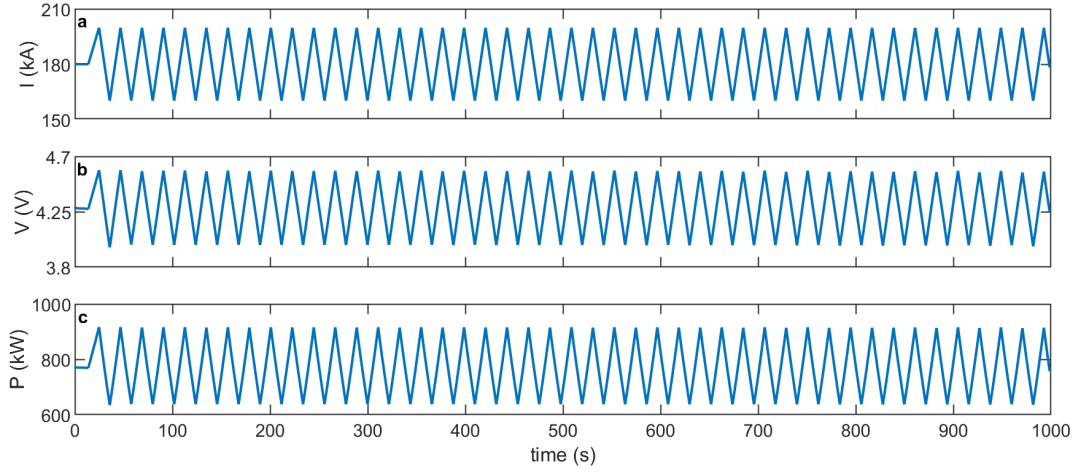


**Figure 3.16:** Current, cell voltage, and power for the TRIMET Al cell at 3.8 cm ACD with an oscillating current of half-amplitude 19.8 kA and frequency 0.045 Hz **a**, Current supplied has an oscillating triangular component with an average of 180 kA. **b**, Cell voltage exhibits a low-frequency oscillation at the current driving frequency. The average voltage is 4.28 V. **c**, Cell total power. Average power is 773.4 kW.

### 3.4.2 Exciting a Different Standing Wave

We prevented the MPI successfully by applying the oscillating current of half-amplitude 19.8 kA and frequency 0.045 Hz. Oscillating the current at this frequency excited a standing wave composed of the  $G_{0,2}$  and  $G_{4,0}$ , whose frequencies,  $f_{0,2}$  and  $f_{4,0}$ , nearly match the drive frequency of 0.045 Hz. In addition to the standing wave composed of the  $G_{0,2}$  and  $G_{4,0}$  modes, we reasoned, other standing wave modes, composed of other  $G_{m,n}$  pairs with approximately matched  $f_{m,n}$ , should also work. To test, we ran another simulation at 4 cm ACD with the steady 180 kA current supplemented with an oscillating component of half-amplitude 19.8 kA and frequency 0.069 Hz, near the  $f_{6,0}$ . A summary of the results is in Fig. 3.17. The RMS interface displacement exhibits low-frequency oscillations that are stable and decay slowly in time (Fig. 3.17a). By applying an exponential fit (not shown), I found the decay rate to be  $1.9 \times 10^{-4} \text{ s}^{-1}$ . The power spectrum of a point on the interface displacement, Fig. 3.17b, shows two narrow peaks, one

near the MPI frequency of 0.0263 Hz and another near the oscillating current frequency of 0.069 Hz. Projecting the interface displacement onto the  $G_{m,n}$  wave modes, I found that other than the MPI modes,  $G_{2,0}$ ,  $G_{0,1}$ , and  $G_{1,1}$ , the  $G_{0,2}$  and  $G_{6,0}$  are also strong, with the  $G_{0,2}$  being the strongest (Figs. 3.17c-e). Visualizing the interface shape at four times spaced evenly through a 0.069-Hz oscillation cycle (marked with red dots in Fig. 3.17a and Fig. 3.17e) reveals a standing wave (Figs. 3.17f-m), and one different from before (Figs. 3.15f-m). For the interface displacement mode projection procedure, the condition number was 4 and the % error was  $\leq 4\%$  at all times.

### 3.4.3 Halting the MPI

Having prevented the MPI, we wondered if we could also halt it in progress. To find out, we ran a simulation at 4 cm ACD with holding the current steady at 180 kA for 100 s before adding a 19.8 kA oscillation at 0.045 Hz (Fig. 3.18a). As expected, the RMS displacement grew when the current was steady but stopped growing soon after we applied the current oscillation (Fig. 3.18b). As shown by the exponential fits, the RMS interface displacement was growing at a rate of  $1.8 \times 10^{-3}$  for the first 400 s and then decayed very slowly at a rate of  $4.3 \times 10^{-5}$  afterwards. The interface moved with characteristics of the MPI when the current was steady, but with characteristics of standing waves after we applied the current oscillation (Figs. 3.18c-j). The MPI was apparently halted.

I Looked at the power spectrum of the interface displacement at a point, plotted in Fig. 3.19a, and found that the interface oscillations are complex with many frequencies present. The power is concentrated in two narrow regions, with the main peak near the MPI frequency at 0.025 Hz and another peak near the current frequency at 0.045 Hz. Three additional smaller peaks are also present: one at 0.021 Hz near the first main peak, one at 0.049 Hz near the second main peak, and one near the frequency sum of the two main peak at 0.07 Hz. Then, I

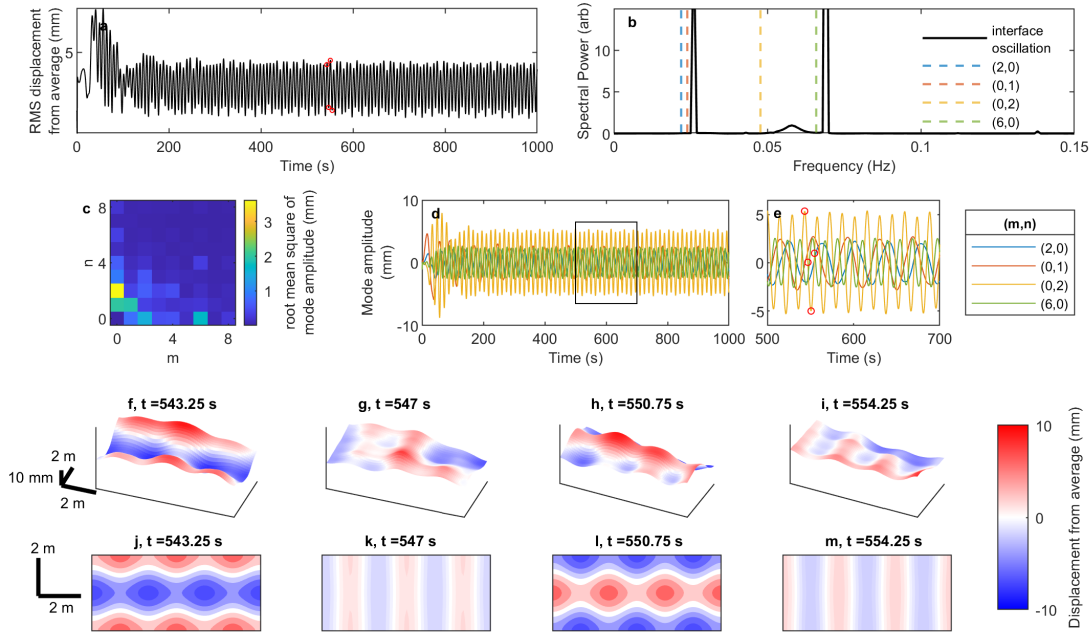


**Figure 3.17:** An oscillating current component with frequency 0.069 Hz prevents the MPI. **a**, The Al-electrolyte interface oscillates stably. **b**, The spectral power of the displacement of one point on the interface is dominated by one frequency band close to the expected in the MPI frequency, and another close to the drive frequency. **c**,  $G_{2,0}$ ,  $G_{0,1}$ ,  $G_{1,1}$ ,  $G_{0,2}$ , and  $G_{6,0}$  have greater root-mean-square amplitude than any other modes. **d-e**, Their amplitudes  $\alpha_{m,n}$  oscillate, and  $G_{0,2}$  and  $G_{6,0}$  are almost aligned in phase, characteristic of a standing wave. **f-i**, Interface displacements at four times spanning one drive cycle (red dots in (e)) show a standing wave. **j-m**, Interface displacements at the same times as in (f-i), estimated using only  $G_{0,2}$  and  $G_{6,0}$  and viewed from above.

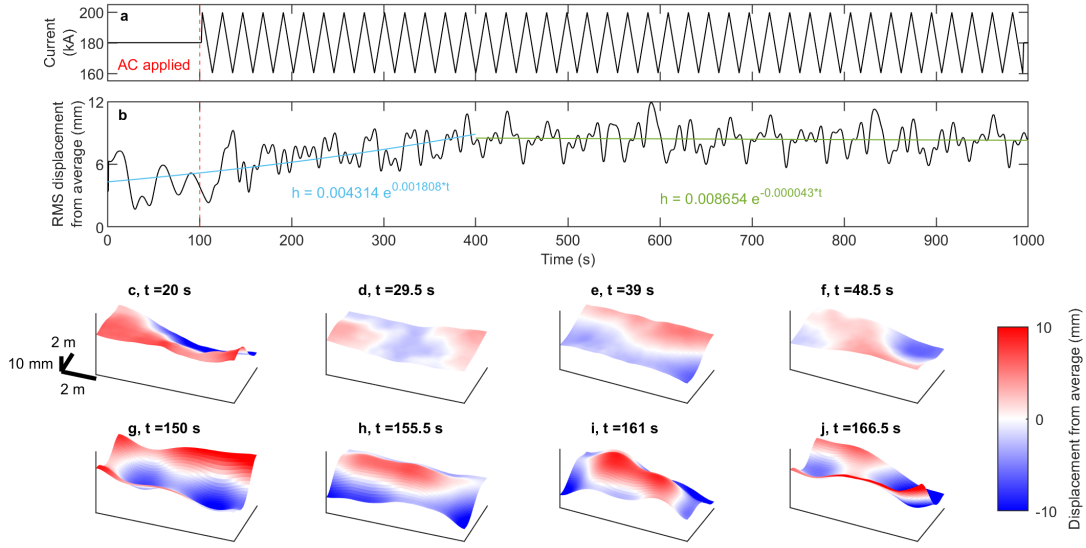


**Figure 3.18:** An oscillating current component halts the MPI in progress. **a**, The applied current was steady for the first 100 s, before an oscillatory current with half-amplitude 19.8 kA and frequency 0.045 Hz was added. **b**, Interface displacement grew when the current was steady but stopped growing soon after we added current oscillation, indicating stability. **c-f**, Interface displacements, when current was steady, at four times spanning one MPI cycle. A circulating travelling wave is present. **g-j**, Interface displacements, after we added the oscillating current, at four times spanning one drive cycle. A standing wave is present.

projected the interface displacement onto the wave modes. The condition number was 4 and the % error was  $\leq 3\%$  at all times (Fig. 3.19b). The RMS mode amplitudes, Fig. 3.19c show that the MPI modes,  $G_{0,1}$ ,  $G_{1,1}$ ,  $G_{2,0}$ , are strongest followed by the modes we expected to excite by the 0.045 Hz current oscillation,  $G_{0,2}$  and  $G_{4,0}$ , which compose the standing wave. Additionally, other modes have non-negligible RMS amplitude such as  $G_{1,0}$ ,  $G_{2,1}$ , and  $G_{1,2}$ . The mode amplitudes  $\alpha_{2,0}$ ,  $\alpha_{0,1}$ , and  $\alpha_{0,2}$  (Figs. 3.19d-e), oscillate in time but not at a single frequency like before. These observations suggest that the MPI can be halted by adding an oscillating current. However, the interface dynamics are much more complex than they would be if the oscillating current is applied initially.

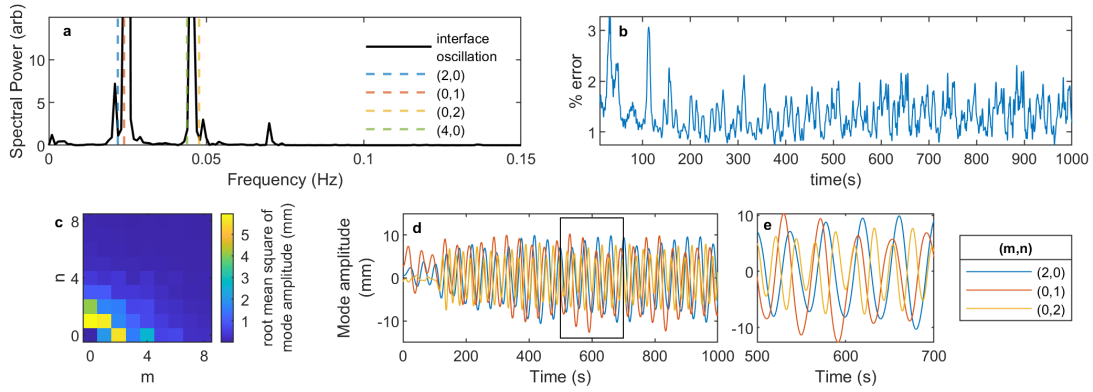


**Figure 3.19:** Wave modes when a non-initial current oscillation is applied. **a**, The spectral power of the displacement of one point on the interface shows many frequencies present, the dominant ones at the MPI frequency and current oscillation frequency. **b**, The estimated interface displacement using the wave mode projection had an error  $\leq 3\%$  at all times. **c**, RMS mode amplitude.  $G_{2,0}$ ,  $G_{0,1}$ , and  $G_{1,1}$  are strongest, followed by  $G_{0,2}$  and  $G_{4,0}$  **g-j**, Amplitudes of the  $G_{2,0}$ ,  $G_{0,1}$ , and  $G_{0,2}$  wave modes in time.

### 3.5 Summary and Future Work

In this chapter, I presented a series of simulation results of the TRIMET 180 kA Al reduction cells that show a novel strategy for stabilizing Al electrolysis cells: applying an oscillating current at a frequency chosen to excite standing wave modes. Through the RMS interface displacement, I showed that the critical ACD of the TRIMET cell is around 4.3 cm, and that at 4 cm ACD the MPI is present causing the cell to short. Through looking at the power spectra of the interface displacement at a point and projecting the interface displacement onto the set of wave modes  $G_{m,n}$ , I showed that the MPI in the TRIMET cell is a resonance between the  $G_{0,1}$ ,  $G_{1,1}$ , and  $G_{2,0}$  wave modes and explained how these three modes couple using different components of the vertical magnetic field. Adding an oscillating current, with half-amplitude 19.8 kA and frequency 0.045 Hz, stabilizes the same cell allowing for stable operation at 4 cm and 3.8 cm ACD. I showed that this oscillating current is exciting a standing wave composed of the wave modes  $G_{0,2}$

and  $G_{4,0}$  which frustrates the MPI. The excited wave modes have frequencies close to the current oscillation frequency. Stable operation at 4 cm was also achieved by exciting the  $G_{6,0}$  and  $G_{0,2}$  modes with the current oscillating at 0.069 Hz. Further, I showed applying the oscillating current after 100 s stabilized the TRIMET cell at 4 cm ACD and halted the MPI.

Achieving an 11.6% ACD decrease, from 4.3 cm with steady current to 3.8 cm with an oscillating current, resulted in reducing the average total power consumption by 4%. If applied to all Al electrolysis cells, this method could reduce the energy intensity of production by 2.1 MJ/kg Al, bringing annual savings of 34 TWh of electricity, perhaps \$1B in energy costs, and 13 Mt of CO<sub>2</sub>e emissions [9].

Other cell designs differ in, e.g., bus bar configuration (affecting  $B_z$ ) [77–79], size (affecting  $f_{m,n}$ ), and aspect ratio (affecting which modes couple, in the MPI and in standing waves). Still, standing waves composed of low-order modes can be excited in any design by oscillating the current at a frequency determined using Eq. 1.44, and those standing waves will impose clockwise forces that oppose the MPI much of the time; our novel stabilisation strategy is broadly applicable. For a given design, many standing wave modes are possible, but we speculate that lowest-frequency mode will be strongest for a given oscillation amplitude, because viscous damping is weaker for low-frequency modes [80]. Thus, we hypothesize that low-frequency modes frustrate the MPI with minimal oscillation amplitude; we hope to test that hypothesis in future work. Other designs have been more carefully optimized, allowing stable operation with steady currents and ACD <3 cm [81]. Still, decreasing ACD in any design could enable producing aluminum with less energy, lower cost, and lower emissions. We hope to test our strategy in an industrial-scale Al cell soon. Given that the MPI is likely to occur in liquid metal batteries (a grid-scale energy storage technology) [82–84] and molten oxide electrolysis cells (for electrochemical manufacture of iron and other metals) [85, 86], it may be useful to apply oscillating currents in those systems as well.

## 3.6 Acknowledgements

This chapter is based on material primarily from “Oscillating Currents Stabilize Aluminum Cells for Efficient, Low Carbon Production” which was printed in the journal *JOM* [9], and some material “Stabilizing Electrolysis Cells with Oscillating Currents: Amplitude, Frequency, and Current Efficiency” which was printed in the book *Light Metals 2022* [7]. Both have been modified to fit in this thesis. The thesis author and co-author Douglas Kelley wrote the original paper [9], and the thesis author wrote [7]. The thesis author was the primary author and was responsible for performing the data analysis, including creating videos of the interface height and displacement, plotting the RMS interface displacement with exponential fits, calculating the oscillation power spectra, and projecting the interface displacement onto the set of basis wave modes. The thesis author wrote all the custom MATLAB code to perform the analysis with the help and guidance from co-author Douglas Kelley, who also wrote the first version of the mode projection code. The thesis author produced all figures in this chapter, except Fig. 3.1 which was courtesy of co-author Marc Dupuis and Fig. 3.2 which was made by co-author Douglas Kelley. Co-author Marc Dupuis was responsible for running the TRIMET 180 kA Al cell simulations on MHD-Valdis software. Co-author Paul Funkenbusch and the thesis author guided oscillation current’s amplitude and frequency choices for the simulation campaign. The thesis author explained how the different mode pairs couple through the different components of the vertical magnetic field, and how the three mode coupling happens in the MPI. The thesis author found that the oscillating current is exciting standing waves and co-author Douglas Kelley came up with the hypothesis on the stabilization mechanism. Co-author Douglas Kelley came up with the idea of stabilization Al cell with oscillating currents and conceived this study. The thesis author is grateful for support from, and conversations with, Riccardo Betti that offered valuable insights at various points in this study. The thesis author is also grateful to David

Foster, Gerrit M. Horstmann, and Jonathan S. Cheng for fruitful discussions, and to Curtis Broadbent for leading the commercialization efforts of this work [12]. This work was supported by the National Science Foundation (CBET-1552182) and by a University of Rochester, URVentures TAG award.

# 4 Stabilizing Electrolysis Cells with Oscillating Currents: Oscillation Amplitude and Current Efficiency

This chapter is based on Reference [7]. It has been reformatted and edited to fit within the thesis. The thesis author was the primary author of this work. §4.4 is entirely unpublished results from a correspondence between the thesis author and Dr. Marc Dupuis, a co-author of [7].

## 4.1 Introduction

In Chapter 3 I showed that oscillating currents can prevent the MPI in simulations of a TRIMET 180 kA electrolysis cell, which allows the electrolysis cell to operate stably at a lower ACD than with steady current only. As discussed in §3.5, with the oscillating current added, we were able to reduce the ACD from 4.3 cm to 3.8 cm while maintaining cell stability in our simulations, reducing the average total power consumption of the cell by 4%. This has the promise of less energy intensive production, electricity savings, and less carbon emissions for the Al industry.

Thus, it is important to study how this stabilization technique can be optimized so more benefits can be reaped. The oscillation current has two parameters, its amplitude and frequency, and optimization boils down to the choice of these parameters. For example, for a given ACD and oscillation frequency, using a smaller oscillation amplitude to stabilize the cell would be more advantageous as this would translate to higher energy savings. On the other hand, if using a higher oscillation amplitude allows decreasing the ACD even further, then it might be worth it.

#### 4.1.1 Current Efficiency

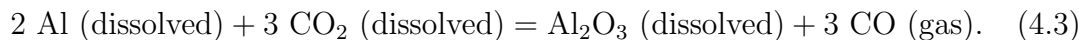
Another key operational parameter for Al cells is current efficiency (CE), which is a measure of how productive an Al electrolysis cell is. Specifically, the theoretical production rate in an Al cell can be found using Faraday’s law for electrolysis [2]:

$$p_0 = \frac{M}{zF}I, \quad (4.1)$$

where  $p_0$  is the production rate in (g/s),  $M$  is the molecular mass in (g),  $z$  is the number of electrons involved in the reaction,  $F$  is the Faraday constant, and  $I$  is the electrolysis current. The theoretical production rate is proportional to the electrolysis current, and ideally, all the current should liberate Al atoms from solution. However, in reality “losses” occur where the current is instead travelling short circuit paths between the electrodes, or when the back reaction occurs forming new alumina. These losses are typically quantified by the current efficiency

$$\text{CE} = \frac{p}{p_0} * 100\%, \quad (4.2)$$

where  $p$  is the measured production rate in (g/s). The biggest loss in CE comes from the back reaction occurring between the dissolved Al metal and carbon dioxide (CO<sub>2</sub>) bubbles [2]:



This reaction is estimated to cause a  $\approx 3\text{-}5\%$  loss in CE [2]. A model of the reaction rate [2, 87] predicts the current efficiency to be

$$\text{CE} = 100\% - k_{al} A (c_{al}^0 - c_{al}), \quad (4.4)$$

where  $k_{al}$  is the mass transfer coefficient between Al and bath,  $A$  is the surface area of the Al-bath interface,  $c_{al}^0$  is the thermodynamic saturation solubility of Al in the bath, and  $c_{al}$  is the amount of Al actually dissolved. The mass transfer coefficient  $k_{al}$  can be approximated as [2, 87, 88]:

$$k_{al} = c D^{0.67} \mu_{el}^{-0.5} u_{rel}^{0.83} \rho_{el}^{0.5} \text{ACD}^{-0.17} \quad (4.5)$$

where  $c$  is a constant,  $D$  is the diffusivity of the dissolved Al in the electrolyte,  $\mu_{el}$  is the viscosity of the electrolyte,  $u_{rel}$  is the relative speed between the Al and electrolyte, and  $\rho_{el}$  is the density of the electrolyte. Substituting Eq. 4.5 into Eq. 4.4, we can write CE as:

$$\text{CE} = 100\% - c D^{0.67} \mu_{el}^{-0.5} u_{rel}^{0.83} \rho_{el}^{0.5} \text{ACD}^{-0.17} A (c_{al}^0 - c_{al}) \quad (4.6)$$

The oscillating current is stabilizing Al electrolysis cells by exciting standing waves, which impacts some of the parameters in Eq. 4.6 such as changing the Al-electrolyte interface surface area. I will explore some of the effects using an oscillating current might have on the cell's CE.

This chapter proceeds as follows: In §4.2 I discuss the impact of using a low amplitude oscillating current, high amplitude oscillating current, and high frequency oscillating current on the 180 kA TRIMET Al electrolysis cell stability in simulation. In §4.3 I discuss how using the oscillating current might impact CE of the electrolysis cell through impacting different parameters of Eq. 4.6 and cell noise, and attempt to quantify the change in CE resulting from each. Finally, in §4.5 I summarize the results and give some ideas for future work.

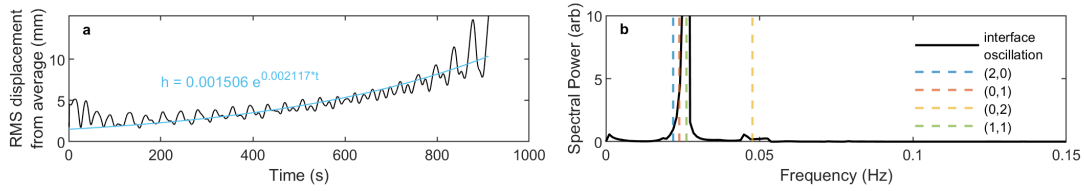


**Figure 4.1:** MPI present at 4 cm ACD, with an oscillating current of frequency 0.045 Hz and half-amplitude 2.9 kA. **a**, Root-mean-square displacement of the Al-electrolyte interface is growing exponentially in time. An exponential fit is shown in blue for  $t > 100$  s. **b**, The spectral power of the displacement of one point on the interface is dominated by a narrow frequency band, close to the frequency of interface wave modes  $G_{2,0}$ ,  $G_{0,1}$ , and  $G_{1,1}$ , expected in the MPI.

## 4.2 Oscillation Current Amplitude and Frequency

From the simulation results presented in Chapter 3, we know that the MPI is present at 4 cm ACD with a steady 180 kA current only (Figs. 3.6,3.8), and the RMS interface displacement had a growth rate of  $2.2 \times 10^{-3} \text{ s}^{-1}$  (see Fig. 3.6). Adding an oscillating current of frequency 0.045 Hz and half-amplitude 19.8 kA stabilized the cell and prevented the MPI (Fig. 3.12).

### 4.2.1 Oscillating Current with Small Amplitude

We wondered if we could stabilize the cell at 4 cm with an oscillating current at the same frequency but a much lower half-amplitude. To test, we ran a simulation at 4 cm ACD, with an an oscillating current of frequency 0.045 Hz and half-amplitude of 2.9 kA. The results are shown in Figs. 4.1-4.2. The Al electrolysis cell was unstable, with the interface RMS displacement growing exponentially in time (Fig. 4.1a) and the MPI present. The growth rate was  $2.1 \times 10^{-3} \text{ s}^{-1}$ , slightly lower than that with a steady current only of  $2.2 \times 10^{-3} \text{ s}^{-1}$ . The power spectrum of the interface displacement at a point, Fig. 4.1b, shows that its power is highly concentrated near 0.0263 Hz, the MPI frequency, and no peak was present at the current oscillation frequency of 0.045 Hz. I projected the interface displacement

shape into  $G_{m,n}$  wave modes. An example is shown in Figs. 4.2a-b where the interface displacement and estimated interface displacement are plotted at  $t = 125$  s, respectively. The condition number was again ( $\sim 4$ ), and the % error was  $\leq 2.5\%$  at all times (Fig. 4.2c). I plotted the RMS amplitude of each mode in Fig. 4.2d and found that the  $G_{2,0}$ ,  $G_{0,1}$ , and  $G_{1,1}$  modes associated with the MPI are strongest. The  $G_{0,2}$  and  $G_{4,0}$ , whose corresponding frequencies,  $f_{0,2}$  and  $f_{4,0}$ , nearly match the drive frequency were not present. The temporal variations of  $G_{2,0}$ ,  $G_{0,1}$ , and  $G_{1,1}$  modes' amplitudes, (Figs. 4.2e-f), show them oscillating at the MPI frequency.

At 19.8 kA half-amplitude, an oscillating current with the same frequency was able to stabilize the cell at 4 cm ACD, but not with a 2.9 kA half-amplitude. It seems that there is a minimum amplitude needed to excite the standing waves strongly enough to prevent the MPI and stabilize the cell.

### 4.2.2 Oscillating Current with Large Amplitude

We wondered if applying an oscillating current with a high amplitude would make the stabilization effect “stronger” and allow reducing the ACD even further. To test, we ran a simulation at 3.7 cm ACD, with an oscillating current of frequency 0.045 Hz and half-amplitude of 36 kA. The cell shorted within 85 s and the results are summarized in Fig. 4.3. The RMS interface displacement is very high (Fig. 4.3a), and the power spectrum of the displacement at a point shows a peak near the current oscillation frequency of 0.045 Hz, as shown in Fig. 4.3b. Plotting the Al-electrolyte interface right before the cell shorted in Fig. 4.3c, shows a wave whose amplitude is high enough to touch the anode i.e. greater than the ACD. Projecting the interface displacement onto the  $G_{m,n}$  modes shows that the  $G_{0,2}$  is the strongest with the  $G_{1,0}$ ,  $G_{0,1}$ , and  $G_{4,0}$  also present (Fig. 4.3e). The projection error being  $< 3\%$  for the duration of the simulation (Fig. 4.3d). The  $G_{0,2}$  and  $G_{4,0}$  modes have frequencies near the current oscillation frequency, and we expected

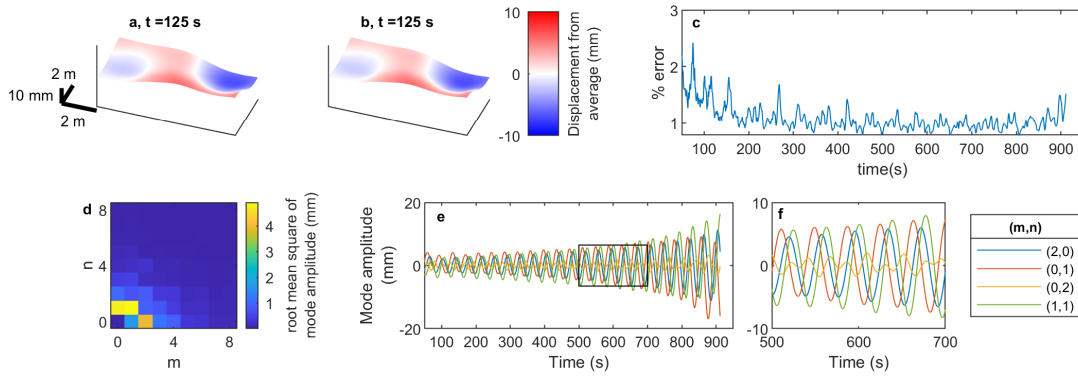


**Figure 4.2:** Modes at 4 cm ACD, with an oscillating current of frequency 0.045 Hz and half-amplitude 2.9 kA. **a**, Al-electrolyte interface displacement at  $t = 125$  s. **b**, Estimate of the interface displacement at  $t = 125$  s through performing a linear least-square projection onto the interface modes  $G_{m,n}$ . The estimated interface displacement looks visually the same as the actual interface displacement. **c**, The % error of the interface displacement estimate relative to the actual interface displacement. The error is very low and  $< 2.5\%$  at all times. **d**,  $G_{2,0}$ ,  $G_{0,1}$ , and  $G_{1,1}$  have greater root-mean-square amplitude than any other modes. **e**,  $G_{2,0}$ ,  $G_{0,1}$ , and  $G_{1,1}$  oscillate with a common frequency and grow over time.  $G_{0,2}$  oscillates with the same frequency but does not grow in time. **f**,  $G_{2,0}$  and  $G_{0,1}$  are separated in phase by  $\sim 90^\circ$ , characteristic of a traveling wave as in the MPI.

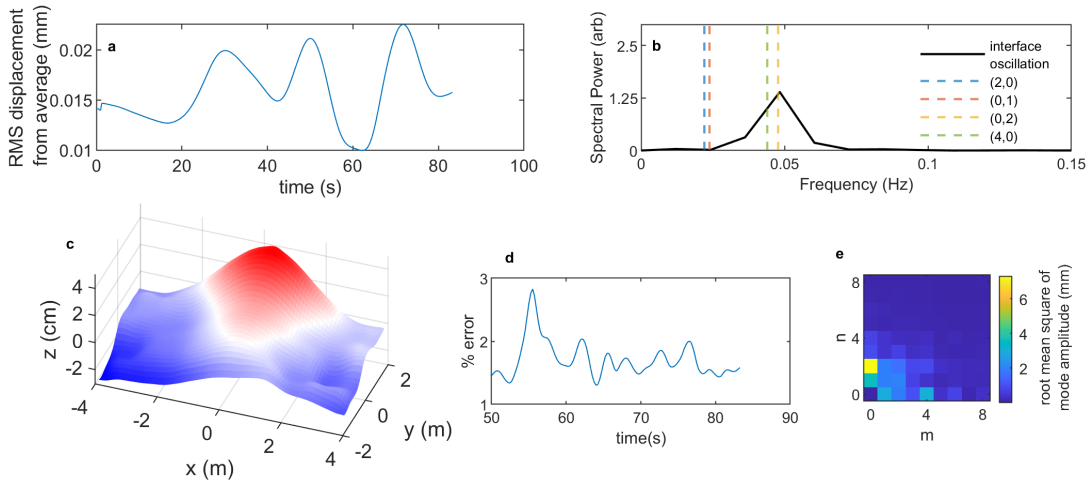


**Figure 4.3:** Al-electrolyte interface behaviour at 3.7 cm ACD, with an oscillating current of frequency 0.045 Hz and half-amplitude 36 kA. **a**, Al-electrolyte interface RMS displacement is very high, causing a short circuit. **b**, Power spectrum of interface displacement at a point shows a small peak near the oscillating current frequency **c**, The Al-electrolyte interface at  $t = 83.25$  s, right before the electrolysis cell shorted. A wave is present whose crest is high enough to touch the anode and cause a short-circuit. **d**, The % error of projecting the interface displacement onto the wave modes is  $< 3\%$  for the duration of the simulation. **e**,  $G_{0,2}$  mode is strongest.

to excite them. It seems that the high oscillation current amplitude excited a standing wave too strongly that it was higher than the ACD and shorted the cell. This observation indicates that using too high of an oscillating current amplitude can be dangerous and short the cell, and that the amplitude of the excited standing wave seems to correlate with the amplitude of the oscillating current.

### 4.2.3 Oscillating Current with High Frequency

We wondered if using a high frequency oscillating current would also stabilize the cell, and potentially be better than a low frequency oscillating current. To test, we ran a simulation at 4 cm ACD with an oscillating current of frequency 0.5 Hz and half-amplitude of 19.8 kA. The oscillation frequency is about an order of magnitude higher than 0.045 Hz we previously used to stabilize the cell at the same

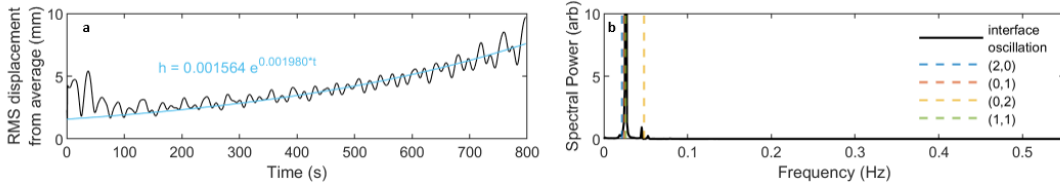


**Figure 4.4:** Al-electrolyte interface behaviour at 4 cm ACD, with an oscillating current of frequency 0.5 Hz and half-amplitude 19.8 kA. **a**, The Al-electrolyte interface grows exponentially, and the MPI is present. **b**, The spectral power of the displacement of one point on the interface is dominated by one frequency band close to the expected MPI frequency. The driving frequency of 0.5 Hz is absent.

ACD, and nearly equal to the high order frequencies  $f_{44,0}$  and  $f_{0,20}$ . The interface displacement grew exponentially in time (Fig. 4.4a) but at a lower growth rate than the case without an oscillating current. The power spectrum of the interface displacement at a point (Fig. 4.4b) shows no peak near the drive frequency of 0.5 Hz. We believe that the high frequency oscillations were damped out by dissipative effects, such as the friction between the fluid layers and electrodes, and the turbulent viscosity [8, 29].

## 4.3 On the Impact of Exciting Standing Waves on Current Efficiency

### 4.3.1 Surface Area and Wave Amplitude

The oscillating current is stabilizing the Al electrolysis cell by exciting standing waves on the Al-electrolyte interface that frustrate the MPI [9]. As shown by Eq. 4.4, CE is inversely proportional with the the surface area of the Al-electrolyte  $A$ , so we wondered if driving standing waves on the interface would decrease CE. If  $z = S(x, y, t)$  represents the interface, then its surface area can be calculated

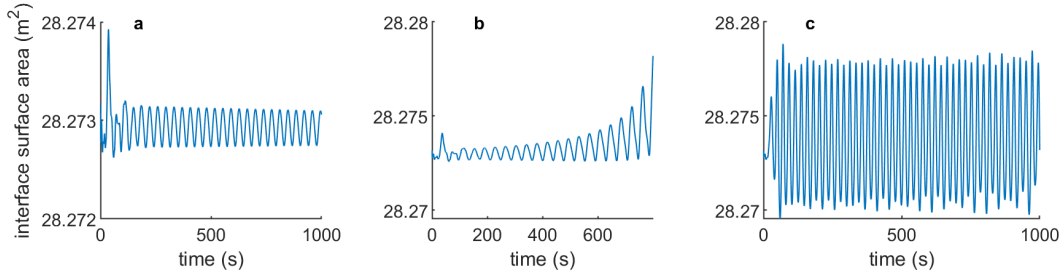


**Figure 4.5:** Interface area in stable, unstable, and stabilized electrolysis cells **a**, Al-electrolyte interface surface area as a function of time for a stable Al cell operating with a steady 180 kA current at 4.3 cm ACD. The surface area oscillates in time and decreases very slowly. **b**, Interface surface area for a cell operating with a 180 kA steady current at 4 cm ACD. The surface area is growing in time, which is consistent with the cell being unstable and the MPI present. **c**, Interface surface area for a cell operating at 4 cm ACD, but with the steady 180 kA current supplemented with an oscillating current of half-amplitude 19.8 kA and of frequency 0.045 Hz. The surface area oscillates in time and does not grow, consistent with the cell being stable. The interface surface area is larger than that of panel **a** due to the excited standing waves by the oscillating current.

by

$$A(t) = \int_{-L_x/2}^{L_x/2} \int_{-L_y/2}^{L_y/2} \sqrt{S_x^2 + S_y^2 + 1} \, dy \, dx, \quad (4.7)$$

where  $S_x$  and  $S_y$  are the partial derivatives of  $S(x, y, t)$  in the  $x$  and  $y$  directions, respectively. I numerically calculated the surface area of the interface given by Eq. 4.7 at every instant in time using a custom MATLAB script for different simulations of the Al electrolysis cell, when the cell is critically stable at 4.3 cm ACD with 180 kA steady current, when the cell is unstable at 4 cm ACD with 180 kA steady current, when the cell is stable at 4 cm ACD with 180 kA steady current supplemented with an oscillating current at of half-amplitude 19.8 kA and of frequency 0.045 Hz. The results are summarized in Fig. 4.5.

When the cell is stable at 4.3 cm ACD with a steady current, the surface area of the Al-electrolyte interface oscillates in time about a mean value of 28.2729 m<sup>2</sup> and an amplitude of 2 cm<sup>2</sup>, as shown in Fig. 4.5a. When the ACD is reduced

by 7% to 4 cm and the cell is unstable with the MPI present, the surface area oscillates and grows exponentially in time as shown in Fig. 4.5b. At the same ACD, when the steady current is supplemented with an oscillating current of 19.8 kA half-amplitude and 0.045 Hz frequency the cell is stable, and the surface area oscillates but does not grow in time, as shown in Fig. 4.5c. The mean surface area in this case is 28.2735 m<sup>2</sup>, 6 cm<sup>2</sup> higher than it was at 4.3 cm ACD and steady current (Fig. 4.5a), and its amplitude is  $\sim 42$  cm<sup>2</sup> (Fig. 4.5c). Although the mean surface area is higher when an oscillating current is added, the change is very small and does not meaningfully affect CE.

However, the surface area amplitude is much higher than it was before (see Figs. 4.5a,c). This can negatively impact CE as it could increase the chance of the Al layer reaching the CO<sub>2</sub> gas bubbles at the anode and driving the back reaction of Eq. 4.3 [17]. This can be roughly quantified by the overlap between the distribution of the height of the Al-electrolyte interface and the distribution of CO<sub>2</sub> gas bubbles at the anodes, as illustrated by Fig. 4.6. Note that the distribution may not be normal for either of the interface height or the CO<sub>2</sub> gas bubbles. I calculated Al-electrolyte interface distribution for the same electrolysis cell simulations in Fig. 4.5, and plotted the results in Fig. 4.7. The interface height distribution for a stable cell with steady current of 180 kA and at the critical ACD of 4.3 cm, Fig. 4.7a, does not look normal or symmetric about a flat interface, where the height is zero. When the MPI is present at 4 cm ACD for the same steady current, the interface height distribution looks more like a normal one (Fig. 4.7b), with the interface height reaching a high enough level to touch the anodes and short the cell. For a stable cell at 4 cm ACD, when the steady 180 kA current is supplemented with an oscillating current of 19.8 kA half-amplitude and 0.045 Hz frequency, the interface height distribution looks bimodal, as shown in Fig. 4.7c. Compared to the stable case with steady current in Fig. 4.7a, the interface height is above 2 cm more often indicating that exciting

the standing waves with the oscillation current is making the interface height higher comparatively. However, in [89] it was reported that the largest bubbles had a thickness of 4.55 mm, about 0.5 cm. With the ACD at 4 cm and the maximum interface height at 2.8 cm, the interface height is not high enough for the Al metal to touch the gas bubbles and trigger the back reaction.

In another simulation, we were able to stabilize the electrolysis cell at an even lower ACD of 3.8 cm using an oscillating current of half-amplitude 19.8 kA and of frequency 0.045 Hz (see Fig. 3.15). I plotted the interface height distribution in Fig. 4.8 normalized as a probability and overlaid the normalized interface height distribution of Fig. 4.7a on it. Similar to before, exciting the standing waves with the oscillating current is increasing the interface height. I plotted the distribution of the maximum interface height at every instant in time in Fig. 4.9 overlaid with that for the cell stabilized with the oscillating current but at 4 cm ACD. Although the oscillation current was the same, the maximum interface height distribution takes on higher values at 3.8 cm ACD. I believe this is due to MPI being stronger in the cell with lower ACD [8, 28]. The maximum interface height is 3.2 cm and for gas bubbles 0.5 cm thick at the anode, the Al layer is only 0.1 cm away from touching the gas bubbles at 3.8 cm ACD. As the oscillating current is used to stabilize the Al electrolysis cells at even lower ACD, this might lead to a reduction in CE. The distribution of gas bubbles at the anodes is needed to quantify the effect on CE.

### 4.3.2 Back Reaction Rate

Based on the back reaction rate model of Eq. 4.5, using the oscillating current to decrease the ACD can lower CE. We were able to reduce the ACD from 4.3 cm with steady current only to 3.8 cm with the oscillating current, while maintaining stable cell operation. This represents an 11.6% reduction, so the new ACD is

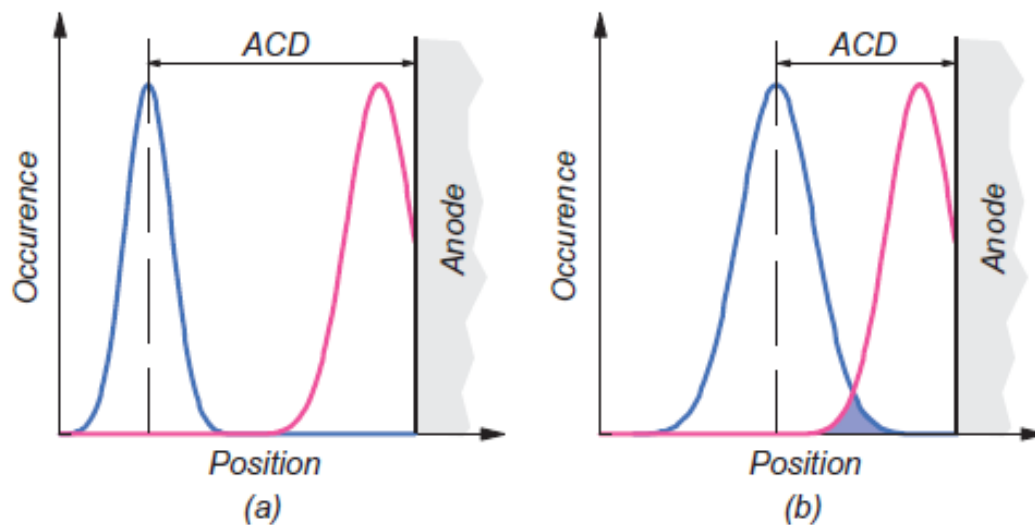


**Figure 4.6:** Illustration of back reaction region with decreasing ACD. **a**, Distribution of interface height of the Al-electrolyte interface is in blue, and of the CO<sub>2</sub> gas bubbles forming on the anode is in pink. **b**, When the ACD is reduced and an overlap between the Al metal and CO<sub>2</sub> bubbles distribution occurs, the back reaction takes place reducing CE. Reprinted by permission from Springer Nature Customer Service Centre GmbH: Springer Nature, *Light Metals 2014*, “Current Efficiency in Aluminium Reduction Cells: Theories, Models, Concepts, and Speculations”, Asbjørn Solheim (2014) [17]

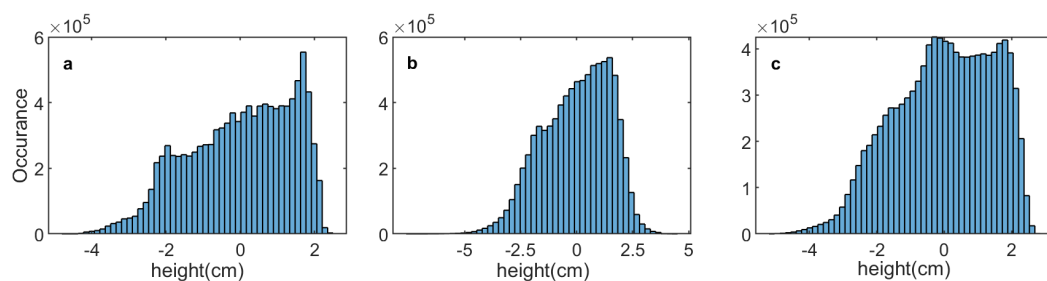


**Figure 4.7:** Distribution of Al-electrolyte interface height in stable, unstable, and stabilized electrolysis cells. **a**, Al-electrolyte interface height distribution for a stable Al cell operating with a steady 180 kA current at 4.3 cm ACD. **b**, Interface height distribution for a cell operating with a 180 kA steady current at 4 cm ACD. The cell is unstable with the MPI present and shorted. **c**, Interface height distribution for a cell operating at 4 cm ACD, but with the steady 180 kA current supplemented with an oscillating current of half-amplitude 19.8 kA and of frequency 0.045 Hz.

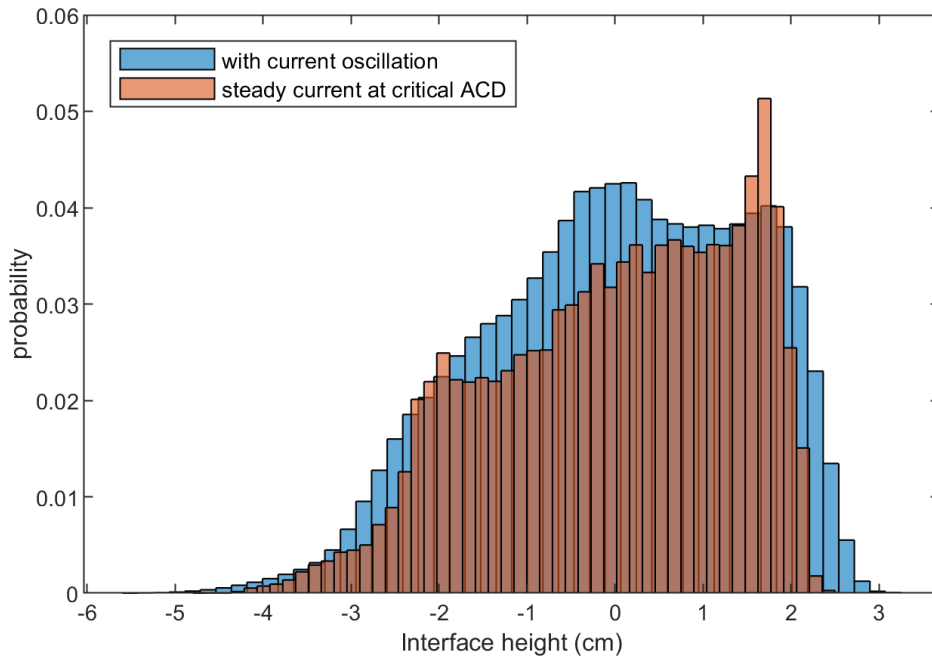


**Figure 4.8:** Distribution of Al-electrolyte interface height for a cell operating with steady current at 4.3 cm ACD, and cell operating at 4 cm ACD, but with the steady 180 kA current supplemented with an oscillating current of half-amplitude 19.8 kA and of frequency 0.045 Hz.

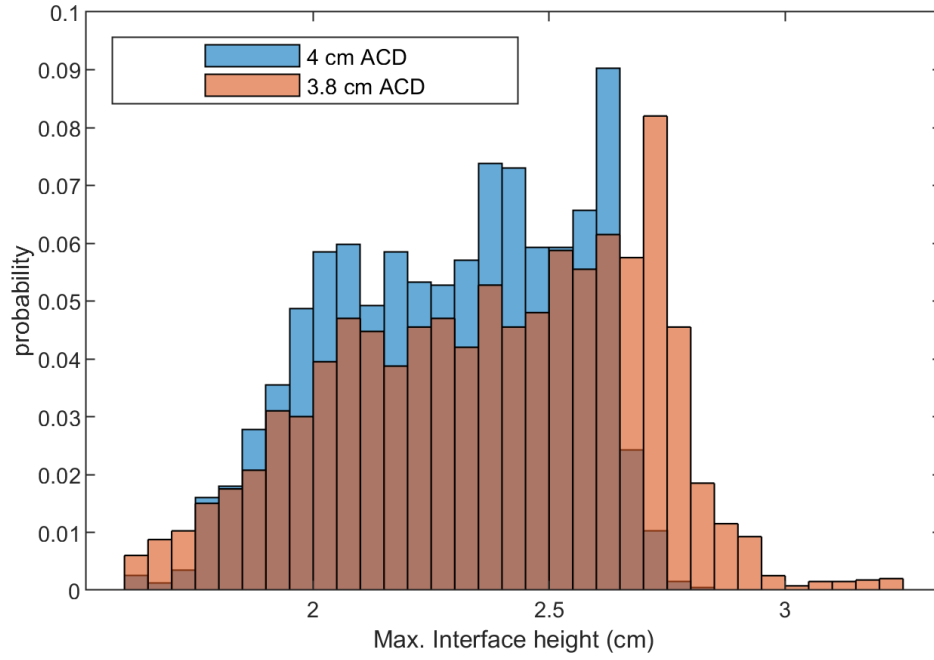


**Figure 4.9:** Distribution of maximum Al-electrolyte interface height at every instant in time for a cell operating the steady 180 kA current supplemented with an oscillating current of half-amplitude 19.8 kA and of frequency 0.045 Hz at 4 cm ACD, and another operating with the same current at 3.8 cm ACD.

0.884 times the original one. Using Eq. 4.6 and assuming that nothing changed but the ACD, the new CE of the cell would be:

$$\begin{aligned} \text{CE}_{new} &= 100\% - C (0.884 \times \text{ACD})^{-0.17} \\ &= 100\% - 1.02 \times C \text{ACD}^{-0.17} \end{aligned} \quad (4.8)$$

where  $C$  is a constant that stands for all the other terms. Assuming that the CE loss in the cell was originally 3 – 5% [2], which is equal to  $C \text{ACD}^{-0.17}$ , then the CE loss would be 3.06 – 5.1% at the reduced ACD. Thus, reducing the ACD by 11.6%, resulted in reducing the average total power by  $\sim 4\%$  (an energy gain), but decreased the CE by only  $\leq 0.1\%$  (a productivity loss).

Other than the impact of reducing the ACD, using the oscillating current might change the relative speed between the Al and the electrolyte,  $u_{rel}$ . This can either improve CE if  $u_{rel}$  is decreased, or worsen CE if  $u_{rel}$  is increased. For example, if the CE loss in the cell was originally 3 – 5%, then using Eq. 4.6, and holding all constant but  $u_{rel}$ , if  $u_{rel}$  is decreased/increased by 10% from using the oscillating current, this would increase/decrease the cell's CE by 0.25 – 0.42%. It would be important to check the relative speed between the Al-electrolyte while using the oscillating current in future work.

## 4.4 Cell Noise and Current Efficiency

Another factor impacting the Al electrolysis cell current efficiency not included in the model of Eq. 4.6 is cell noise. A simple way to define cell noise is the moving standard deviation of the normalized cell voltage  $V_n$  given by [90]:

$$V_n = \left( \frac{V - V_e}{I} \times I_n \right) + V_e \quad (4.9)$$

where  $V_e$  is the cell voltage at zero current ( $= 1.65 \text{ V}$ ),  $I$  is the current, and  $I_n$  is the target line current ( $= 180 \text{ kA}$ ). Increased cell noise decreases CE [90–92],

and cell noise increases with higher cell voltage fluctuations amplitude [91]. Using the oscillating current to stabilize the cell resulted in higher voltage fluctuations when compared to those with steady current at the critical ACD (see Fig. 3.4b and Fig. 3.11b), which could indicate an increase in cell noise too. To check, I calculated the cell noise for a stable TRIMET Al electrolysis cell operating with steady current of 180 kA at 4.3 cm, an unstable cell operating with the same steady current at 4 cm ACD, a stable cell operating at 4 cm ACD and with the steady current supplemented by an oscillating current of half-amplitude 19.8 kA and of frequency 0.045 Hz, and a stable cell operating at 3.8 cm ACD and with the steady current supplemented by an oscillating current of half-amplitude 19.8 kA and of frequency 0.045 Hz. The results are summarized in Fig. 4.10.

When the cell is operating at the critical ACD with a steady current, Fig. 4.10a, the cell noise is low having an average value of 0.011 dV for  $t \geq 150$  s. When the ACD is reduced to 4 cm and the cell is unstable with the MPI present, the cell noise is quite high as expected, Fig. 4.10b, reaching 0.38 dV before the cell shorted, near the cell noise value reported in [93]. When the cell is stabilized by the action of the oscillating current, Fig. 4.10c, the cell has an average value of 0.073 dV for  $t \geq 150$  s, higher than that in Fig. 4.10a for a stable cell with the steady current only. For a stable cell at 3.8 cm with the same oscillating current, the cell noise is slightly higher with an average of 0.076 dV for  $t \geq 150$  s. Thus, decreasing the ACD from 4.3 cm to 3.8 cm by using an oscillating current, resulted in increasing the cell noise by 0.065 dV. This will decrease CE but it is hard to quantify by how much as the correlation between cell noise and CE is often empirically derived [92] and changes smelter to smelter. The correlation between cell noise and CE for the TRIMET 180 kA cell, and the definition of cell noise TRIMET uses, would be both needed to quantify the impact of increased cell noise by oscillating the current on CE.

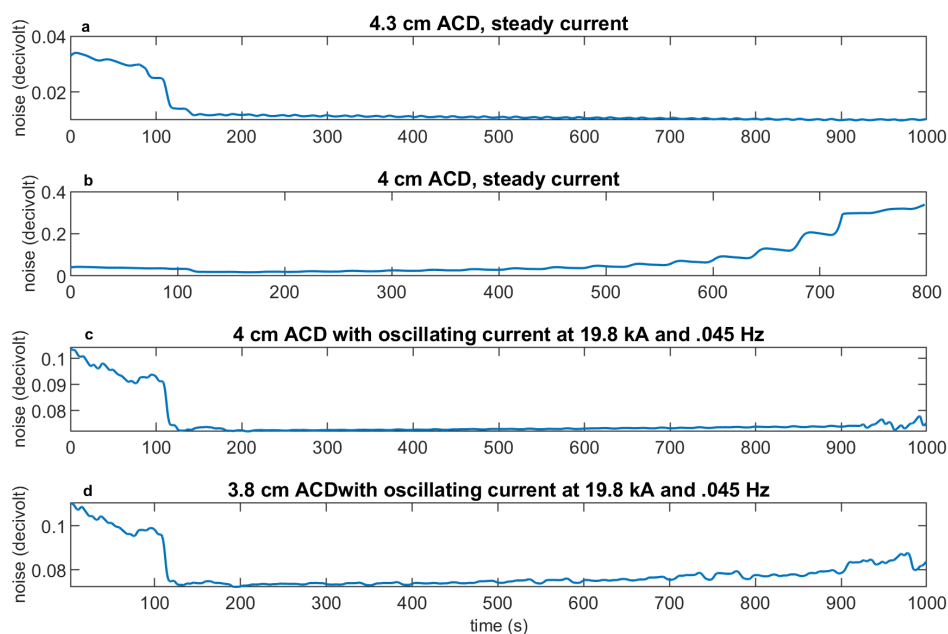


**Figure 4.10:** Cell noise for TRIMET 180 kA Al electrolysis cells operating at different currents and ACD. **a**, Cell operating with steady current of 180 kA at 4.3 cm. **b** Unstable cell operating with steady current of 180 kA at 4 cm. **c** Cell operating at 4 cm ACD and with the steady current supplemented by an oscillating current of half-amplitude 19.8 kA and of frequency 0.045 Hz. **d** Cell operating at 3.8 cm ACD and with the steady current supplemented by an oscillating current of half-amplitude 19.8 kA and of frequency 0.045 Hz.

## 4.5 Summary and Future Work

In this chapter, I discussed aspects of industrial importance about using an oscillating current to stabilize Al electrolysis cells, specifically the choice of oscillation amplitude, oscillation frequency, and the impact of using current oscillation on the cell's current efficiency. For reference, adding an oscillating current, with half-amplitude 19.8 kA and frequency 0.045 Hz, allows for stable operation of the TRIMET 180 kA cell at 4 cm ACD and 3.8 cm ACD. I showed that using an oscillating current at the same frequency but a 2.9 kA half-amplitude is not enough to stabilize the same cell at 4 cm ACD. This implies that there is a minimum oscillating current amplitude required for the stabilization effect to be strong enough to prevent the MPI. Also, I showed that using a 36 kA half-amplitude current oscillation at the same frequency excites a standing wave high enough to short the electrolysis cell at 3.7 cm ACD. Therefore, it seems that there exists an optimal choice for the oscillating current amplitude such that it is high enough to prevent the MPI, but as low as possible to save on electric power and not excite high standing waves that can short the cell. I also showed that using a current with 0.5 Hz oscillation frequency and 19.8 kA half-amplitude has a minimal stabilization effect, and it is not strong enough to stabilize the cell. We believe that the high frequency oscillations were damped out by dissipative effects, such as the friction between the fluid layers and electrodes, and the turbulent viscosity. However, further simulations are needed to verify.

As for the impact of using an oscillating current on the Al electrolysis cell's CE, I discussed the consequences of exciting standing waves on the Al-electrolyte interface, the back reaction rate, and the cell noise. Exciting standing waves on the interface by the oscillating current can reduce CE by increasing the interfacial surface area and by increasing the likelihood of the Al metal reaching the gas bubbles at the anodes. I showed that when using the oscillating current,

the interfacial surface area does increase when compared to that with steady current, however, this increase was not meaningful to impact CE. Also, I showed that using the oscillating current results in higher interface heights which could decrease CE at low ACD if the distribution of wave height overlaps with that of the gas bubbles at the anodes. The distribution of the gas bubbles at the anodes of the TRIMET 180 kA cell is needed to quantify the overlap between the interface height distribution and the gas bubbles, and consequently the impact on CE. Decreasing the ACD via the oscillating current, directly decreases CE as shown by Eq. 4.6. For the 11.6% ACD reduction we were able to achieve in simulation, it would result in only  $\sim 0.1\%$  reduction in CE. Using the oscillating current probably affects the relative speed between the Al and electrolyte, which can have a positive/negative impact on CE if the speed is reduced/increased. Considering the relative speed in future work is very important. Finally, I showed that using the oscillating current increased the cell noise by 0.065 dV compared to the steady current only case. It is not possible to quantify the decrease in CE caused by the noise without an empirical model for the correlation between cell noise and CE for the TRIMET 180 kA cell.

Achieving an 11.6% ACD decrease, from 4.3 cm with steady current to 3.8 cm with an oscillating current, resulted in reducing the average total power consumption by 4%. Adequately accounting for the impact this has on CE will give a more complete picture and is crucial for industry to assess if using this method is financially profitable. The model used for CE of Eq. 4.6 is not perfect as, for example, it doesn't take into account cell noise, which is shown to reduce CE [90, 92]. Testing the idea in an actual cell is the best way to quantify the impact of oscillating currents on CE. In all cases, it seems that optimizing the choice of oscillating current amplitude and frequency is about finding the combination that would balance using the least power, reducing the ACD the most, and improve CE or reduce it the least. Running more simulation to map out the oscillating current

amplitude-frequency stability phase space for different ACD would aid in finding the optimum combination to use. Also, it was shown recently [94] that oscillating the currents in the magnetic compensation loops also has a stabilizing effect on the Al electrolysis cell. This is easier on the power grid operation, as the potline current will be kept constant [94]. Exploring this idea in detail by checking which oscillating current amplitudes and frequencies can stabilize the cell is important.

## 4.6 Acknowledgements

This chapter is based on material primarily from “Stabilizing Electrolysis Cells with Oscillating Currents: Amplitude, Frequency, and Current Efficiency” which was printed in the book *Light Metals 2022* [7], and some unpublished work aimed at expanding the discussion of the impact of using oscillating currents on current efficiency. The material from the paper [7] has been modified to fit in this thesis. The thesis author was the primary author and was responsible for writing the paper, performing all the data analysis, writing the custom MATLAB code to perform the analysis, and producing all the figures except where it was noted in the caption. Working out the impact of using the oscillating current on cell noise was done through a correspondence between the thesis author and co-author Marc Dupuis. Co-author Marc Dupuis was responsible for running the TRIMET 180 kA Al cell simulations on MHD-Valdis software, and provided guidance on the topic of Al electrolysis cell current efficiency. Co-author Paul Funkenbusch and the thesis author guided oscillation current’s amplitude and frequency choices for the simulation campaign. Co-author Douglas Kelley came up with the idea of stabilization Al cell with oscillating currents, and provided guidance and support throughout this work. The thesis author is grateful to Riccardo Betti, David Foster, Gerrit M. Horstmann, and Jonathan S. Cheng for fruitful discussions, and to Curtis Broadbent for leading the commercialization efforts of this work [12].

This work was supported by the National Science Foundation (CBET-1552182) and by a University of Rochester, URVentures TAG award.

## 5 Conclusion

The metal pad instability (MPI) imposes a limit on the anode-to-cathode distance (ACD) in aluminium (Al) electrolysis cells which, consequently, prevents the cells from being more energy efficient as about 50% of the cell's energy consumption produces no Al, and is instead transformed into heat by the high electrical resistance of the electrolyte [9]. This thesis presented an exploration of a novel idea for stabilizing aluminium (Al) electrolysis cells: using an oscillating current to prevent the metal pad instability (MPI).

In chapter 2, I extended the mechanical model of the MPI presented in [8] to include an additional oscillating current component with a specific angular frequency and amplitude, to test whether the oscillating current component can stabilize it. I derived the equations of motion of the extended model, and solved them numerically in MATLAB. The results showed that the oscillating current stabilized the model, and that the stability depended on the choice of the oscillating current's amplitude and frequency. Also, as the model became more unstable fewer choices of the oscillating current's amplitude and frequency stabilized the model.

In chapter 3, we tested the idea of oscillating the current in a suite of numerical simulations of a TRIMET 180 kA Al electrolysis cell. The results showed that a

4.3 cm ACD is needed for stable operation with a steady current, and that the MPI is present if the ACD is reduced below that threshold. Oscillating the current of the cell allowed for stable cell operation at 11.6% lower ACD than with steady current only, and required 4% less electrical power. The current is oscillated at a frequency chosen to excite standing waves on the Al-electrolyte interface that frustrate the MPI [9].

In chapter 4, we showed that a minimum oscillating current amplitude is needed to stabilize the cell, and that too high an amplitude can excite standing waves large enough to short the cell. We also explored the potential impact oscillating the current might have on the cell's current efficiency (CE). Using the oscillating current increased the cell noise, which can be detrimental to CE. Reducing the ACD while exciting high amplitude standing waves could impact CE the most, however, a distribution of the gas bubbles at the anodes is needed to quantify the impact. Testing the oscillating current in a real electrolysis cell is the only way to know the true impact on CE.

### 5.0.1 Future Directions

The extended mechanical model of the MPI with the oscillating current added in chapter 2 can be extended further to include a damping term to mimic the damping effects present in an actual Al electrolysis cell. Although damping will have a stabilizing effect on the model, it would better mimic an electrolysis cell, and be interesting study the stability in combination with the oscillating current. One way to include damping would be to introduce a friction term at the pivot point of the pendulum, which was suggested to the author by Dr. Marc Dupuis. Additionally, one can change the location of the pivot point from the fixed wall to the top of the aluminium plate, and create a different model of the MPI as suggested by Dr. Marc Dupuis in [94].

Exploring the amplitude-frequency stability phase space in the Al electrolysis simulations would be an obvious next step. It would allow finding the minimum oscillating current amplitude needed for a given oscillation frequency which would translate to better power savings, and probably be easier to implement. Also, there might exist a frequency that is particularly more stable than others for a given cell. From our simulation results, we were able to stabilize the cell at 4 cm ACD with the oscillating current of frequency 0.045 Hz and 0.069 Hz but at 3.8 cm ACD with only the 0.045 Hz frequency. Also, testing higher frequencies above 0.1 Hz would be interesting.

In actual Al smelters, no two Al electrolysis cells are exactly the same. Thus, it is important to conduct sensitivity analysis on the stabilizing effect of the oscillating current as many operational parameters change from cell to cell in a potline such as the ledge thickness on the side of the cell which can vary by  $\pm 5 - 10$  cm from cell to cell. Such changes affect the electrolysis cell geometry and consequently the frequencies of the hydrodynamic gravity wave modes on the Al-electrolyte interface. Studying how much the modes creating the standing waves are driven if the excitation frequency differs slightly would be important.

In a recent publication [94], it was shown that oscillating the currents in the magnetic compensation loops also has a stabilizing effect on the Al electrolysis cell. This is easier on the power grid operation, as the potline current will be kept constant [94]. Exploring this idea in detail by checking which oscillating current amplitudes and frequencies can stabilize the cell, and how much the ACD can be reduced would be valuable.

The MPI is not the only limiting factor for lowering the ACD. Cell heat balance is another limiting factor, where a lot of heat is lost at the electrolysis cell's side walls so a ledge from frozen electrolyte can be formed. This frozen ledge is critical for containing the liquid molten electrolyte inside the electrolysis cell for an extended period of time.

## Bibliography

- [1] I. Aluminium, “Primary aluminium production statistics,” (2011-2021), [Online; accessed October 27, 2022], URL <https://international-aluminium.org/statistics/primary-aluminium-production/>.
- [2] T. Foosnaes, K. Grjotheim, R. Huglen, H. Kvande, B. Lillebuen, T. Mellerud, and T. Naterstad (Aluminium-Verlag, 1993), pp. 136–138.
- [3] I. Aluminium, “Primary aluminium smelting power consumption,” (2021), [Online; accessed October 27, 2022], URL <https://international-aluminium.org/statistics/primary-aluminium-smelting-power-consumption/>.
- [4] Enerdata, “Electricity domestic consumption,” (2019-2021), [Online; accessed October 27, 2022], URL <https://yearbook.enerdata.net/electricity/electricity-domestic-consumption-data.html>.
- [5] P. A. Davidson, “Overcoming instabilities in aluminium reduction cells: a route to cheaper aluminium,” *Materials science and technology* **16**, 475 (2000), ISSN 0267-0836.
- [6] N. Urata, in *TMS Annual Meeting* (2005), pp. 455–460, ISBN 0147-0809.
- [7] I. Mohammad, M. Dupuis, P. D. Funkenbusch, and D. H. Kelley, in *Light Metals 2022*, edited by D. Eskin (Springer International Publishing, Cham, 2022), pp. 551–559, ISBN 978-3-030-92529-1.

- [8] P. A. Davidson and R. I. Lindsay, “Stability of interfacial waves in aluminium reduction cells,” *Journal of Fluid Mechanics* **362**, 273 (1998), ISSN 0022-1120.
- [9] I. Mohammad, M. Dupuis, P. D. Funkenbusch, and D. H. Kelley, “Oscillating currents stabilize aluminum cells for efficient, low carbon production,” *JOM* **74**, 1908 (2022), URL <https://doi.org/10.1007/s11837-022-05254-8>.
- [10] I. Mohammad and D. H. Kelley, in *Light Metals 2022*, edited by D. Eskin (Springer International Publishing, Cham, 2022), pp. 512–519, ISBN 978-3-030-92529-1.
- [11] V. Bojarevics, “MHD-VALDIS Reference manual,”.
- [12] D. Kelley and I. Mohammad, “Systems and methods for energy efficient electrolysis cells,” (2021).
- [13] H. Kvande and W. Haupin, “Cell voltage in aluminum electrolysis: A practical approach,” *JOM* **52**, 31 (2000).
- [14] V. Capitalist, “All the metals we mined in 2021 in one visualization,” (2021), [Online; accessed October 27, 2022], URL <https://elements.visualcapitalist.com/all-the-metals-mined-in-2021/>.
- [15] K. Kabezya, T. Hara, and R. Paton, “A review of primary aluminium tapping models,” *SN Applied Sciences* **1**, 1 (2019).
- [16] H. Kvande and P. A. Drabløs, “The aluminum smelting process and innovative alternative technologies,” *Journal of Occupational and Environmental Medicine* **56**, S23 (2014).
- [17] A. Solheim, *Current efficiency in aluminium reduction cells: theories, models, concepts, and speculations* (Springer, 2014), pp. 753–758.

- [18] D. Rabinovich, “The allure of aluminium,” *Nature Chemistry* **5**, 76 (2013).
- [19] N. Gow and G. Lozej, “Bauxite,” *Geoscience Canada* **20**, 9 (1993).
- [20] J.-F. Gerbeau, C. Le Bris, and T. Lelièvre, *Mathematical methods for the magnetohydrodynamics of liquid metals*, vol. 9780198566656 (Oxford University Press, Oxford, 2006).
- [21] C. Li, J. Wang, Y. Zhou, D. Chai, Z. Shi, Y. Wang, and S. Bao, *The aluminium electrolysis cell heat balance challenge under low voltage* (Springer, 2021), pp. 413–418.
- [22] M. Dupuis, *How to limit the heat loss of anode stubs and cathode collector bars in order to reduce cell energy consumption* (Springer, 2019), pp. 521–531.
- [23] M. Dupuis and V. Bojarevics, “Weakly coupled thermo-electric and mhd mathematical models of an aluminium electrolysis cell,” *Light Metals* **1**, 449 (2005).
- [24] U. E. I. Administration, “Electricity explained, use of electricity,” (2021), [Online; accessed October 27, 2022], URL <https://www.eia.gov/energyexplained/electricity/use-of-electricity.php#:~:text=Total%20U.S.%20electricity%20consumption%20in,consumers%20and%20direct%20use%20electricity>.
- [25] B. Lillebuen, S. Ytterdahl, R. Huglen, and K. Paulsen, “Current efficiency and back reaction in aluminium electrolysis,” *Electrochimica acta* **25**, 131 (1980).
- [26] W. Haupin, *Interpreting the components of cell voltage* (Springer, 2016), pp. 153–159.
- [27] K. A. Pericleous, V. Bojarevics, and G. S. Djambazov, in *Solidification Processing of Metallic Alloys Under External Fields* (Springer, 2018), pp. 75–118.

- [28] T. Sele, “Instabilities of the metal surface in electrolytic alumina reduction cells,” *Metallurgical Transactions B* **8**, 613 (1977), ISSN 0360-2141.
- [29] Bojarevics and M. V. Romerio, “Long waves instability of liquid-metal electrolyte interface in aluminum electrolysis cells - a generalization of sele criterion,” *European journal of mechanics, B, Fluids* **13**, 33 (1994), ISSN 0997-7546.
- [30] P. Davidson, “An energy analysis of unstable, aluminium reduction cells,” *European Journal of Mechanics B-fluids* **13**, 15 (1994).
- [31] O. Zikanov, A. Thess, P. Davidson, and D. Ziegler, “A new approach to numerical simulation of melt flows and interface instability in hall-héroult cells,” *Metallurgical and Materials Transactions B* **31**, 1541 (2000).
- [32] A. Lukyanov, G. El, and S. Molokov, “Instability of mhd-modified interfacial gravity waves revisited,” *Physics letters. A* **290**, 165 (2001), ISSN 0375-9601.
- [33] N. Urata, in *Light Metals: Proceedings of Sessions, AIME Annual Meeting* (1985), pp. 581–591, ISBN 0147-0809.
- [34] K. Mori, K. Shiota, N. Urata, and H. Ikeuchi, “The surface oscillation of liquid metal in aluminum reduction cells,” *Paper from” Light Metals 1976”*. **1** (1976).
- [35] P. A. Davidson, *Introduction to Magnetohydrodynamics* (Cambridge University Press, 2016), ISBN 9781316672853.
- [36] P. H. Roberts, *An introduction to magnetohydrodynamics*, vol. 6 (Longmans London, 1967).
- [37] M. Leitner, T. Leitner, A. Schmon, K. Aziz, and G. Pottlacher, “Thermophysical properties of liquid aluminum,” *Metallurgical and Materials Transactions A* **48**, 3036 (2017).

- [38] P. K. Kundu, I. M. Cohen, and D. R. Dowling, *Fluid mechanics* (Academic press, 2015).
- [39] A. D. Sneyd and A. Wang, “Interfacial instability due to mhd mode coupling in aluminium reduction cells,” *Journal of fluid mechanics* **263**, 343 (1994), ISSN 0022-1120.
- [40] G. Politis and J. Priede, “fractality of metal pad instability threshold in rectangular cells,” *Journal of fluid mechanics* **915** (2021), ISSN 0022-1120.
- [41] J. Givry, “Computer calculation of magnetic effects in the bath of aluminum cells,” *AIME MET SOC TRANS* **239**, 1161 (1967).
- [42] P. Davidson, “Overcoming instabilities in aluminium reduction cells: a route to cheaper aluminium,” *Materials Science and Technology* (2000).
- [43] W. Herreman, C. Nore, J. L. Guermond, L. Cappanera, N. Weber, and G. M. Horstmann, “Perturbation theory for metal pad roll instability in cylindrical reduction cells,” *Journal of fluid mechanics* **878**, 598 (2019), ISSN 0022-1120.
- [44] R. Moreau and D. Ziegler, “Stability of aluminum cells—a new approach,” *Light Metals 1986*. **2**, 359 (1986).
- [45] S. Pigny and R. Moreau, “Stability of fluid interfaces carrying an electric current in the presence of a magnetic field,” *European journal of mechanics. B, Fluids* **11**, 1 (1992).
- [46] A. D. Sneyd, “Stability of fluid layers carrying a normal electric current,” *Journal of Fluid Mechanics* **156**, 223 (1985).
- [47] A. D. Sneyd, “Interfacial instabilities in aluminium reduction cells,” *Journal of Fluid Mechanics* **236**, 111–126 (1992).

- [48] J. Descloux, Y. Jaccard, and M. Romerio, “A bidimensional stability result for aluminium electrolytic cells,” *Journal of Computational and Applied Mathematics* **38**, 77 (1991).
- [49] P. Maillard and M. Romerio, “A stability criterion for an infinitely long hall-heroult cell,” *Journal of computational and applied mathematics* **71**, 47 (1996).
- [50] H. Sun, O. Zikanov, and D. P. Ziegler, “Non-linear two-dimensional model of melt flows and interface instability in aluminum reduction cells,” *Fluid Dynamics Research* **35**, 255 (2004), URL <https://dx.doi.org/10.1016/j.fluiddyn.2004.06.003>.
- [51] R. Moreau and J. Evans, “An analysis of the hydrodynamics of aluminum reduction cells,” *Journal of the Electrochemical Society* **131**, 2251 (1984).
- [52] V. Bojarevics, *Nonlinear waves with electromagnetic interaction in aluminium electrolysis cells* (American Institute of Aeronautics and Astronautics, Inc., 1998), chap. 58, pp. 833–848, URL <https://doi.org/10.2514/5.9781600866531.0833.0848>.
- [53] A. Pedcenko, S. Molokov, and B. Bardet, “The effect of “wave breakers” on the magnetohydrodynamic instability in aluminum reduction cells,” *Metalurgical and Materials Transactions B* **48**, 6 (2017), ISSN 1073-5615.
- [54] A. Lützerath, *High Frequency Power Modulation - TRIMET smelters provide primary control power for stabilizing the frequency in the electricity grid* (2016), pp. 659–662, ISBN 978-3-319-65135-4.
- [55] V. Bojarevics and K. Pericleous, in *Fifth International Conference on CFD in the Process Industries CSIRO* (2006).

- [56] J.-F. Gerbeau and B. Perthame, Tech. Rep. (2006), URL <https://hal.inria.fr/inria-00072549>.
- [57] S. Molokov, A. Pedcenko, R. Chahine, and N. Chailly, “The onset of instabilities and finite amplitude waves in a model of aluminum reduction cells with nonuniform cathode current,” *Physics of Fluids* **33**, 034108 (2021), <https://doi.org/10.1063/5.0039232>, URL <https://doi.org/10.1063/5.0039232>.
- [58] F. Schilder and B. Peckham, “Computing arnol’d tongue scenarios,” *Journal of computational physics* **220**, 932 (2007).
- [59] D. J. Daniel, “Exact solutions of Mathieu’s equation,” *Progress of Theoretical and Experimental Physics* **2020** (2020), ISSN 2050-3911, 043A01, <https://academic.oup.com/ptep/article-pdf/2020/4/043A01/33114067/ptaa024.pdf>, URL <https://doi.org/10.1093/ptep/ptaa024>.
- [60] J. N. Kutz, “Advanced differential equations: Asymptotics & perturbations,” (2020), URL <https://arxiv.org/abs/2012.14591>.
- [61] V. Bojarevics and K. Pericleous, in *TMS Light Metals* (2006), pp. 347–352, ISBN 0147-0809.
- [62] V. Bojarevics and K. A. Pericleous, *SHALLOW WATER MODEL FOR ALUMINIUM ELECTROLYSIS CELLS WITH VARIABLE TOP AND BOTTOM* (2008), pp. 569–574.
- [63] V. Bojarevics and K. Pericleous, in *TMS Light Metals*, edited by G. Bearne (2009), pp. 569–574, ISBN 0147-0809.
- [64] V. Bojarevics and K. Pericleous, in *TMS Annual Meeting* (2010), pp. 199–206, ISBN 0873397509;9780873397506;.

- [65] M. Dupuis, V. Bojarevics, and J. Freibergs, “Demonstration thermo-electric and mhd mathematical models of a 500 ka aluminum electrolysis cell: Part 2,” TMS Light Metals (2004).
- [66] M. Dupuis and V. Bojarevics, “Busbar sizing modeling tools: comparing an ansys® based 3d model with the versatile 1d model part of mhd-valdis,” Metals & Materials Society **2006**, 341 (2006).
- [67] D. S. Severo, V. Gusberti, A. F. Schneider, E. C. V. Pinto, and V. Potocnik, in *Essential Readings in Light Metals: Volume 2 Aluminum Reduction Technology*, edited by G. Bearne, M. Dupuis, and G. Tarcy (Springer International Publishing, Cham, 2016), pp. 379–384, ISBN 978-3-319-48156-2, URL [https://doi.org/10.1007/978-3-319-48156-2\\_54](https://doi.org/10.1007/978-3-319-48156-2_54).
- [68] V. Bojarevics and J. W. Evans, *Mathematical Modelling of Hall-Héroult Pot Instability and Verification by Measurements of Anode Current Distribution* (John Wiley & Sons, Inc, Hoboken, NJ, USA, 2015), pp. 783–788, ISBN 1119082447;9781119082446;9781119093435;1119093430;.
- [69] V. Bojarevics, E. Radionov, and Y. Tretiyakov, *Anode Bottom Burnout Shape and Velocity Field Investigation in a High Amperage Electrolysis Cell* (2018), pp. 551–556, ISBN 978-3-319-72283-2.
- [70] R. Shaoyong, Y. Feiya, M. Dupuis, V. Bojarevics, and Z. Jianfei, *Production Application Study on Magneto-Hydro-Dynamic Stability of a Large Prebaked Anode Aluminum Reduction Cell* (John Wiley & Sons, Inc, Hoboken, NJ, USA, 2013), pp. 603–607, ISBN 9781118605721;1118605721;.
- [71] M. Dupuis and V. Bojarevics, in *ALUMINIUM SMELTING INDUSTRY* (2021), pp. 54–57.
- [72] D. R. Sisan, *Hydromagnetic turbulent instability in liquid sodium experiments* (University of Maryland, College Park, 2004).

- [73] S. L. Brunton and J. N. Kutz, *Data-driven science and engineering: Machine learning, dynamical systems, and control* (Cambridge University Press, 2022).
- [74] R. Penrose, in *Mathematical proceedings of the Cambridge philosophical society* (Cambridge University Press, 1955), vol. 51, pp. 406–413.
- [75] R. Penrose, in *Mathematical Proceedings of the Cambridge Philosophical Society* (Cambridge University Press, 1956), vol. 52, pp. 17–19.
- [76] V. Bojarevics and S. Sira, *MHD stability for irregular and disturbed aluminium reduction cells* (Springer, 2014), pp. 685–690.
- [77] G. O. Linnerud, R. Huglen, and N. H. ASA, “Method for electrical connection and magnetic compensation of aluminium reduction cells, and a system for same,” (2011).
- [78] C. et al., “Device for connection between very high intensity electrolysis cells for the production of aluminium comprising a supply circuit and an independent circuit for correcting the magnetic field,” (1987).
- [79] M. Dupuis, J. Chaffy, and B. Langon (2015).
- [80] G. Lesieutre, in *Encyclopedia of Vibration*, edited by S. Braun (Elsevier, Oxford, 2001), pp. 321–327, ISBN 978-0-12-227085-7, URL <https://www.sciencedirect.com/science/article/pii/B0122270851000217>.
- [81] S. Akhmetov, J. Blasques, and M. I. Faraj, *Potline retrofit to increase productivity under energy supply constraints* (Light Metals Research Centre, 2018), ISBN 9780473464639.
- [82] N. Weber, P. Beckstein, W. Herreman, G. M. Horstmann, C. Nore, F. Stefani, and T. Weier, “Sloshing instability and electrolyte layer rupture in liquid metal batteries,” *Physics of fluids* (1994) **29**, 54101 (2017), ISSN 1070-6631.

- [83] G. M. Horstmann, N. Weber, and T. Weier, “Coupling and stability of interfacial waves in liquid metal batteries,” *Journal of Fluid Mechanics* **845**, 1 (2018), ISSN 0022-1120.
- [84] O. Zikanov, “Metal pad instabilities in liquid metal batteries,” *Physical review. E, Statistical, nonlinear, and soft matter physics* **92**, 063021 (2015), ISSN 1539-3755.
- [85] A. Allanore, L. Yin, and D. R. Sadoway, “A new anode material for oxygen evolution in molten oxide electrolysis,” *Nature (London)* **497**, 353 (2013), ISSN 0028-0836.
- [86] D. Sadoway, “Apparatus for electrolysis of molten oxides,” (2008).
- [87] B. Lillebuen, S. Ytterdahl, R. Huglen, and K. Paulsen, “Current efficiency and back reaction in aluminium electrolysis,” *Electrochimica acta* **25**, 131 (1980), ISSN 0013-4686.
- [88] J. Chen and M. Taylor, “The current efficiency model of lillebuen et al. for aluminium electrolysis,” *Electrochimica Acta* **35**, 109 (1990).
- [89] M. Sun, B. Li, and L. Li, “A multi-scale mathematical model of growth and coalescence of bubbles beneath the anode in an aluminum reduction cell,” *Metallurgical and Materials Transactions B* **49**, 2821 (2018).
- [90] A. Agnihotri, S. Pathak, and J. Mukhopadhyay, “Cell voltage noise in aluminium smelting,” *Transactions of the Indian Institute of Metals* **67**, 275 (2014).
- [91] L. Banta, C. Dai, and P. Biedler, *Noise classification in the aluminum reduction process* (2003), pp. 431–436.
- [92] B. Lillebuen, M. Bugge, and H. Hoie, “Alumina dissolution and current efficiency in hall-heroult cells,” *Light Metals* **2009**, 389 (2009).

- [93] L. Bugnion and J.-C. Fischer, *Effect of carbon dust on the electrical resistivity of cryolite bath* (Springer, 2016), pp. 587–591.
- [94] M. Dupuis and V. Bojarevics, in *TRAVAUX 51* (2022), pp. 1247–1258.